This is to certify that the
dissertation entitled

ATOMIC AND ELECTRONIC STRUCTURES OF NOVEL TERNARY AND QUATERNARY NARROW BAND-GAP SEMICONDUCTORS

presented by

KHANG HOANG

has been accepted towards fulfillment
of the requirements for the

Ph.D. degree in Physics and Astronomy

S. D. Mahanti

Major Professor's Signature

12/15/2007

Date

ATOMIC AND ELECTRONIC STRUCTURES OF NOVEL TERNARY AND QUATERNARY NARROW BAND-GAP SEMICONDUCTORS

By

Khang Hoang

A DISSERTATION

Submitted to
Michigan State University
in partial fulfillment of the requirements
for the Degree of

DOCTOR OF PHILOSOPHY

Department of Physics and Astronomy

2007

ABSTRACT

ATOMIC AND ELECTRONIC STRUCTURES OF NOVEL TERNARY AND QUATERNARY NARROW BAND-GAP SEMICONDUCTORS

By

Khang Hoang

This thesis concerns mainly with atomic and electronic structures of novel ternary and quaternary chalcogenide narrow band-gap semiconductors which are of great interest for infrared devices, photovoltaics, and high temperature thermoelectrics. More specifically, it presents studies of charge ordering and self-assembled nanostructures in a class of quaternary systems and their phase diagram, defect clustering and nanostructure formation in bulk thermoelectrics, atomic and electronic structures of ternary chalcogenides, and nature of defect states in narrow band-gap semiconductors.

Studies are carried out using Monte Carlo (MC) and *ab initio* methods to understand the nanostructuring phenomenon observed in $AgPb_mSbTe_{m+2}$ and similar systems. MC simulations in these quaternaries using an ionic model show a distinct phase diagram and a variety of structural orderings depending on the concentration of the monovalent and trivalent atoms as a result of the long-range nature of the Coulomb interaction. *Ab initio* density functional theory (DFT) based calculations also show that monovalent and trivalent impurities in PbTe, SnTe, and GeTe-based bulk thermoelectric materials like to come close to each other and form clusters or some sort of embedded nanostructures.

Interplay of atomic and electronic structures and band gap formation in I-V-VI_2 and Tl-based III-V-VII_2 ternary chalcogenides (I=Ag, Cu, Au, Na, K; V=As, Sb, Bi; VII=S, Se, Te) are studied using *ab initio* electronic structure calculations. These calculations have been able to identify low energy ordered structures which are consistent with experiments. Several intriguing physical properties of these materials can be understood in terms of the calculated electronic structure. This thesis suggests

how to modify a certain ternary by replacing its constituting element(s) such that the electronic structure shows desired features for different applications.

Comprehensive studies of the nature of defect-induced electronic states associated with a large class of substitutional impurities and native point defects in PbTe, SnTe, and GeTe are carried out using DFT and supercell models. Calculations are also carried out in PbTe thin films and nanoclusters to study how the defect states change in going from one geometry to another. This thesis also concerns with energetics of the defects, particularly defect formation energy, which may be able to give some information on the doping mechanism and the distribution of the defects in these systems. Based on the calculated electronic structures, one can explain the peculiar properties of PbTe doped with group III (Ga, In, Tl) impurities and the observed transport properties of PbTe, SnTe, and GeTe-based thermoelectrics.

To my family

Acknowledgements

I have benefited from numerous people during my graduate study at Michigan State University (MSU). First of all, I would like to thank my advisor, Professor S. D. Mahanti, for teaching me how to think "like a physicist". Over the last 5 years, he has provided me with an enormous amount of guidance and support and deeply inspired me with his love for science.

Next, I would like to thank the whole ONR-MURI team for providing me such a wonderful working environment where I had a chance to work side-by-side with and learn from different people from different disciplines. Of special note are Professor M. G. Kanatzidis and his past and current group members (MSU/Northwestern University) with whom I have worked most closely. Besides the ONR-MURI team, I would like to thank the following collaborators: K. Desai (MSU), S. Ahmad (MSU), Professor P. Jena (Virginia Commonwealth University), Professor J. Heremans Group (Ohio State University), Professor T. Tritt Group (Clemson University), Professor A. Freeman and Dr. L. Ye (Northwestern University), Dr. R. Loloee (MSU), and Professor S. Billinge Group (MSU).

I would also like to thank Professors B. A. Brown, M. Berz, P. Duxubury, S. Tessmer, and M. G. Kanatzidis for serving in my guidance committee. At last, I would like to thank my family and friends for their endless love and support.

Finally, I greatly acknowledge financial support from the U. S. Office of Naval Research through the ONR-MURI program "*Development and Application of High Efficiency Thermoelectric Materials for Power Generation*" (Grant No. N00014-03-10789), the U. S. Department of Energy for the work done at Virginia Commonwealth University (in Summer 2006), and MSU Graduate School for the Dissertation Completion Fellowship. I would also like to acknowledge the support of the MSU High Performance Computing Center.

Contents

List of Figures

List of Tables

Chapter 1

Introduction

In the last few years, my research has been to understand fundamental properties of complex materials using Monte Carlo (MC) and *ab initio* methods. These materials are mainly novel ternary and quaternary chalcogenide narrow band-gap semiconductors which are of great interest for infrared devices, photovoltaics, and high temperature thermoelectric applications. A fundamental understanding of these materials is crucial for explaining, predicting, and optimizing the properties of these materials, and to suggest new materials for better performance. In this chapter, I will briefly present some of these materials, challenges in understanding their properties which set the main motivations for my studies, and the theoretical approaches I have used to understand these properties.

1.1 Thermoelectricity and Thermoelectrics

As fossil fuel supplies decrease and world demands for energy increase, one of the biggest challenges that will face humankind in the twenty-first century is to provide a sustainable supply of energy to the world's population. Thermoelectric phenomena, which involve direct thermal-to-electric energy conversion and can be employed for both refrigeration and power generation, are expected to play an increasingly

important role in meeting these challenges [1, 2].

Thermoelectricity.—Thermoelectricity was discovered back in the nineteenth century by Seebeck [3] and underwent the first revival in 1950s started with Ioffe's observation [4] that doped semiconductor are the best thermoelectrics. Bismuth telluride (Bi_2Te_3), lead telluride (PbTe), and bismuth-antimony (Bi-Sb) alloys were the best materials for refrigeration during the 1957-1965 period [5, 6]. Over the three decades spanning 1960-1990, not much progress was made and the field of thermoelectrics received little attention from the worldwide research community. The second revival of interest in thermoelectrics came in early 1990s with strong support from funding agencies to encourage the research community to re-examine research opportunities to see if modern materials science can improve thermoelectric materials' performance for cooling and power generation [2, 6].

It has been established since 1950s that the performance of a thermoelectric device can be described by the dimensionless thermoelectric figure of merit, ZT, defined as [7]

$$ZT = \frac{\sigma S^2}{\kappa} T, \tag{1.1}$$

where σ is the electrical conductivity, S is the thermopower (Seebeck coefficient), T is the operating temperature, and $\kappa = \kappa_{el} + \kappa_{latt}$ is the total thermal conductivity containing an electronic part κ_{el} and a lattice part κ_{latt}; σS^2 is the materials property known as the thermoelectric "power factor". Within Boltzmann transport equation approach, the electrical conductivity σ and thermopower S for a cubic system can be calculated using the following equations [7]:

$$\sigma = e^2 \int_{-\infty}^{+\infty} d\epsilon (-\frac{\partial f_0}{\partial \epsilon}) \Sigma(\epsilon), \tag{1.2}$$

$$S = \frac{e}{T\sigma} \int_{-\infty}^{+\infty} d\epsilon (-\frac{\partial f_0}{\partial \epsilon}) \Sigma(\epsilon)(\epsilon - \mu), \tag{1.3}$$

where μ is the chemical potential, e the electron charge, f_0 is the Fermi-Dirac distribution function, and $\Sigma(\epsilon)$, known as the transport distribution function, is given by

$$\Sigma(\epsilon) = \sum_{\mathbf{k}} \nu_x(\mathbf{k})^2 \tau(\mathbf{k}) \delta(\epsilon - \epsilon(\mathbf{k})), \tag{1.4}$$

where the summation is over the first Brillouin zone (the band index has been dropped for simplicity), $\nu_x(\mathbf{k})$ is the group velocity of the carriers with wave vector $\mathbf{k}$ along the direction (x) of the applied field, $\tau(\mathbf{k})$ is the relaxation time, and $\epsilon(\mathbf{k})$ is the dispersion relation for the carriers. Mahan and Sofo [7] have shown that a delta-shaped transport distribution maximizes the thermoelectric properties (i.e., give highest ZT). For parabolic bands and when the relaxation time depends on $\mathbf{k}$ through $\epsilon(\mathbf{k})$, the transport distribution function takes the form [7]

$$\Sigma(\epsilon) = N(\epsilon) \nu_x(\epsilon)^2 \tau(\epsilon), \tag{1.5}$$

where $N(\epsilon)$ is the electronic density of states (DOS). Eq. (1.5) shows different approaches to manipulate the energy dependence of the transport function and consequently the temperature dependence of the transport functions.

Thermoelectric materials.—During the 1960-1990 period, the highest ZT values were $\sim$1, found in binary chalcogenides such as Bi_2Te_3, Sb_2Te_3 and their alloys [5, 6]. To make thermoelectric devices competitive with the existing technologies for cooling and power generation, one needs ZT values of 3-4 [8]. Increasing the value of ZT has been one of the most challenging tasks (increasing the electrical conductivity usually reduces S and increases κ_{el}, the net result being a reduction in ZT), although there are no fundamental thermodynamic arguments against achieving very high values of ZT [6]. A more realistic approach has been to reduce σ and κ_{el} and increase S by manipulating the DOS near the chemical potential through band structure engineering or strong correlation effects, and decreasing κ_{latt} through lattice engineering. Examples

of the former are In-doped PbTe [9] and doped cobaltates [10]. Those of the latter are multilayers of binary narrow band-gap semiconductors [11], skutterudites [12], quantum dot superlattices [13, 14] and bulk quaternary systems such as $AgPb_mSbTe_{2+m}$ (LAST-m; LAST stands for Lead-Antimony-Silver-Tellurium) containing Ag-Sb-rich nanoscale domains [15].[1]

Recent discoveries of new thermoelectric materials [16] that can give large ZT, particularly at high temperatures (T ~600-700 K), have created great deal of excitement. LAST-m, which is formed from a mixture of PbTe and $AgSbTe_2$, is among these materials; it gives ZT=1.7 at 700 K for m=18 [15]. Due to the small Ag and Sb concentration, one can consider LAST-18 as PbTe doped simultaneously with Ag and Sb. Compared to PbTe, LAST-18 shows an enhanced power factor and a reduced thermal conductivity. The increased ZT in LAST-m has been thought to be mainly due to the nanostructuring in the system where high-resolution transmission electron microscopy (HRTEM) images indicate inhomogeneities in the microstructure of these materials, showing nanoscale domains of a Ag-Sb-rich phase embedded in a PbTe matrix [15, 17]. Other materials discovered more recently also have high ZT values and are nanostructured, not solid solutions, such as $Ag(Pb_{1-y}Sn_y)_mSbTe_{2+m}$ [18], $Na_{1-z}Pb_mSb_yTe_{2+m}$ [19], and $K_{1-z}Pb_mSb_yTe_{2+m}$ [20].

1.2 Basic Issues and Theoretical Approaches

As mentioned above, LAST-m and similar PbTe-based systems have the following distinct features compared to PbTe: (i) nanostructuring, (ii) enhanced power factor (in some cases), and (iii) reduced thermal conductivity. A fundamental understanding of these features is crucial for explaining, predicting, and optimizing these materials, and also to suggest new materials for high performance thermoelectrics. This thesis

[1] For complete reviews of thermoelectric materials, see, Wood [5], Mahan [6], and the special issue of MRS Bulletin: *Thermoelectric Materials and Applications* (March 2006).

will focus on understanding the first two features.

It is well known that transport and optical properties of semiconductors are dominated by the electronic states in the neighborhood of the band gap. In a thermoelectric, for example, the figure of merit ZT depends on the electric conductivity σ and the thermopower S through Eq. (1.1). Clearly, large values of ZT require large values of S and σ, both of which depend sensitively on the nature of the electronic states near the band gap [see Eqs. (1.2) and (1.3)]. Thus it is essential to understand the underlying physics of the band gap formation and the nature of the electronic states in its neighborhood before being able to explain and optimize the properties of the systems. One, however, needs to know their atomic structures. Unfortunately, there is little, if any, information about the ordered structures of the above mentioned bulk thermoelectric materials and also of their end-compounds, i.e., $AgSbTe_2$, $NaSbTe_2$ and $KSbTe_2$.

In this thesis, I will study the properties of LAST-m and similar systems using the following approaches:

• Assuming that the bonding in LAST-m and similar systems has a strong ionic character as in PbTe, one can construct a simple ionic model to describe the interaction between atoms (ions) in these systems. This ionic model is then used in Monte Carlo (MC) simulations to study the ordering of the atoms on the host (e.g., PbTe) lattice. The output from these simulations will be used for further studies using more advanced (*ab initio* electronic structure calculations) methods.

• One can also learn a lot about LAST-m and similar systems by looking at and near their binary and ternary end-compounds. In LAST-m, the two end-compounds are PbTe and $AgSbTe_2$. Understanding the structural and electronic properties of $AgSbTe_2$ is crucial to understanding the properties of its quaternary or more complex counterparts. However, the atomic and electronic structures of this is unknown. One, therefore, tries to explore a large number of possible ordered structures and, via *ab*

initio electronic structure calculations, finds the one(s) with the lowest energy and studies the interplay of the atomic and electronic structures.

• From the other end-compound, LAST-m can be considered as PbTe doped with Ag and Sb, i.e., Ag and Sb are treated as defects in PbTe. This approximation is expected to be adequate at low impurity concentrations (large m values). One then looks at the electronic states induced by these two impurities and how they can affect the transport properties of the system.

Computational Methods.—This thesis makes intensive use of *ab initio* methods. Over the past 10-15 years, *ab initio* studies have had an increasingly important impact on materials science, not only in fundamental understanding of atomic and electronic structures but also with a strong emphasis toward materials design. Density functional theory (DFT) based calculations, in spite of their limitations, have been extremely helpful in this regard [21]. However, incorrect determinations of lattice parameters and band gaps are among the limitations and will be addressed in this thesis. A description of DFT is not given here because it has been given in many textbooks [22] and review articles [23, 24]. Besides DFT-based calculations, this thesis also makes use of Monte Carlo method, which will be presented in Chapter 2.

1.3 Overview

In Chapter 2, an ionic model for LAST-m (and similar systems) that explicitly includes the long-range Coulomb interaction between the ions residing on the sites of a face-centered cubic (fcc) lattice is presented. This model maps onto a spin-1 Ising model on a fcc lattice with long-range antiferromagnetic interaction. This is also a very interesting problem in statistical physics because of the long-range nature of the interaction and because fcc lattice is known to involve geometric "frustration". MC simulations have been carried out using this ionic model to construct the phase diagram and to study the ordering of the ions in the systems. Nanostructures obtained in

these simulations are further studied using *ab initio* methods. Some results from the simulations and ideas learned from the electronic structure of these nanostructures will be carried on to the next chapters.

Chapter 3 deals with atomic and electronic structures of I-V-VII_2 and Tl-based III-V-VII_2 ternary chalcogenides (I=Ag, Cu, Au, Na, K; V=As, Sb, Bi; VII=S, Se, Te). These classes of materials have been studied mainly in connection with optical phase change, photovoltaic, and thermoelectric applications. The ternaries constitute one end in the phase diagram (will be given in Chapter 2). $AgSbTe_2$, for example, is the end-compound (m=0) of LAST-m and similar systems such as $AgSn_mSnTe_{m+2}$ [25] and $AgGe_mSbTe_{m+2}$ [5]. In this chapter, extensive *ab initio* studies of the interplay of atomic and electronic structures and the nature of the electronic states near the band gap region are presented. These studies suggest how to modify a certain ternary by replacing its constituting element(s) such that the electronic structure shows desired features for better thermoelectric.

Chapter 4 approaches the phase diagram of LAST-m and similar systems from the other end. The nature of defect states in bulk, thin films, and nanoclusters of PbTe is studied using DFT and supercell models. I discuss how the defect states associated with different substitutional impurities and native point defects found in bulk PbTe are modified in the film and cluster geometries. The defects being considered are monovalent, divalent, and trivalent substitutional impurities (on the cation site), and vacancies on the cation and anion sites. I also look at the energetics of the defects and discuss their implications in the doping mechanism and distribution of the defects in PbTe systems.

Chapter 5 expands on the previous chapter with comprehensive studies of the impurity bands associated with various defects in PbTe, SnTe, and GeTe. The defects being considered are (but not limited to): Na, K, Ag, Sb, Bi (substitutional impurities on the cation site), and vacancies on the cation and anion sites. Defect clustering and

possible off-centering of the atoms in these systems are also considered. I will show how the peculiar properties of PbTe doped with group III (Ga, In, Tl) impurities and the observed transport properties of the whole class of PbTe, SnTe, and GeTe-based thermoelectric materials can be qualitatively understood in terms of the calculated electronic structures.

Finally, some remaining open issues and outlook for future research will be presented in Chapter 6.

Chapter 2

Phase Diagram and Self-Assembled Nanostructures in a Class of Quaternary Systems

The compositional ordering of Ag, Pb, Sb, and Te ions in $AgPb_mSbTe_{2+m}$ and of those in similar systems possessing a NaCl structure is studied using a Coulomb lattice gas (or ionic) model on a face-centered cubic (fcc) lattice and Monte Carlo simulations. The nanostructures obtained in the simulations are further studied using *ab initio* methods.

2.1 Introduction

Lattice gas[1] with long-range Coulomb interaction has attracted considerable interest over the past 20 years. Two types of long-range models have been studied. One where the interaction between the charges $\propto 1/r$ (Coulomb lattice gas, or CLG), and the other where the interaction $\propto \ln r$ (lattice Coulomb gas, or LCG). Studies of various models of one [26, 27, 28, 29]- and two [29, 30, 31]-dimensional CLG

[1]By "lattice gas" we mean a system of particles occupying the sites of a regular lattice with the restriction that no more than a single particle may be on any one site.

and LCG using different methods have shown the existence of multiple phase transitions, complexity in phase diagrams, and their practical applications to real materials, e.g., $KCu_{7-x}S_4$ [26, 27, 28] and $Ni_{1-x}Al_x(OH)_2(CO_3)_{x/2}.yH_2O$ [29]. In three-dimensional CLG on a simple cubic (sc) lattice, several works have been done using either approximate theoretical methods, such as mean-field approximation [32] and Padé expansion [33], or Monte Carlo (MC) simulations [32, 34]. However, to the best of my knowledge, there are no studies of CLG on a fcc lattice except when all the lattice sites are occupied by either a positive or a negative charge [35].

It is well known that fcc lattice involves competition (competing interactions) or also sometimes referred to as geometric "frustration",[2] a phenomenon in which the geometric properties of the lattice with specific type of interaction forbid the existence of a unique ground state. Geometric frustration, for example, occurs in the triangular, fcc, hexagonal close-packed, tetrahedron, pyrochlore and kagomé lattices with antiferromagnetic (AF) interaction between Ising spins [see examples in Fig. 2.1(a)-(c)]. Since the role played by frustration in the nature of phase transition in Ising-type systems (on triangular or fcc lattice) with short-range interaction has been of great interest in statistical physics [36, 37, 38, 39, 40], it is of equal interest to see what role frustration effects play in long-range Coulomb systems.

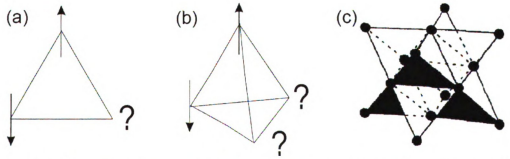

Figure 2.1: Geometric frustration in the fcc lattice with antiferromagnetic bonds: Ising spins on a (a) triangular and (b) tetrahedral plaquettes, and (c) geometrically frustrated fcc lattice.

[2]The term "frustration" was first introduced in 1977 by Toulouse to describe the inability to minimize fully all interactions; see, G. Toulouse, Commun. Phys. (London) 2, 115 (1977).

From a materials perspective, the quaternary compound $AgPb_mSbTe_{2+m}$ (LAST-m) [15] and similar systems, such as $Ag_{1-y}SnSb_{1+y}Te_3$ [25], $Ag(Pb_{1-y}Sn_y)_mSbTe_{2+m}$ [18], and $Na_{1-z}Pb_mSb_yTe_{2+m}$ [19], have recently emerged as materials for potential use in efficient thermoelectric power generation. These systems are not solid solutions but rather nanostructured materials. High-resolution transmission electron microscopy (HRTEM) images [see Fig. 2.2] from LAST-m samples, for instance, indicate inhomogeneities in the microstructure of the materials, showing nano-domains of a Ag-Sb-rich phase embedded in a PbTe matrix [15, 17]. Quantitative understanding of their properties requires understanding of the atomic structure. X-ray diffraction data in LAST-m [15, 17] suggest that this system belongs to an entire family of compounds, which are compositionally complex yet they possess the simple cubic NaCl structure on average, but the detailed ordering of Ag, Pb, and Sb ions is not clear. However, as pointed out by Bilc *et al.* [41], the electronic structure of these compounds depends sensitively on the nature of structural arrangements of Ag and Sb ions. Hence a simple but accurate theoretical model is necessary to understand and

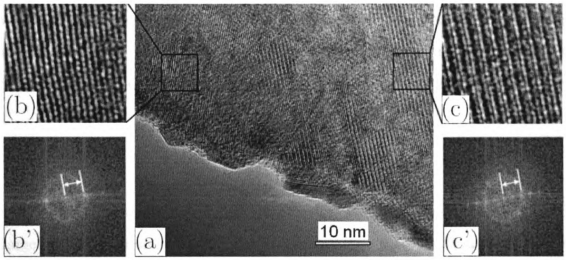

Figure 2.2: High-resolution transmission electron microscopy (HRTEM) image of a LAST-18 sample (a) shows the coexistence of two kinds of nanoscale domains which are magnified in figures (b) and (c). The fast Fourier transforms (FFT) of such zones [(b') and (c'), respectively] show that the lattice parameter of domain (c) is double that of domain (b). Image courtesy of M. G. Kanatzidis.

predict the ordering of the ions in these systems.

In this chapter, I present a simple ionic model for LAST-m and similar systems that explicitly includes the long-range Coulomb interaction and in which the ions are located at the sites of a fcc lattice. As will be shown in the next section, this problem maps onto a spin-1 Ising model on a fcc lattice with long-range AF interaction. The ionic model and computational details are presented in Sec. 2.2 and Sec. 2.3, respectively. In Sec. 2.4 and Sec. 2.5, I discuss the Monte Carlo simulation results including a complete phase diagram in the "x-T" (concentration of Ag and Sb ions versus temperature) plane and structural orderings at different locations in the phase diagram. Energetics and electronic structure of exotic nanostructures obtained in the simulations are further studied using *ab initio* density functional methods and the results are presented in Sec. 2.6. This chapter is concluded with a summary in Sec. 2.7. Part of this chapter has been published in *Physical Review B* [42].

2.2 Coulomb Lattice Gas (or Ionic) Model

We use a model where the minimization of electrostatic interaction energy between different ions in the compounds can lead to the compositional ordering that exists in the system [15]. The total electrostatic energy is then expressed as

$$E = \frac{e^2}{2} \sum_{l\tau \neq l'\tau'} \frac{Q_{l\tau} Q_{l'\tau'}}{\epsilon \mid \mathbf{R}_{l\tau} - \mathbf{R}_{l'\tau'} \mid}, \tag{2.1}$$

where ϵ is the static dielectric constant; $\mathbf{R}_{l\tau}$ and $Q_{l\tau}$ are, respectively, the position and charge of an atom at site τ of cell l. This model has been successfully applied to cubic perovskite alloys [34]. Here we consider supercells of the NaCl-type structure made of two interpenetrating fcc lattices with possible mixtures of different atomic species on Na sites, i.e., τ = {Na(Ag,Sb,Pb), Cl(Te)}, with periodic boundary condition. Ionic mixing occurs on the Na sublattice (see Fig. 2.3).

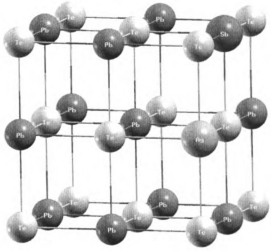

Figure 2.3: Example of ionic mixing on the Pb sublattice of the NaCl-type structure of PbTe. Small balls are for Pb and Te, large balls are for Ag and Sb.

In a simple ionic model of LAST-m, we can assume the Pb ion to be 2^+, Te ion to be 2^-, Ag ion to be 1^+, and Sb ion to be 3^+, i.e., $Q_{l\tau} = \{Q_{l,\mathrm{Na}}; Q_{l,\mathrm{Cl}}\} = \{+1, +3, +2; -2\}$, where $Q_{l,\mathrm{Cl}} = q_{\mathrm{Cl}} = -2$ is independent of l. Focusing on the Na sublattice sites where ordering occurs, we write $Q_{l\tau,\mathrm{Na}} = q_{\mathrm{Na}} + \Delta q_l$, where $q_{\mathrm{Na}} = +2$ and $\Delta q_l = \{-1, +1, 0\}$. Substituting the expression for $Q_{l,\mathrm{Na}}$ into Eq. (2.1), we can write $E = E_0 + E_1 + E_2$, where the subscripts refer to the number of powers of Δq_l appearing in that term. Then E_0 is just a constant, it is the energy of an ideal PbTe lattice, and E_1 vanishes due to charge neutrality. The only term which depends on the charge configuration is E_2; it is given by

$$E_2 = \frac{e^2}{2\epsilon a} \sum_{l \neq l'} \frac{\Delta q_l \Delta q_{l'}}{|\, l - l' \,|} \equiv \frac{J}{2} \sum_{l \neq l'} \frac{s_l s_{l'}}{|\, l - l' \,|}, \tag{2.2}$$

where ion positions are measured in unit of the fcc lattice constant a, l and l' run over the N sites of the Na-sublattice of NaCl structure, and s_l={−1,+1,0}.

Thus if we start from a PbTe lattice as a reference system and replace two Pb ions by one Ag ion and one Sb ion, we map the system unto a CLG with effective

charges -1, $+1$ (of equal amount) and 0; this implies a constraint, $\sum_l \Delta q_l = 0$. The model also maps onto a spin-1 Ising model ($s_l = 0, \pm 1$) with long-range AF interaction ($J > 0$). The short-range version of this model [nearest- (n.n.) and next-nearest-neighbor (n.n.n.) interaction] in the extreme limit (where $s_l = \pm 1$ for all l) on a fcc lattice has been investigated [38, 39, 40]. Grousson *et al.* [43], on the other hand, have studied a generalization of this model by adding a n.n. short-range ferromagnetic interaction on an sc lattice (also with $s_l = \pm 1$ for all l). A continuum version of this model that takes into account the finite size of the charged particles-restricted primitive model (RPM)[3] has been investigated by Bresme *et al.* [35] for a fcc lattice at the close packing limit and by Panagiotopoulos and Kumar [44] for a sc lattice; $s_l = \pm 1$ for all l in both the works. The spin-1 Ising model has also been studied by Dickman and Stell [32], but on a sc lattice and using mean-field approximation.[4] Comparison with the relevant works will be made in Sec. 2.4.

Because of the attraction between $+1$ and -1 charges, the Ag and Sb ions tend to come together and form clusters or some sort of ordered structures depending on the temperature at which these compounds are synthesized and the cooling profile (annealing scheme). The ordering may be quite complex compared to the one on a sc lattice because of the geometric frustration associated with spins on a fcc lattice and the AF interaction (in the Ising model). In the calculations for $AgPb_mSbTe_{2+m}$, an equivalent formula, $(AgSbTe_2)_x(Pb_2Te_2)_{(1-x)}$, is used; where $x = 2/(2+m) = 1/N\sum_l |\Delta q_l| \equiv 1/N\sum_l s_l^2$ $(0 \leq x \leq 1)$, is the concentration of Ag and Sb in the Pb sublattice. It is noted that one can apply this ionic model to a large class of $A_nB_mM_nQ_{m+2n}$ quaternary systems, where A={Na, K, Ag}, B={Ge, Sn, Pb}, M={As, Sb, Bi}, and Q={S, Se, Te}, due to their similarities.

[3]Restricted primitive model (RPM) is a system of charged hard-sphere anions and cations, all with equal charge magnitude $|q|$ and diameter σ.

[4]It is called "lattice restricted primitive model" (LRPM) in Dickman and Stell's work with the meaning that it is the lattice-gas version of the RPM.

2.3 Monte Carlo Simulation

To study the thermodynamic properties and microstructural ordering of the system, we have done canonical ensemble Monte Carlo (MC) simulations following the usual Metropolis criterion [45] using the energy given by Eq. (2.2), i.e., particles interact via site-exclusive (multiple occupancy forbidden) Coulomb interaction. The simulations were carried out at a fixed concentration (x). In the Ising model problem, this corresponds to a fixed magnetization simulation. Ewald summation [46] was used to handle this long-range interaction employing a very fast lookup table scheme using Hoshen-Kopelman algorithm [47]. This model is parameter-free in the sense that $J = e^2/\epsilon a$ defines a characteristic energy.

A simulation for a fixed concentration x started at a high temperature with an initial random configuration followed by gradual cooling. For each temperature T, 2×10^4 sweeps (MC steps per lattice site) were used to get thermal equilibration followed by 10^5 sweeps for averaging. Particles moved either via hopping to empty sites or via exchange mechanism. The equilibrium configuration at a given temperature T was used as the initial configuration for a study at a nearby temperature. Different thermodynamic quantities were monitored and the microstructures were analyzed. The data presented below were obtained with system size $L = 8$ (i.e., 8 fcc cells in one direction, 2048 lattice sites in total) with periodic boundary conditions.

2.4 Phase Diagram of LAST-m and Similar Systems

Fig. 2.4(a) shows the energy and heat capacity (obtained using energy fluctuation) for $x = 0.25$. The two energy curves correspond to slow cooling and slow heating. There is evidence of a first-order phase transition at $T = 0.08$ with an energy discontinuity,

which is further confirmed by a sharp peak in the heat capacity, and hysteresis. For $x = 0.75$, there are two phase transitions, one at $T = 0.106$ and the other at $T = 0.21$ [see Fig. 2.4(b)]. The heat capacity curve shows peaks at the above two T values. The transition at higher T is continuous and indicates a lattice gas-liquidlike phase transition. There is no apparent hysteresis associated with this transition. The low T transition, on the other hand, appears to be first-order. There is an energy discontinuity and there is hysteresis, albeit small, associated with this transition. For $x \leq 0.5$, only one transition is seen, which is first-order. This suggests that with decreasing x the system changes from undergoing two phase transitions to one. Also, I find that as x decreases from 0.875, the high T continuous and low T first-order phase transitions approach each other and the two transitions merge at $x \approx 0.5$. As x increases from 0.875, the high T continuous transition changes to first-order. At $x = 1$, the transition is first-order, in agreement with previous simulation of the RPM at the close packing density [35]. I also monitored the structure factor $S(\mathbf{q})$, defined as

$$S(\mathbf{q}) = \frac{1}{N}|\sum_{l} s_l e^{i\mathbf{q}.\mathbf{R}_l}|^2, \tag{2.3}$$

for different $\mathbf{q}$ values. For several $\mathbf{q}$ values, I find that $S(\mathbf{q})$ changes discontinuously at the first-order transition and smoothly at a continuous transition.

Phase diagram. —To construct the total phase diagram, I have studied energy, heat capacity and structure factor as functions of temperature for a series 15 values of the concentration x. Figure 2.5 shows the phase diagram constructed from the loci of specific heat maxima. The phase diagram consists of three different phases: disordered (D), partially ordered (PO), and ordered (O). The DO-O and PO-O transitions are first-order. In the limit $x = 0$, the compound is simply PbTe, and the transition should occur at $T = 0$ since there are no charged particles (effective charges of Pb and Te are 0). For $x = 1$, the compound is $AgSbTe_2$. The simulations show a strongly first-order transition at $T = 0.38$ and no other transition is found with

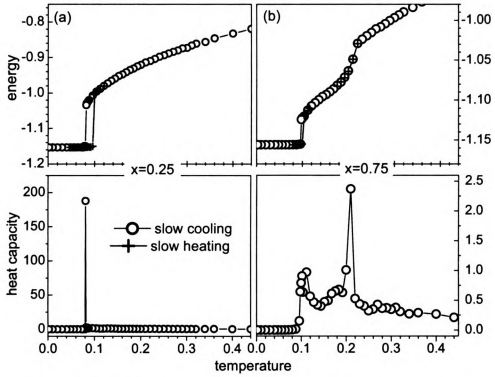

Figure 2.4: Energy and heat capacity (per particle) versus temperature for (a) $x = 0.25$ and (b) $x = 0.75$. Phase transitions occur at $T = 0.08$ (first order) for $x = 0.25$; at $T = 0.106$ (first order) and 0.21 (second order) for $x = 0.75$.

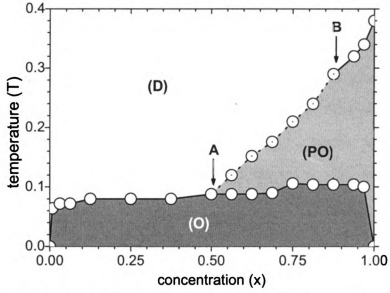

Figure 2.5: Concentration (x) versus temperature (T) phase diagram constructed from the loci of the heat capacity maxima. The phase diagram consists of three different phases: disordered (D), partially ordered (PO), and ordered (O). There are first (solid lines) and second (dotted line) order transitions with two possible tricritical points (x_t, T_t): A at $\approx (0.500, 0.088)$ and B at $\approx (0.875, 0.290)$.

decreasing T. This strong first-order transition is softened by introducing effectively neutral particles into the system (by decreasing x from 1). The hysteresis associated with this transition becomes smaller with decreasing x from 1 and disappears at $x \approx 0.875$ showing a changeover from a first- to a second-order transition. Therefore, we have two possible tricritical points [48] (x_t, T_t): A at $\approx (0.500, 0.088)$ and B at $\approx (0.875, 0.290)$. More accurate results on the tricritical points would require further careful large-scale simulations for more number of x values, and perhaps in much larger systems.

I would now like to compare our results with those of previous simulations carried out for lattice RPM. In this model, there is a parameter $\xi = \sigma/a$, where σ is the hard sphere diameter of the charged particles. For $\xi = 1$ which is comparable to our model, Panagiotopoulos and Kumar [44] have obtained a phase diagram for a sc lattice that is similar to ours. They found one tricritical point at (x_t, T_t)$\simeq$(0.48$\pm$0.02, 0.15$\pm$0.01) [44]. MC simulations of the CLG on a sc lattice by Dickman and Stell [32] give (x_t, T_t)$\simeq$(0.4, 0.14). It appears that x_t values for sc and fcc lattices are quite close whereas the T_t values for the fcc lattice is about a factor of 0.6 smaller, perhaps due to frustration. As regards the second tricritical point (B), it is unique to the fcc lattice. Dickman and Stell [32] found a high T continuous phase transition (λ-transition) in a sc lattice as x increased from 0.4 to 0.82. The observation of the high T first-order transition in our simulations ($x = 1$) is similar to the one seen in n.n. and n.n.n. Ising model on a fcc lattice by Phani *et al.* [39]. In this model, the Hamiltonian is

$$H = J \sum_{n.n.} \sigma_i \sigma_j - \alpha J \sum_{n.n.n.} \sigma_i \sigma_j, \tag{2.4}$$

where $\sigma_i = \pm 1$ and $J > 0$. Their MC simulations showed that the system underwent a first-order transition for $-1 \lesssim \alpha \lesssim 0.25$, whereas for other values of α the transition appeared to be continuous (second-order) [39].

Annealing versus quenching. —To see how the evolution of the system depends on

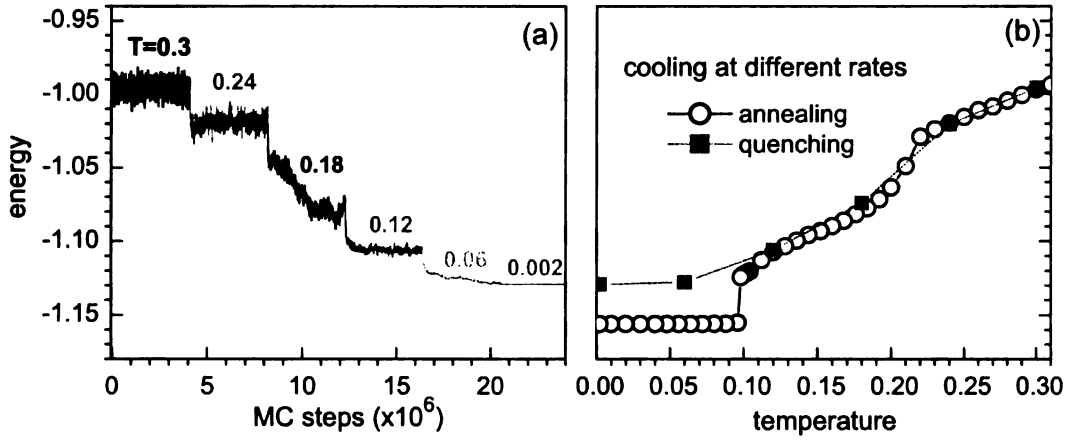

Figure 2.6: Energy (a) as a function of Monte Carlo steps and (b) as a function of temperature in annealing and in quenching studies. The system ($x = 0.75$) is quenched from $T = 0.3$ to 0.24, then from $T = 0.24$ to 0.18, and so on.

the cooling profile, i.e., slow cooling *vs* quenching, the system is quenched instead of being cooled gradually. Fig. 2.6(a) gives plot of the energy of a system with $x = 0.75$ as a function of MC steps as one quenches the system from $T = 0.3$ to 0.002 through several intermediate values of T. More than 4×10^6 moves are used for each T without discarding any step for thermal equilibration. The final configuration at a given T is used as the initial configuration for the next T. As we can see the energy fluctuation is large at high T and gets smaller with decreasing T. From one T to another, it takes some time ($\approx 10^3$ steps) for the system to equilibrate. As one crosses the transition region, e.g., from $T = 0.24$ to 0.18 or from 0.12 to 0.06, the result shows the existence of possible local minima in energy where the system is in a metastable state. The response of the system near the continuous transition to a sudden drop of temperature across the phase transition is quite different than going across the low-T first order transition. The system can not get to the ground state at T=0 which was obtained via annealing, as can be seen in Fig. 2.6(b). Structural differences between the quenched and annealed systems will be presented in the next section.

The comparison made with a system of smaller size ($L = 4$) shows no appreciable change in the results for the first-order transition except the fact that no hysteresis

was seen with $L = 4$. The energy at a given concentration differs by $0.1\% - 0.5\%$ from that obtained for $L = 8$. However, for the continuous transition along the line joining A and B in Fig. 2.5, one expects to see the usual finite size effects [49]. Most of the earlier simulations have been carried out in systems of similar sizes. For example, the system size $L = 4$ was also used by Bresme *et al.* [35] for a CLG in fcc lattice. Bellaiche and Vanderbilt [34] chose $L = 6$ for their study of cubic perovskite alloys. For a CLG in sc lattice, larger size lattices have been used because the number of atoms per unit cell is one in this case. For example, Panagiotopoulos and Kumar [44] and Dickman and Stell [32] chose $L = 12$ and 16, respectively.

2.5 Exotic Nanostructures Resulting from Competition

A typical low-temperature structure of $(AgSbTe_2)_x(Pb_2Te_2)_{(1-x)}$ for $0 < x < 0.375$ is a self-assembled nanostructure with layers of $AgSbTe_2$ arranged in a particular fashion in the PbTe bulk as shown in Fig. 2.7. In the case of $x = 0.25$, four layers of $AgSbTe_2$ are separated from one another by four layers of Pb_2Te_2. This domain is again separated by a purely PbTe domain formed by eight other layers of Pb_2Te_2. The superlattice pattern is similar for $x = 0.3125$. In each $AgSbTe_2$ layer (the xy plane), there are Ag (negative effective charge) chains separated by Sb (positive effective charge) chains align along the x and y directions. Along the z-direction (perpendicular to the layers), positive charge and negative charge arrange consecutively. This happens not only with the charges in the completely filled layers (e.g., in the upper picture of Fig. 2.7) but also with charge defects, like those in the sixth layer (from the bottom) in the lower picture of Fig. 2.7. This is clearly a result of the long-range Coulomb interaction. Experimentally, HRTEM images indicate inhomogeneities in the microstructure of the materials, showing nanoscale

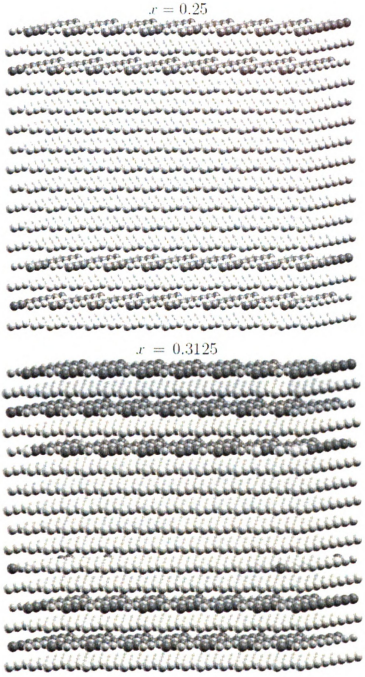

Figure 2.7: Layered (superlattice) structures formed out of Pb_2Te_2 layers separated by $AgSbTe_2$ layers for $x = 0.25$ (upper picture) and 0.3125 (lower picture). Small balls are for Ag, large balls are for Sb and Pb; Te sublattice is not shown.

domains of a Ag-Sb-rich phase embedded in a PbTe matrix [15, 17], which appears to be consistent with the simulation results (see also Fig. 2.2). Similar nanostructuring is also observed in $Ag_{1-y}SnSb_{1+y}Te_3$ [25], $Ag(Pb_{1-y}Sn_y)_mSbTe_{2+m}$ [18], and $Na_{1-x}Pb_mSb_yTe_{2+m}$ [19]; see Fig. 2.8.

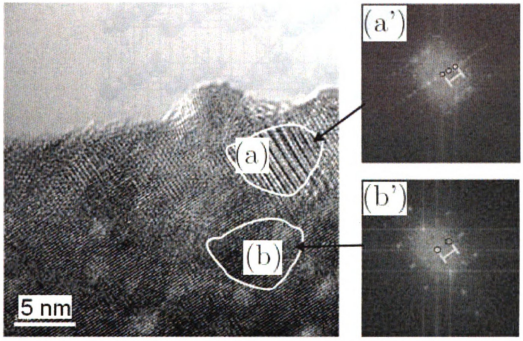

Figure 2.8: High-resolution transmission electron microscopy (HRTEM) image of a $Na_{0.95}Pb_{20}SbTe_{22}$ sample shows the coexistence of domains (a) and (b) with different features. The fast Fourier transforms (FFT) of such domains [(a') and (b'), respectively] show that the lattice parameter of domain (a) is double that of domain (b). Image courtesy of M. G. Kanatzidis.

In going to larger x values, even more exotic structures are discovered at several x values. For $x = 3/8$ ($m = 10/3$), Ag and Sb form a sodalite framework [50] that encapsulates PbTe cubes (see Fig. 2.9). The unit cell of this framework is usually referred to as the β-cage; it resembles a truncated octahedron [51]. For $x = 0.5$ ($m = 2$), an array of tubes of $AgSbTe_2$ and Pb_2Te_2 are arranged in a checker-board pattern (Fig. 2.10). This structure, here called $AgPb_2SbTe_4$ or LAST-2 "tubular structure", has the same energy as the layered (superlattice) structure consisting of alternate layers of $AgSbTe_2$ and Pb_2Te_2 (energy per particle $E = -1.157278$), I will

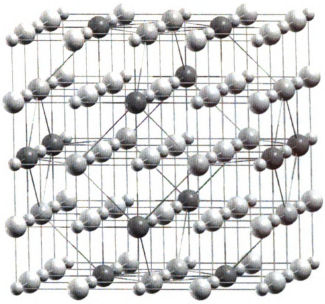

Figure 2.9: Unit cell of the sodalite-like structure observed at $x = 3/8$. Connected, dark grey balls are for Ag/Sb, light grey balls are for Pb (large balls) and Te (small balls). Ag and Sb form a sodalite-like network.

call it $AgPb_2SbTe_4$ or LAST-2 "layered structure". This tubular structure is also found at $x = 0.4375$ (see Fig. 2.10). However, the checker-board pattern in this case is less perfect because of the smaller number of the charged particles present at this concentration. It coexists with PbTe-type domains.

In the limit $x = 1$, the compound is $AgSbTe_2$ and the ordered structure is body-centered tetragonal (bct) structure with a c-parameter which is double that of the NaCl subcell, belongings to the space group $I4_1/amd$ (including the Te sublattice). The unit cell of this structure has eight atoms, with every Ag or Sb atom surrounded by eight atoms of opposite charge and four of the same charge (Te is effectively neutral). The ordering of Ag and Sb in this structure of $AgSbTe_2$ is equivalent to the type-III AF structure (hence named AF-III) which has been found in n.n. and n.n.n. Ising model by Phani *et al.* [39]. The mapping to the AF Ising model is straightforward with Ag$\equiv\uparrow$ and Sb$\equiv\downarrow$. The AF-III structure has also been found in the RPM by Bresme *et al.* [35] in Monte Carlo simulations and by Ciach and Stell [52] within a field-theoretic approach. In a n.n. and n.n.n. Ising model [see Eq. (2.4)] on a

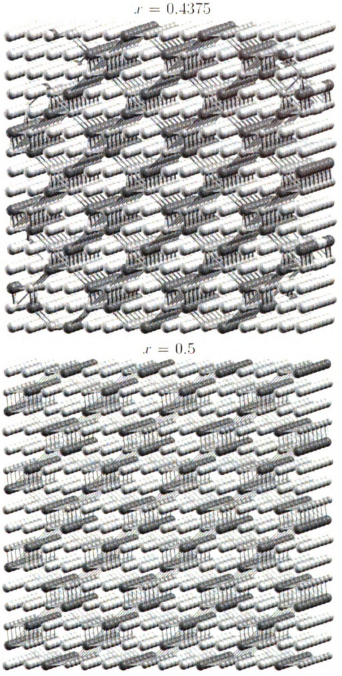

Figure 2.10: Checker-board pattern tubular structure formed by $AgSbTe_2$ and Pb_2Te_2 blocks for $x = 0.4375$ (upper picture) and 0.5 (lower picture). Connected balls are for Ag/Sb, unconnected balls are for Pb; Te sublattice is not shown.

fcc lattice, Phani *et al.* [39] found that AF-III was the ground state for $-0.5 < \alpha < 0$, where $-\alpha$ is the n.n.n. coupling constant. Since $-\alpha > 0$, n.n.n. interaction is also antiferromagnetic. As I will discuss in the next chapter, AF-III acts as a starting point for us to explore different ordered structures of $AgSbTe_2$ and similar systems using *ab initio* electronic structure calculations.

Low temperature structures for $0.5 < x < 0.75$ (Fig. 2.11) are those with domains of $AgSbTe_2$ possessing a bct structure (described above), $AgPb_2SbTe_4$-layered structure, and PbTe. For $x = 0.75$, the ordered (O) phase ($T < 0.1$) does not have a PbTe domain, only a mixture of AF-III and $AgPb_2SbTe_4$-layered structures (Fig. 2.12). The partially ordered (PO) phase ($0.1 < T < 0.21$), on the other hand, has Pb atoms (charge neutral particles) distributed somewhat randomly in the whole space. The Ag/Sb network is, however, quite well-defined with Ag and Sb chains aligning almost perfectly, although the chains themself are not perfect because of the Pb defects. The low temperature configuration obtained in quenching studies of $x = 0.75$ (Fig. 2.6) is similar to the one in the PO phase (Fig. 2.13). This is because the transition from the disordered (D) phase to PO phase is second-order and, therefore, the D phase (with $x > 0.5$) is can not be quenched into a metastable state.

"Good bonds" versus "bad bonds". —In an Ising-like model with AF interaction like our CLG model, a positive charge (up spin) tends to come close to a negative charge (down spin) since it is energetically favorable. Let us define this as a "good bond" (GB). A charged particle wants to have as many GBs as possible with other particles within the interaction range. The interaction between two particles with the same charge is energetically unfavorable. Let us define this as a "bad bond" (BB). The interaction between a positive or a negative charge with a neutral charge is zero; we will call it "neutral bond" (NB). On a fcc lattice, which is known to have geometric "frustration", one can not have all nearest neighbor bonds as GBs. I have examined the structures obtained in the MC simulations and find that each charged particle

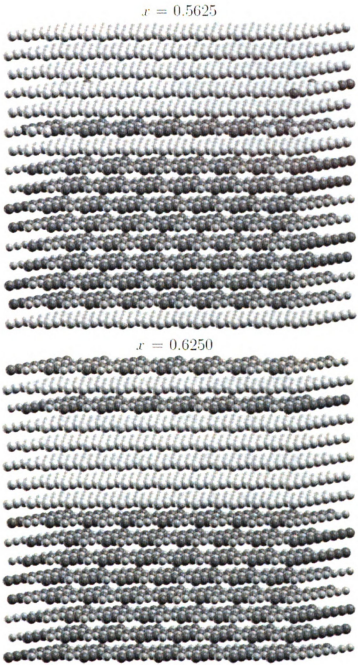

Figure 2.11: Domain-separated structures for $x = 0.5625$ (upper picture) and 0.6250 (lower picture). Small balls are for Ag, large balls are for Sb and Pb; Te sublattice is not shown.

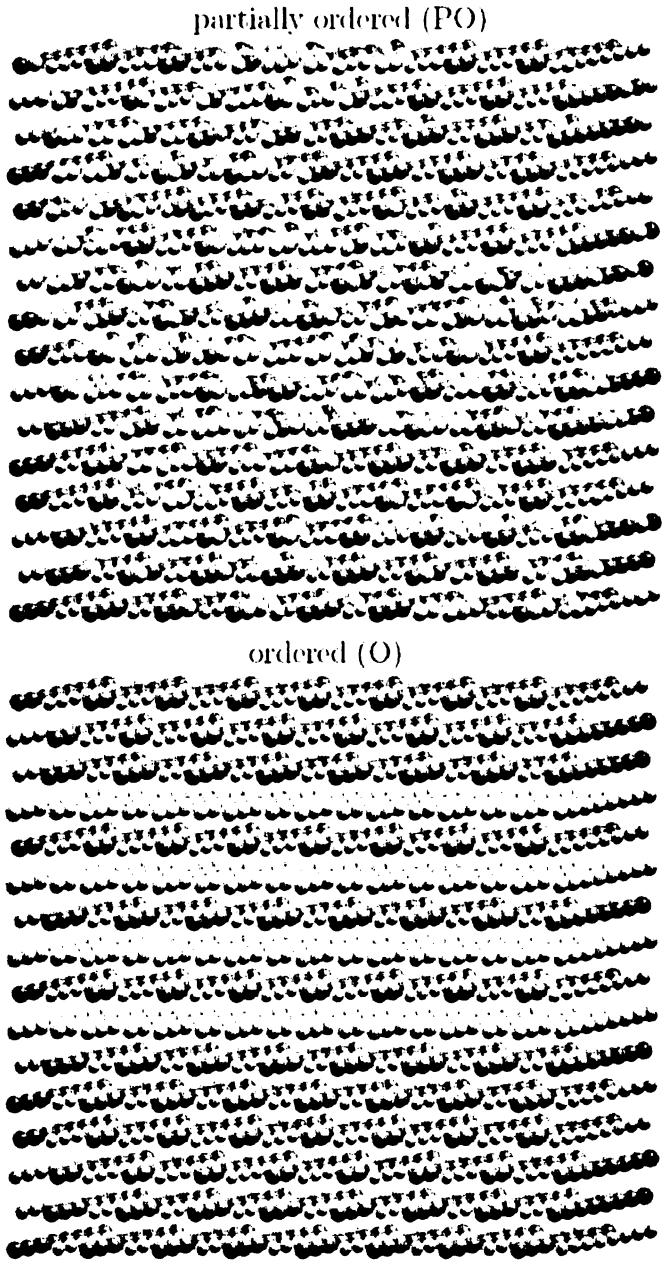

Figure 2.12: Configurations observed in the partially ordered (PO) phase (at $T = 0.16$; upper picture) and in the ordered phase (lower picture) of $x = 0.75$. Small balls are for Ag, large balls are for Sb and Pb; Te sublattice is not shown.

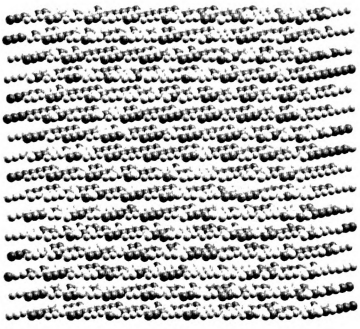

Figure 2.13: Low temperature structure obtained in quenching studies of $x = 0.75$. Small balls are for Ag, large balls are for Sb and Pb; Te sublattice is not shown.

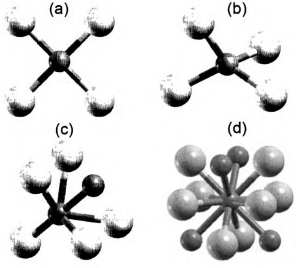

Figure 2.14: "Good bonds" (energetically favorable) versus "bad bonds" (energetically unfavorable) and orderings in an ionic model: (a) layered, (b) sodalite-like, (c) tubular, and (d) AF-III structures. Small (large) balls are for positive (negative) effective charges. Neutral bonds are not shown.

has 4 GBs and 8 NBs in the layered structures [Fig. 2.14(a)]; 5 GBs, 1 BB, and 6 NBs in the tubular structure [Fig. 2.14(b)]; 4 GBs and 8 NBs in the sodalite-like structure [Fig. 2.14(c)], and 8 GBs and 4 BBs in the AF-III structure [Fig. 2.14(b)]. After taking into account the cancelation between GBs and BBs which are in opposite direction and equal in magnitude, all these structures have 4 GBs. They, therefore, should be degenerate in the n.n. interaction model; the degeneracy is, however, lifted by long-range interaction.

2.6 *Ab initio* Study of the Exotic Nanostructures

In order to go beyond the CLG model of these mixed ion systems, *ab initio* studies are needed to see not only the effects of covalency on the atomic structure but also to look at the interdependence of electronic and atomic structures. The nanostructures obtained in the MC simulations are used as the initial structures in these studies. In this section, we focus mainly on LAST-m with m=2 (x = 0.5, i.e., $AgPb_2SbTe_4$) which has the tubular structure and m=10/3 (x=3/8, i.e., $Ag_3Pb_{10}Sb_3Te_{16}$) which has the sodalite-like structure. The layered structure of LAST-2 consisting of alternate layers of $AgSbTe_2$ and Pb_2Te_2 is also investigated and comparisons with its tubular counterpart will be made. $AgSbTe_2$ (m = 0) will be studied in the next chapter. Different superlattice structures of other m values for the Ag/Sb/Pb/Te and Ag/Sb/Sn/Te systems have also been studied but presented elsewhere [53, 54].

Computational Details. –Structural (ionic) optimization[5], total energy and electronic structure calculations were performed within the density functional theory (DFT) formalism, using the generalized-gradient approximation [55] and the projector-augmented wave (PAW) [56] method as implemented in the *Vienna Ab initio Simulation Package* (VASP) [57], and a supercell model. Each calculation begins with

[5]Structural (ionic) optimization, or structural (ionic) relaxation, includes volume optimization and internal (ion positions) relaxation.

structural optimization of the supercell, the relaxed cell is then used to calculate energy and electronic density of states (DOS). Scalar relativistic effects (mass-velocity and Darwin terms) and spin-orbit interaction (SOI) were included, unless otherwise noted. In the structural optimization, only the scalar relativistic effects were taken into account since it is found that the inclusion of SOI did not have significant influence on the structural properties [58].

Structural relaxation and energetics. —Cubic supercells with 64 atoms/cell are used for the layered and tubular (LAST-2) and the sodalite-like structure. The optimized lattice constant of the LAST-2 systems is 12.7 Å, whereas it is 12.82 Å for the sodalite-like one. The supercell of the layered LAST-2 is built up by 8 bct primitive cells (a=6.25 Å and c/a=2.0); that of the tubular LAST-2 is built up by 2 simple tetragonal (st) primitive cells (a=12.7 Å and c/a=0.5). In the layered LAST-2, the atoms relax mostly along the z direction (normal to the $AgSbTe_2$ and Pb_2Te_2 layers), where the Te atoms move towards Sb resulting in ~1.87% contraction (expansion) in the Sb-Te (Ag-Te) bond lengths. If no constraints are imposed on the supercell (e.g., allow the supercell shape to relax) then there will be an overall expansion of the structure along the z direction. After internal relaxations, the total energy of the layered LAST-2 is lowered by ~5 meV/f.u. (f.u.=$AgPb_2SbTe_4$). The internal relaxations are much larger in the tubular structure because of the complex geometry; the changes in the bond lengths range from +0.09% to −3.77% for the Ag-Te bonds and from +0.04% to −4.20% for the Sb-Te bonds. This helps lower the total energy of the tubular LAST-2 by ~250 meV/f.u. It is also found that the tubular structure is lower in energy than the layered one by ~168 meV/f.u. This means that if one goes beyond the CLG model the degeneracy between the two structures of LAST-2 is removed. There are also significant internal relaxations in the sodalite-like system with a relaxation energy of ~531 meV/f.u. (f.u.=$Ag_3Pb_{10}Sb_3Te_{16}$).

Electronic structure of the layered and tubular LAST-2. —Figs. 2.15(a)-(d) show the total density of states (DOS) and the partial density of states (PDOS) of LAST-2 in the layered and tubular structures. LAST-2 in both structures appears to be a semimetal with a very well-formed pseudogap in the DOS near the Fermi energy (ϵ_F=0 eV). The number of electronic states at ϵ_F is very small and is nearly zero for the layered structure in the presence of SOI. The DOS changes rapidly in the neighborhood of ϵ_F and there are many sharp peak structures showing possible quasi-one-dimensional (quasi-1D) energy bands. An analysis of the PDOS of the layered and the tubular LAST-2 [see Fig. 2.15(b) and 2.15(d)] shows that the sharp peaks just

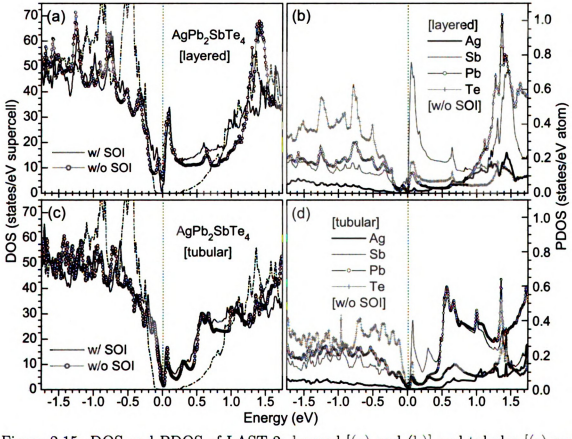

Figure 2.15: DOS and PDOS of LAST-2: layered [(a) and (b)] and tubular [(c) and (d)] structures. DOS of PbTe (the dash-dotted curve) is also provided for comparison. The Fermi level (ϵ_F) is set to the highest occupied state.

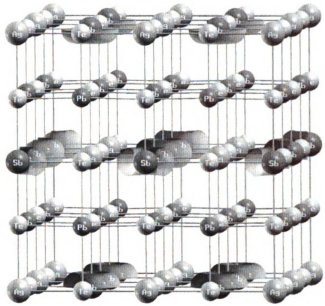

Figure 2.16: Charge density associated with the states in the energy range from 0 eV to +0.2 eV of the layered LAST-2. The states that contribute to this region are predominantly Sb p.

above ϵ_F are predominantly Sb p,[6] whereas the region below ϵ_F is predominantly Te p hybridizing with Pb and Sb p.

The partial charge density associated with the sharp peak just above ϵ_F [in the energy range: 0 eV to +0.2 eV; see Fig. 2.15(a)] is visualized in Fig. 2.16. As can be seen from the figure, the electronic states associated with this peak are predominantly Sb p states associated with the Sb-Te chains in the $AgSbTe_2$ planes. This picture confirms the quasi-1D feature in the electronic structure we have discussed above. These features should have important implications in transport properties in these systems and are very desirable for good thermoelectric materials [7, 59].

Interrupted chain model. —From the above analysis we know that Sb in the Sb-Te chains play a crucial role in controlling the electronic states in the band gap region and in forming the quasi-1D band structure. It is, therefore, desirable to see how the electronic structure of the system changes if one modifies the ordering of the

[6]The comparison is made based on the number of states contributed to the total DOS from a single atom of a constituent element, not the total contribution from a constituent element.

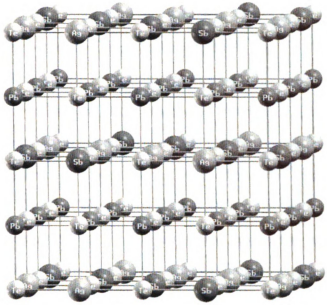

Figure 2.17: Interrupted chain (ic) model for the layered structure of LAST-2: the Sb-Te chains in the $AgSbTe_2$ planes are interrupted by Ag atoms.

cations in the $AgSbTe_2$ planes (in the layered structure) or the $AgSbTe_2$ tubes (in the tubular structure). To examine the former, an interrupted chain (ic) model has been constructed for the layered LAST-2 (hence named icLAST-2) where all Sb-Te chains are interrupted by Ag atoms [see Fig. 2.17]. As seen in the figure, icLAST-2 has Ag-Te-Sb-Te-... chains along the x and y directions (in the $AgSbTe_2$ planes).

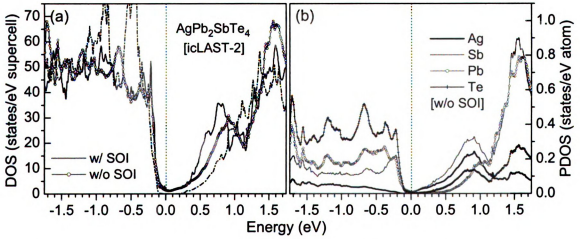

Figure 2.18: (a) DOS and (b) PDOS of icLAST-2. DOS of PbTe (the dash-dotted curve) is also provided for comparison. The Fermi level (ϵ_F) is set to the highest occupied state.

Fig. 2.18(a) shows the total DOS of icLAST-2. There is a large suppression of the DOS in the neighborhood of ϵ_F. The sharp peak just above ϵ_F observed in the layered LAST-2 (with the Sb-Te chains) disappears with transfer of the electronic states to higher energy. There is also a transfer of electronic states below ϵ_F to lower energy which results in lowering the total energy of the system. The LAST-2 with the interrupted chains is lower in energy than the uninterrupted one by ~136 meV/f.u.; f.u.=$AgPb_2SbTe_4$. The PDOS analysis [Fig. 2.18(b)] also shows that the states in the region near ϵ_F coming from Sb and Te atoms have been suppressed drastically compared to the uninterrupted one. This suggests how to engineer atomic structure in a system in order to tailor it properties. This idea will be explored further in Chapter 3 where I present my studies on atomic and electronic structures of several classes of ternary chalcogenides.

Electronic structure of the sodalite-like LAST-10/3. —The sodalite-like structure also shows a pseudogap feature [Fig. 2.19(a)]. The number of states at ϵ_F is almost zero. There is a broad peak (or a double peak) just above ϵ_F ranging from 0 eV to +0.4 eV and another one in the region ranging from +0.4 eV to +0.9 eV. An analysis of the PDOS of LAST-10/3 shows that Sb and Te atoms contribute almost equally

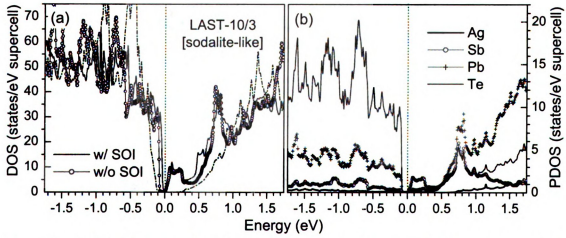

Figure 2.19: (a) DOS and (b) PDOS of the sodalite-like LAST-10/3. DOS of PbTe (the dash-dotted curve) is also provided for comparison. The Fermi level (ϵ_F) is set to the highest occupied state.

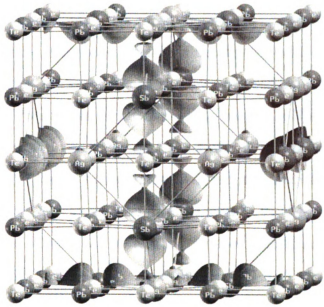

Figure 2.20: Charge density associated with the states in the energy range from 0 eV to +0.4 eV of the sodalite-like LAST-10/3. The states contribute to this region are predominantly Sb p hybridizing with Te p along the Sb-Te chains.

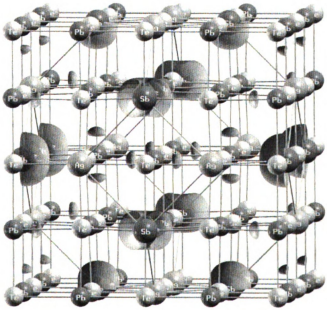

Figure 2.21: Charge density associated with the states in the energy range from +0.4 eV to +0.9 eV of the sodalite-like LAST-10/3. The states contribute to this region are predominantly Sb p with some contribution from Pb p components which align along the Pb-Te-Sb chains.

to the first peak. However, since there are only 6 Sb atoms but 32 Te atoms in the supercell, each Sb atom contributes much more than a single Te atom. Hence we can say the first peak is predominantly Sb p hybridizing with Te p along the Sb-Te chains; see Fig. 2.20. The second peak is, however, predominantly Sb p with some contributions from Pb p states which align along the Pb-Te-Sb chains [Fig. 2.21].

Spin-orbit effects.—In order to see the effects of spin-orbit interaction (SOI), the DOS obtained in calculations where SOI was not included are also given in Figs. 2.15(a), 2.15(c), 2.18(a), and 2.19(a). As seen in the figures, SOI pushes some states from the valence band top up and some states from the conduction band bottom down in energy. These effects are small in LAST-10/3 compared to PbTe (see discussions in Chapter 4), they are much smaller in the LAST-2 compound due to the lower Pb and Te concentration. There is one discernible effect in layered LAST-2, where the DOS at the Fermi energy reduces drastically in the presence of SOI. It is noted that most DFT calculations underestimate the band gaps of semiconductors and the systems may actually have small gaps. For example, our DFT-GGA calculations give PbTe a band gap of ~0.1 eV, whereas experiment gives 0.19 eV (at 4 K) [60]; the calculations give $AgSbTe_2$ a negative gap [61], whereas experiments give a small gap [61] (see discussions in Chapter 3).

2.7 Summary

In summary, the phase diagram of the CLG on a fcc lattice shows the distinct feature of having two tricritical points; in contrast to a simple cubic lattice where it has only one tricritical point. I have demonstrated that MC simulation using an ionic model of $(AgSbTe_2)_x(Pb_2Te_2)_{(1-x)}$ and related systems shows different possible structural orderings. Layered structures formed out of $AgSbTe_2$ layers separated by Pb_2Te_2 layers are typical low-temperature structures. In addition to the layered structures, tubular structures for x=0.4375 and 0.5, sodalite-like structure for $x = 3/8$ have also

been discovered. For $x = 1$, a bct structure has been found to be the lowest energy, in agreement with previous simulation results in the RPM [35] and a n.n. and n.n.n. Ising model [39]. Structures for other values of x are mixtures of those for $x = 0$, 0.5 (layered or tubular structure), and 1.

Ab initio studies of the exotic nanostructures obtained in MC simulations show that the tubular structure, among the three different structures (layered, interrupted, and tubular) of LAST-2, has the lowest total energy. Both the tubular LAST-2 and the sodalite-like LAST-10/3 have large relaxation energy. All these exotic nanostructures are semimetals with very small DOS at the Fermi energy. I find that the Sb p states associated with the Sb-Te chains dominate the states in the band gap region that tend to drive the systems towards (semi)metallicity. The interruption of the Sb-Te chains by Ag atoms significantly reduces the DOS in the band gap region. This suggests how to engineer the atomic structure in order to have a desired electronic structure of narrow band-gap semiconductors. I will explore this idea further in the next chapter where I present my studies on atomic and electronic structures of several classes of ternary chalcogenides.

Although Ag and Sb have high concentrations and are highly ordered in LAST-10/3 and LAST-2, the electronic structures of these two compounds resemble that of PbTe, except that the PbTe band gap region are filled up with electronic states which are predominantly Sb p. One, therefore, can consider these systems as PbTe with (Ag,Sb) "defect complexes" which introduce states into the band gap region. This provides us with an important hint: One can learn a great deal about, for example, PbTe, SnTe, and GeTe-based systems by carefully studying defects, defect pairs, and defect complexes in the corresponding host materials. This idea will be demonstrated in Chapter 4 and 5 where I present my comprehensive studies of defect states in PbTe, SnTe, and GeTe.

Chapter 3

Atomic and Electronic Structures of Ternary Chalcogenides

Novel semiconductors with tailored properties can be designed theoretically based on our understanding of the interplay of atomic and electronic structures and the nature of the electronic states near the band gap region. I discuss here the realization of this idea in the group-I-V-VII_2 ternary chalcogenides, which are important optical phase change and thermoelectric materials. They are also the end compounds of the LAST-m and similar systems which have been introduced in earlier chapters.

3.1 Introduction

I-V-VII_2 ternary chalcogenides, especially Ag-Sb-based systems, have been studied mainly in connection with optical phase change [62] and thermoelectric applications [5]. $AgSbTe_2$, for example, is not only a good thermoelectric but is the end-compound of several high-temperature high-performance thermoelectrics [5, 15, 18, 25]. It has very low lattice thermal conductivity (0.6 W/m K) [5]. Although it was synthesized almost 50 years ago and was thought to be a semiconductor [63, 64], the ordering of Ag and Sb on a face-centered cubic (fcc) lattice has been confirmed

only recently [17]. Furthermore, the electronic properties of these systems are quite intriguing and show anomalies. Diffuse reflectance measurements [61] in $AgSbTe_2$ give an apparent band gap (~0.35 eV), whereas electrical conductivity [65] suggested a metallic behavior. A similar observation in the diffuse reflectance spectrum of $AgSbSe_2$ has also been made (apparent band gap of ~0.57 eV) [61]. Other I-V-VII_2 compounds have also been synthesized and investigated [63, 64, 66, 67]. However, unlike I-III-VI_2 (where I=Ag, Cu; III=Al, Ga, In, Tl; VI=S, Se, Te) and II-IV-V_2 (II=Be, Mg, Ca, Zn, Cd; IV=Si, Ge, Sn; V=N, P, As, S) chalcopyrites where extensive theoretical works have been done [68, 69, 70], to the best of my knowledge, there are very few, if any, theoretical studies on atomic and electronic structures of the I-V-VI_2 compounds, except for some preliminary results on $AgSbTe_2$ by Bilc [71] and by Kumar *et al.* [72].

Besides the I-V-VI_2 ternary chalcogenides, there have been also of great interests in Tl-based III-V-VI_2 compounds, especially for thermoelectrics. $TlBiTe_2$ has been proposed as a candidate material for thermoelectric applications for several decades [73, 74] but its use has been limited due to the fact that Tl and its compounds have to be handled carefully. Superconductivity has been also found to occur at 0.14 K in samples of $TlBiTe_2$ with nominal carrier densities ($\sim 6\times10^{20}$ holes/cm^3) [75]. There has been a revival of interest in these Tl-based ternary chalcogenides for thermoelectric applications inspired by interesting results from recent studies. Wölfing *et al.* [76] have reported a ZT ~1.2 at 500 K for Tl_9BiTe_6. This compound exhibits an extremely low thermal conductivity (0.39 W/m K at 300 K) [76]. Tl_9BiTe_6 together with $TlBiTe_2$ are usually found in Tl_2Te-Bi_2Te_3 systems. It is reported that $TlBiTe_2$ also has a relatively low thermal conductivity compared to other state-of-the-art thermoelectric materials [77]. The Sb counterpart of this compound, $TlSbTe_2$, is also known to be a good thermoelectric (ZT ~0.87 at 715 K) [78].

To understand the origin of the intriguing physical properties of the I-V-VI_2 and

Tl-based III-V-VI_2 chalcogenides, extensive *ab initio* electronic structure calculations have been carried out within the density functional theory (DFT) formalism. In Sec. 3.2, the energetics of different types of ordering of the cations and how they impact on the electronic properties are investigated starting with the Ag-Sb-based I-V-VI_2 compounds. Available experimental data are used to critically examine the calculated electronic structure. To see how the general characteristics of these compounds change as one changes the monovalent atom and/or the trivalent atom, I study a class of ternaries where the monovalent Ag is replaced by other monovalent atoms (such as Cu, Au, Na, and K) and the trivalent Sb is replaced by other trivalent atoms (such as As and Bi). These results are discussed in Sec. 3.3. Finally, in Sec. 3.4, I discuss my work on Tl-based ternaries. A major part of the study on AgSbQ_2 has been published in *Physical Review Letters* [61].

3.2 Ag-Sb-Based Ternary Chalcogenides

3.2.1 Atomic Ordering and the Crystal Structure

For electronic structure calculations we need to know the ordering of Ag and Sb atoms. Although earlier X-ray diffraction (XRD) measurements of AgSbQ_2 indicated that Ag and Sb were disordered on the Na site of the NaCl-type structure [64], recent careful single-crystal XRD studies of $AgSbTe_2$ have found evidence of Ag-Sb order; $Pm\bar{3}m$ (cubic), $P4/mmm$ (tetragonal) and $R\bar{3}m$ (rhombohedral) space groups were used successfully in diffraction refinement [17]. Also, as discussed in Chapter 2, Monte Carlo (MC) simulation of an ionic or Coulomb lattice gas (CLG) model gave a body-centered tetragonal (bct; space group $I4_1/amd$) structure with a c-parameter double that of the NaCl-type cubic lattice [42]. I have calculated the total energies of these and various other ordered structures to find the one(s) with the lowest energy.

Before presenting the energy calculations, I describe the different types of ordering

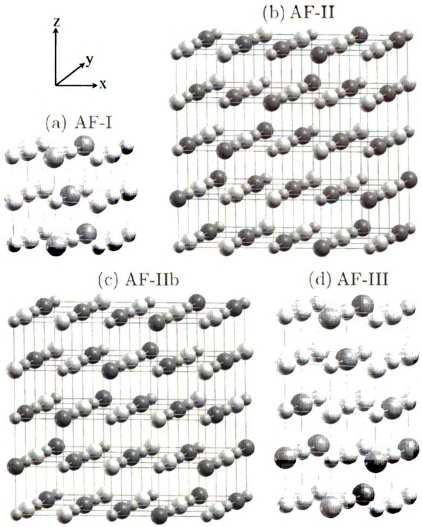

Figure 3.1: Possible ordered structures of $AgSbQ_2$ (Q=Te, Se, S): (a) AF-I (space groups: $Pm\bar{3}m$, $P4/mmm$), (b) AF-II ($R\bar{3}m$), (c)AF-IIb ($F\bar{3}dm$), and (d) AF-III ($I4_1/amd$). Large balls are for Ag/Sb, small balls are for Q.

of Ag and Sb ions using the standard nomenclature of anti-ferromagnetic (AF) orderings [39], i.e., identify Ag(Sb) ions as spin-up(down) occupying the sites of the fcc lattice. The simplest structure is AF-I [Fig. 3.1(a)] with alternating Ag-Q and Sb-Q planes normal to the [100] direction. AF-III [Fig. 3.1(d)] can be obtained from AF-I by doubling the unit cell along the z-direction and interchanging Ag and Sb atoms in the third and the fourth Ag-Sb-Q xy-planes starting from the top. This leads to a mixing of Ag and Sb atoms in the Ag-Q and Sb-Q planes of AF-I. AF-III still has Ag-Q-Ag... and Sb-Q-Sb... chains (along the x and y directions). It turns out that

AF-III with bct symmetry is the ground state structure obtained in MC simulation studies of the CLG model [42]. In order to disrupt the above chains and to see how they control the energetics, I constructed an interrupted chain (ic) model (AF-IIb) that has sequence of Sb-Q-Ag-Q-Sb... chains in all three directions [Fig. 3.1(c)]. AF-IIb can also be visualized as alternating Ag-Sb and Q planes normal to the [111] direction. Finally, AF-II with alternating Ag, Q, and Sb planes normal to the [111] direction [Fig. 3.1(b)] is obtained from AF-IIb by rotating the second and the fourth layers of AF-IIb by 90° around the z-axis. AF-II also has interrupted chains along the x, y, and z directions. I will discuss how the presence of Ag in the Sb-Q-Sb... chains affects the electronic structure near the Fermi energy (ϵ_F) and the energetics.

The orderings of Ag and Sb on the cation sublattice of AF-I, AF-II, AF-IIb, and AF-III are the type-I, type-II, type-IIb, and type-III AF orderings, respectively, which have been found, for example, in the nearest neighbor (n.n.) and next-nearest neighbor (n.n.n.) Ising model on an fcc lattice [39]. As discussed in Chapter 2, the Hamiltonian for this model is given by,

$$H = J \sum_{n.n.} \sigma_i \sigma_j - \alpha J \sum_{n.n.n.} \sigma_i \sigma_j, \tag{3.1}$$

where $\sigma_i = \pm 1$ and $J > 0$ (antiferromagnetic n.n. interaction). AF-I was found to be the ground state for $\alpha > 0$, i.e., for ferromagnetic next nearest neighbor interaction. For negative values of α the ground states were: AF-III for $-0.5 < \alpha < 0$; AF-II and AF-IIb for $\alpha < -0.5$. AF-II and AF-IIb are degenerate. In fact, these ordered structures have been studied in several different systems. Allen and Cahn [79] found AF-II and AF-III (among several other structures) to be the ground state structures in ordered fcc binary alloys using a model where they assumed only n.n. and n.n.n. pairwise interactions between the atoms. These two structures were named "CuPt" and "CuAuII", respectively. In Li_xCoO_2, a positive electrode (cathode) material in rechargeable Li batteries, many different ordered structures of the cation

sublattice have been studied by Wolverton and Zunger [80]. Among these are AF-I, AF-II, AF-IIb, and AF-III which have been named "CA" (CuAu-type), "CP" (CuPt-type), "D4", and "Z2", respectively, in their works. AF-I and AF-II were used in the crystal structure refinements of $AgSbTe_2$ [17].

3.2.2 Structural Properties and Energetics

Structural optimization, total energy and electronic structure calculations were performed within DFT formalism using GGA and PAW as implemented in the VASP package [57] (see the previous chapters for more computational details). In several cases I have also used all-electron full-potential linearized augmented plane-wave (FP-LAPW) [81] method incorporated in the WIEN2k package [82] to substantiate our PAW results. After cell shape and ion position relaxations, all the structures of $AgSbQ_2$ (except AF-IIb) are found to change their lattice parameters from their initial values obtained after only volume optimization. The cubic AF-I ($Pm\bar{3}m$; 8 atoms/cell) becomes tetragonal with a=6.1502 Å and c/a=0.9853 for Q=Te; a=5.8141 Å, c/a=0.9773 (Q=Se); and a=5.6076 Å, c/a=0.9642 (Q=S). Except for a small distortion, the results agree well with the available data in the literature where it has been reported that $AgSbTe_2$ crystallized in the fcc NaCl structure (at least in their high-temperature modification) [64, 17]. There are inter-layer contraction (1.0% in the Ag-Te and Sb-Te bonds) along the x direction (normal to the Ag-Te and Sb-Te planes) and inter-layer expansion (0.5% in the Ag-Te and Sb-Te bonds) along the y and z direction [Fig. 3.1(a)]. Similar contraction and expansion are observed in AF-III with Te atoms moving slightly towards Ag (Ag-Te bonds are 0.4% shorter than those of Sb-Te). Ag-Q bonds are also shorter than Sb-Q in AF-II and AF-IIb for Q=Te (2.9%) and Se (1.2%), whereas Ag-S bonds are longer than Sb-S bonds by ~0.2%. Relaxation energy decreases in going from Te→Se→S; in AF-II (AF-IIb) it is 37.38 meV (38.63 meV) for Te, 5.35 meV (5.41 meV) for Se, and 0.06 meV (0.74

Table 3.1: Structural properties of the primitive cells, and total energies (E) and their differences (ΔE) of different ordered structures of AgSbQ_2 (Q=Te, Se, S); f.u.=AgSbQ_2. The primitive cells of AF-I, AF-II, AF-IIb, and AF-III structures are simple tetragonal (st; $P4/mmm$, 4 atoms/cell), trigonal (rhomboedric; $R\bar{3}m$, 4 atoms/cell), face-centered cubic (fcc; $F\bar{3}dm$, 16 atoms/cell), and body-centered tetragonal (bct; $I4_1/amd$, 8 atoms/cell), respectively. The structures are fully relaxed (volume, cell shape and positions of ions).

	Structure	Lattice parameters (Å)	E (eV/f.u.)	ΔE (eV/f.u.)
$AgSbTe_2$	AF-I	a=4.3557, c=6.0473	−13.7039	0.1956
	AF-II	a=4.3842, c=21.0118	−13.8958	0.0037
	AF-IIb	a=12.3050	−13.8995	0
	AF-III	a=6.1074, c=12.3388	−13.8251	0.0744
$AgSbSe_2$	AF-I	a= 4.1176 Å, c= 5.6652 Å	−14.5782	0.2138
	AF-II	a= 4.1256 Å, c=19.9373 Å	−14.7920	0
	AF-IIb	a=11.6150 Å	−14.7907	0.0013
	AF-III	a= 5.7347 Å, c=11.7374 Å	−14.7335	0.0585
$AgSbS_2$	AF-I	a= 3.9612 Å, c= 5.4184 Å	−15.6113	0.2448
	AF-II	a= 3.9641 Å, c=19.1091 Å	−15.8561	0
	AF-IIb	a=11.1500 Å	−15.8545	0.0016
	AF-III	a= 5.4760 Å, c=11.3714 Å	−15.8147	0.0041

meV) for S. This reflects the ionicity trend of these chalcogens (ionicity increases in going from Te→Se→S).

The primitive cells of AF-I, AF-II, AF-IIb, and AF-III are, respectively, simple tetragonal ($P4/mmm$, 4 atoms/cell), rhombohedral ($R\bar{3}m$, 4 atoms/cell), fcc ($F\bar{3}dm$, 16 atoms/cell), and bct ($I4_1/amd$, 8 atoms/cell). Table 3.1 lists the calculated lattice parameters for AgSbQ_2. The values for AF-I and AF-II structures are in excellent agreement with the XRD refinement results of $AgSbTe_2$ using the $P4/mmm$ and the $R\bar{3}m$ space groups, respectively, where the former gives a=4.2898(6) and c=6.0667(9), and the latter gives a=4.2898(6) and c=21.016(4) [17].

Energetically, AF-IIb has the lowest energy for $AgSbTe_2$; however, the energy difference between AF-II and AF-IIb is small, ΔE$\sim$4 meV/f.u. (f.u.=formula unit). AF-I turns out to be the highest energy structure; $\sim$196 meV/f.u. higher than AF-IIb and $\sim$121 meV/f.u. higher than AF-III (see Table 3.1). As will be made clear later,

the physical reason why AF-II and AF-IIb have lower energies is the presence of Ag in the Sb-Te-Sb... chains similar to the idea presented in Chapter 2 in connection with the ic model of LAST-2 (see Fig. 2.17). The Ag in the chains strongly perturbs the hybridized Sb and Te p-bands. This leads to a rearrangement in the DOS by shifting states near ϵ_F ($\sim$ -0.5 eV to 0 eV) to lower energy. Also it leads to an enhanced pseudogap feature near ϵ_F (for Q=Te) and a gap (Q=Se and S; see the next section). In the case of $AgSbSe_2$ and $AgSbS_2$, the rhombohedral AF-II is found to be the lowest energy structure; again the energy difference between AF-II and AF-IIb is small, ΔE=1.3, 1.6 meV/f.u for Q=Se and S, respectively; AF-II and AF-IIb are almost degenerate. For comparison, the chalcopyrite structure [68] is found to give for $AgSbTe_2$ considerably ($\sim$0.5 eV/f.u.) higher energy than those discussed here.

Summarizing the structural aspects, the theoretical calculations support the $R\bar{3}m$ picture among the three space groups used in the XRD refinement of $AgSbTe_2$. However, it will be interesting to re-analyze the data using the $F\bar{3}dm$ space group to see if this gives a superior fit. The AF-III structure found in MC simulations of the CLG model as the lowest energy structure [42] is not so here. However, it turns out that it has the lowest electrostatic energy. The *ab initio* studies clearly indicate that covalency effects play a significant role in the energetics of different ordered structures.

As will be made clear in the next section, the low energy structures, AF-II and AF-IIb, were constructed based on the understanding of the formation of the electronic states near ϵ_F in AF-I and AF-III. Extensive investigation of other structures (up to 64 atoms/supercell) which are the derivatives of AF-II and AF-IIb were also carried out, but no other structure which has lower energy than AF-II (Q=Se, S) or AF-IIb (Q=Te) was found. AF-I, AF-II, AF-IIb, and AF-III are, therefore, the best choices for our current studies. Exploring different ordered structures is essential in these chalcogenides, because in real samples one might have either a particular

ordered structure or a mixture of several ordered structures depending on the synthesis conditions. Experimental data may look controversial because of that. In fact, one may not even access the lowest energy structure because of kinetics. Besides, X-ray and neutron diffractions may not be able to differentiate between similar ordered structures because of the very similar form factors of Ag and Sb.

3.2.3 Electronic *vis-à-vis* Atomic Structures

We now discuss the bonding, semiconducting or semi-metallic nature of the compounds and the role Ag plays in determining this. The DOS of $AgSbTe_2$ in AF-I and AF-III are found to have pseudogap-like features with large DOS above ϵ_F at

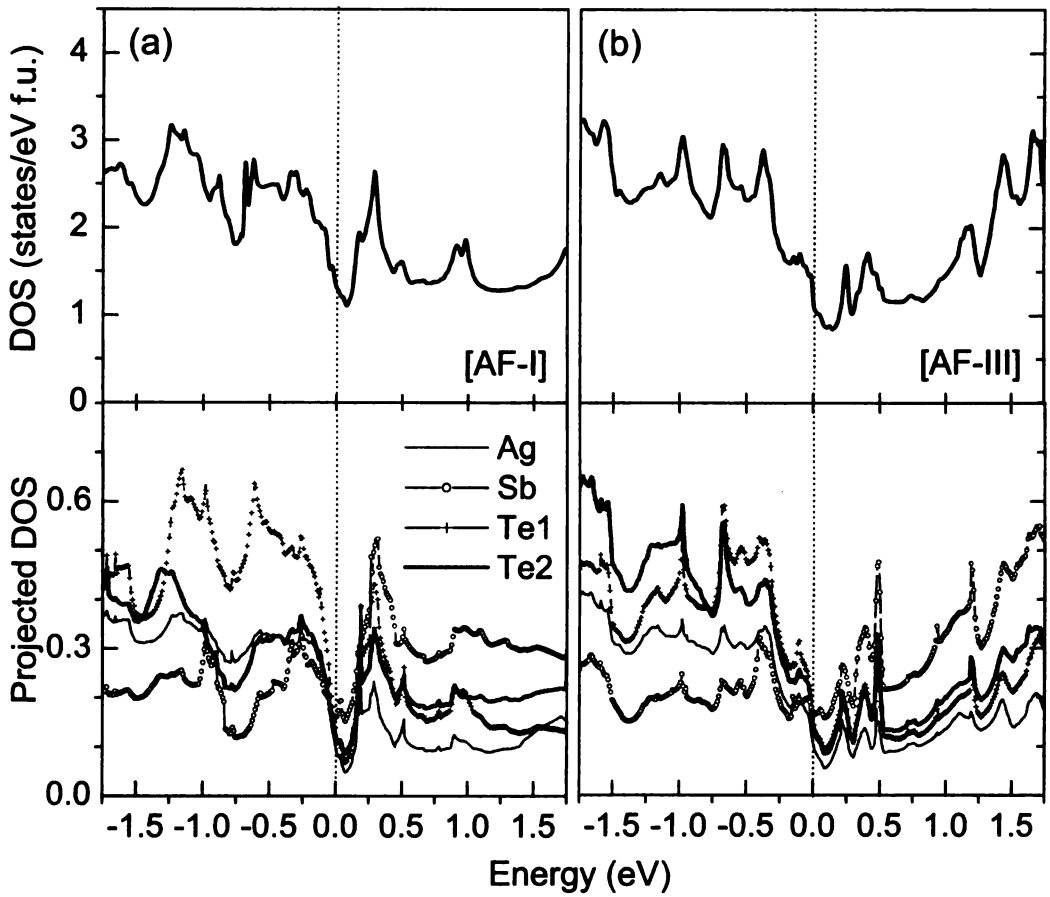

Figure 3.2: DOS and PDOS of $AgSbTe_2$ in (a) AF-I and (b) AF-III. The Fermi energy (ϵ_F, at 0 eV) is set at the highest occupied state; f.u.=$AgSbTe_2$.

$\sim$0.2-0.5 eV [Figs. 3.2(a) and 3.2(b)]. The minima near ϵ_F have $\sim$1 states/eV f.u. (f.u.=$AgSbTe_2$). ϵ_F lies in the rapidly decreasing part of the DOS near the pseusogap region. A careful analysis of the projected DOS [Figs. 3.2(a) and 3.2(b)] and band characters shows that there is a strong hybridization between p states of Sb and those of Te coming from the Sb-Te planes (in AF-I). These hybridized states predominantly contribute to the region near ϵ_F in addition to the p states of Te coming from the Ag-Te planes. In going from AF-I to AF-III, the DOS near ϵ_F coming from Sb and Te p states are significantly suppressed. The suppression of the DOS (especially those states coming from Sb) indicates that the presence of Ag in the Sb-Te-Sb... chains in AF-III (which was made from AF-I by mixing Ag and Sb atoms in the Ag-Te and Sb-Te planes of AF-I) plays a role in controlling the DOS near ϵ_F. The energy is lower in AF-III (by $\sim$120 meV/f.u. compared to AF-I) because there is a transfer of DOS just below ϵ_F (predominantly Te2 p states coming from the Sb-Te planes in AF-I) to lower energies. A natural question arises: can we manipulate these states to further lower the DOS in the pseudogap region by changing the ordering of Ag and Sb in these systems or even open up a real gap?

Fig. 3.3(a) shows the total DOS of $AgSbTe_2$ in the AF-II and AF-IIb structures. In both cases, although there is no real gap in the DOS, the peaks just above ϵ_F (found in AF-I and AF-III) disappear, there is a suppression of the DOS below ϵ_F, and the pseudogap feature is enhanced. The projected DOS analysis [Fig. 3.3(b)] shows that the states in the region near ϵ_F coming from the Sb and Te atoms have been suppressed drastically compared to AF-I and AF-III. Thus interruption of the Sb-Te-Sb... chains by Ag (now in all three directions) helps in developing a true pseudogap structure.

There are several generic features of the total DOS. The pseudogap structure in AF-IIb changes to a gapped one in going from Te to Se and S [see Figs. 3.4(b) and 3.4(d)]. There are 2 sharp peaks in the total DOS, one below ϵ_F by $\sim$0.1 eV with a

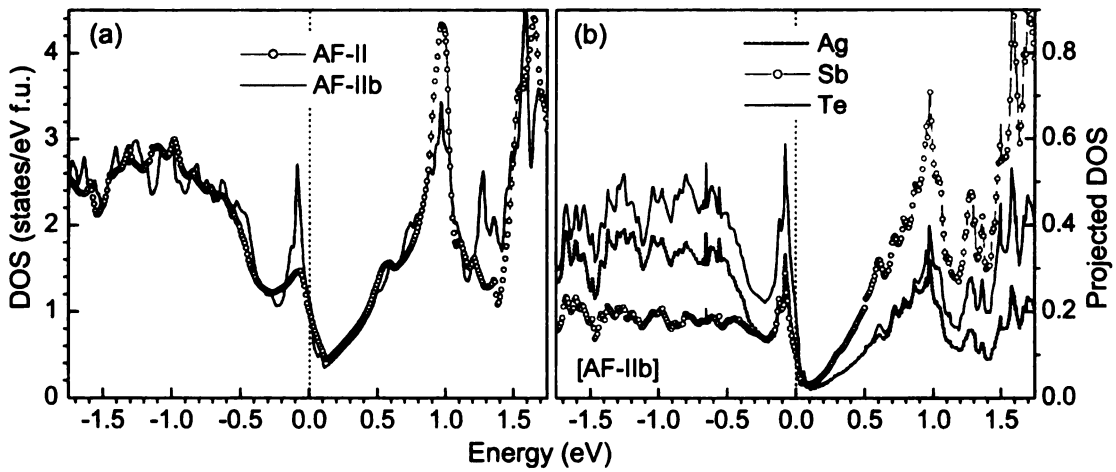

Figure 3.3: (a) DOS of $AgSbTe_2$ in AF-II and AF-IIb, and (b) PDOS of $AgSbTe_2$ in AF-IIb. The Fermi energy (ϵ_F, at 0 eV) is set at the highest occupied state; f.u.=$AgSbTe_2$.

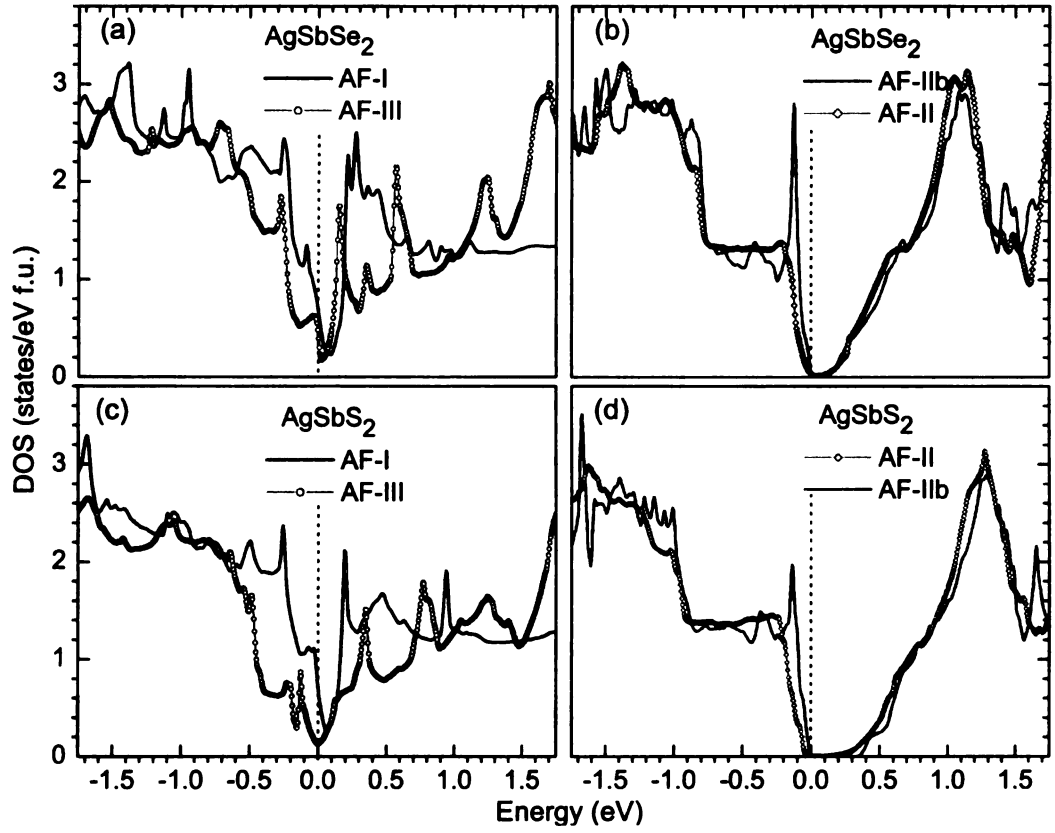

Figure 3.4: DOS of $AgSbQ_2$ (Q=Se and S) in AF-I, AF-II, AF-IIb, and AF-III. The Fermi energy (ϵ_F, at 0 eV) is set at the highest occupied state; f.u.=$AgSbQ_2$.

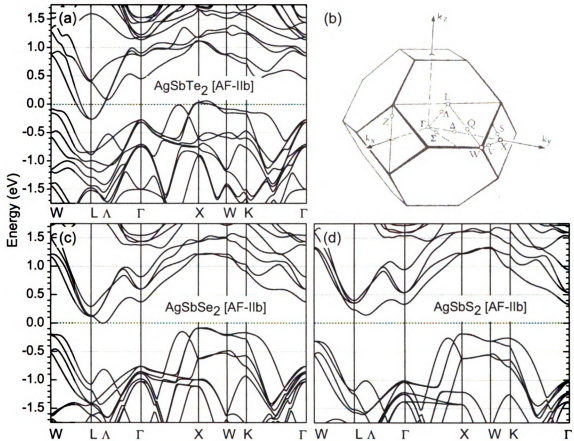

Figure 3.5: Band structure of $AgSbQ_2$(Q= Te, Se, S) along the high symmetry lines of the Brillouin zone of the fcc AF-IIb structure.

width of ~0.15 eV, and the other at about 1.0 eV above ϵ_F of much broader width. The latter is formed predominantly by Sb p states (hybridized with Ag s and Q p states) while the former is predominantly by the Q p states (hybridized with Ag d and Sb p states). Similar features are also seen in AF-II, but the lower energy peak is suppressed and there is a transfer of spectral weight to the higher one. The energy gap is ~0 eV (AF-II) or 0.08 eV (AF-IIb) for the selenide, whereas it is 0.10 eV (AF-II) or 0.32 eV (AF-IIb) for the sulfide. AF-I and AF-III still give $AgSbSe_2$ and $AgSbS_2$ pseudogaps (negative gaps), although they are more pronounced than those in $AgSbTe_2$ [see Figs. 3.4(a) and 3.4(c)]. Spin-orbit interaction (SOI) does not have significant effect on the total DOS near ϵ_F.

Fig. 3.5(a) shows the band structure of $AgSbTe_2$ (in AF-IIb) along the high sym-

metry directions of the fcc Brillouin zone (BZ) [83] (a=12.305 Å). The fcc BZ with the special **k**-points is also given in Fig. 3.5(b). In both AF-II and AF-IIb, the top of the valence band is found to be predominantly p states of the chalcogenide (hybridized with the Sb p and Ag d states). Ag plays a very interesting role. In addition to helping suppress Sb p and Te p hybridization (as compared to AF-I and AF-III), its s state, which strongly hybridizes with Sb p states near the L point, has a large dispersion. For simplicity, this band will be referred to as the "Ag s band", which is the broadly dispersed conduction band coming across ϵ_F, centered at the L point and not split by SOI. If this band was not there, the system would be a semiconductor. However it comes down and goes below the top of the valence band and the system becomes a semimetal (negative-gap semiconductor or pseudogap system). In going from Te to Se and S, the relative separation of the "Ag s band" and the valence band increases and the latter two systems are semiconductors [Figs. 3.5(c) and 3.5(d)]. The conduction band minimum (CBM) of the selenide and sulfide is however no longer at the L point, but somewhere between the L point and Λ point. The separation between the conduction band bottom (which is predominantly Q p states) and valence band top (predominantly Sb p) increases in going from Te and Se to S. This is in the right trend with the relative positions of the p levels of the chalcogens and Sb given in the Harrison's *Solid-State Table*; these energy levels are: -8.14 eV (Sb $5p$), -9.54 eV (Te $5p$), -10.68 eV (Se $4p$), and -11.60 eV (S $3p$) [84].

To get a good narrow band-gap semiconductor, in stead of replacing Te by Se or S one can replace Ag by another monovalent cation with higher s state energy (such as Na and K, as will be presented in the next section). One can also replace Ag by Cu to manipulate the narrow peak below ϵ_F through its d-level. The DOS of $CuSbTe_2$ in the hypothetical AF-IIb structure resembles very well that of $AgSbTe_2$. The minimum of the pseudogap in the case of $CuSbTe_2$ is not as deep because the Cu $4s$ level is lower in energy compared to Ag $5s$ resulting in a small increase in the

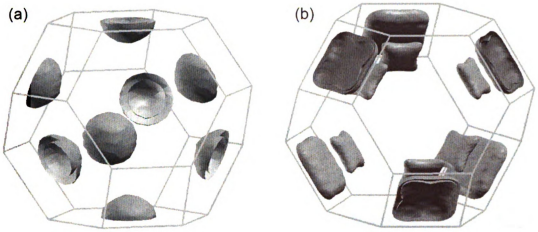

Figure 3.6: Fermi surfaces of $AgSbTe_2$ in AF-IIb: (a) electron pockets centered around the L points (centers of the hexagons), and (b) hole pockets centered around the X points (centers of the squares).

DOS in the pseudogap region. $CuSbTe_2$ is, however, still a good candidate for high performance thermoelectric since it is Ag-free. Experimentally, $CuSbTe_2$ is reported to possess a Bi_2Te_3-like hexagonal structure with a=4.22 Å and c=29.9 Å (at 300 K) [85]. For $AuSbTe_2$, the pseudogap feature is much less pronounced because the Au d level (which is higher in energy than Ag d) pushes Te p states upwards and enhances the DOS near ϵ_F. This system behaves more like a metal and is not likely to be a good thermoelectric.

In the AF-IIb telluride, one has light electron pockets centered around the L points and heavy hole pockets centered around the X points; see the band structure in Fig. 3.5(a) and the Fermi surfaces in Figs. 3.6(a) and 3.6(b). This compound appears to be a classic semimetal. Both electrons and holes will contribute to transport properties. Since the valence band maximum is quite flat, the holes are expected to be heavy compared to the electrons. In addition, there is a multi-peak valence band structure with anisotropic band maxima. These will result in a large positive thermopower [59] as seen in experiments [65]. In the Se and S compounds, the band gap is indirect, the conduction band minimum is Sb-Se or Sb-S derived and lie along the Λ-line; these gaps are respectively 0.08 eV and 0.32 eV. AF-II gives for $AgSbTe_2$

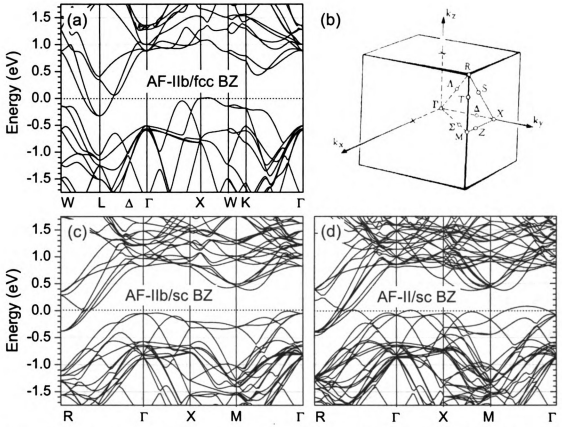

Figure 3.7: Band structure of $AgSbTe_2$ in sc Brillouin zone (BZ): AF-II [figure (d)] and AF-IIb [figure (c)]. The results obtained in calculations using 64-atom supercells; spin-orbit interaction (SOI) was not included. Band structure of $AgSbTe_2$ in fcc BZ without SOI [figure (a)] is also included for comparison.

similar band structure with electron pockets at the L points and hole pockets near the T points (of the rhombohedral BZ) and a multi-peak valence band structure. However there are also some differences due to the different Ag/Sb/Q connectivities in these two structures.

For the sake of comparison, the band structures of $AgSbTe_2$ in AF-II and AF-IIb using sc supercells with the same number of atoms and the same lattice constant (a=12.24 Å) have been calculated. The band structures are then projected on the sc BZ [see Fig. 3.7]. This sc BZ is 4 times smaller than the fcc BZ we have discussed above. The basic difference between AF-II and AF-IIb is along the R-Γ line. There is band overlap in the case of AF-II, whereas the conduction band minimum coming

down across ϵ_F without touching the valence band bottom in the case of AF-IIb.

3.2.4 Calculated Band Gap *vis-à-vis* Experiment

It is well known that most DFT calculations tend to underestimate the band gaps of semiconductors [23], and one can not exclude the possibility that $AgSbTe_2$ is a semiconductor with a small band gap.[1] To resolve this "band gap problem" associated with the present DFT calculations, experimental measurements have been carried out on carefully made $AgSbTe_2$ samples.[2] The samples were synthesized by combining the elements in their stoichiometric ratio on the 50 mmol scale in a 9 mm fused silica tube. The reactants were heated to 850°C over the course of 10 h then soaked at this temperature for 72 h with mechanical agitation to ensure a homogenous distribution of the elements within the melt. The samples were then cooled to room temperature over the course of 2 h to minimize the formation of secondary phases such as Ag_2Te and Sb_2Te_3; well-formed ingots with shiny surfaces were obtained. Electrical conductivity measurements were performed in the temperature range 10-573 K using standard four-probe techniques and the results are given in Fig. 3.8. The electrical conductivity (σ) increases with increasing T and reaches its maximum (of $\sim$38 $\mathrm{S\,cm^{-1}}$) at $\sim$170 K, it then decreases and reaches its minimum (of $\sim$19 $\mathrm{S\,cm^{-1}}$) at $\sim$473 K and then increases again with increasing T. Estimation of the activation energies gives a band gap of $\sim$0.1 eV in the intrinsic (high T) range and an impurity binding energy of $\sim$1-2 meV in the extrinsic (low T) range. This suggests that $AgSbTe_2$ is a narrow band-gap semiconductor.

To further confirm the gap picture, heat capacity [87] and magnetic susceptibility [61] measurements were carried out on the same sample. The latter shows a weak T-dependent diamagnetism and the former gives a very small γ-factor indicating that

[1] Bagayoko, Zhao, and Williams (BZW), however, have claimed that the "band gap problem" is not intrinsic to DFT; rather they ascribe most of the gap underestimation to a combined basis set and variational effect in solving the Kohn-Sham equations; see Ref. [86].

[2] In collaboration with J. R. Salvador and M. G. Kanatzidis.

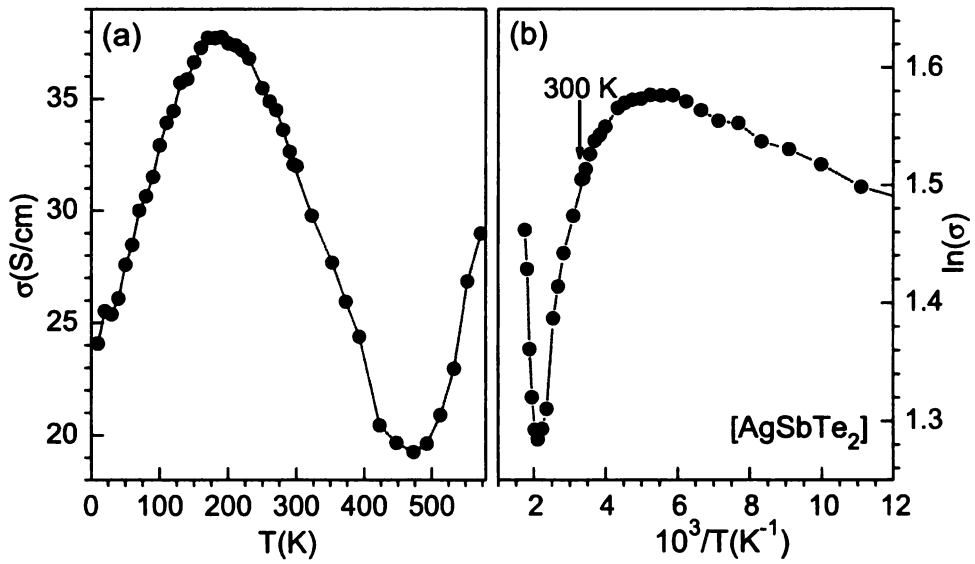

Figure 3.8: Electrical conductivity (σ, in S cm^{-1}) as a function of temperature measured in a $AgSbTe_2$ sample.

there are no or very few electronic states near ϵ_F. The discrepancy between the experimental data and the calculated band structure can be ascribed to the deficiency of the current DFT calculations in obtaining a true gap. In this case, because of the diffuse nature of Te p orbitals, and also that of Ag s, our calculations give a negative band gap (of ~ -0.3 eV). The Se(S) compounds suffer less in this regard and give gaps which are however smaller than their true ones. Improvements beyond present DFT calculations [23] can give a better picture of the gap structure. Indeed DFT calculations within screened-exchange local density approximation (sx-LDA) [88] carried out recently[3] gives $AgSbTe_2$ in AF-II and AF-IIb an almost zero gap. All the features of the DFT-GGA band structures of $AgSbTe_2$ are preserved in the sx-LDA calculations, except there is a almost rigid relative shift (away from one another) of the valence band (including the "hole pocket" in the GGA band structure near the X point) and the conduction band (including the "electron pocket" centered at L) [89].

Recent measurements by Heremans *et al.* [90] on carefully made single crystals of

[3]In collaboration with L. Ye and A. Freeman.

$AgSbTe_2$ show that $AgSbTe_2$ is a semiconductor with a very small gap (~7 meV at 77 K). Hole density (5×10^{19} cm^{-3} at 300 K) is much higher than electron density (by factor of 500) and hole mobility (12 cm^2/Vs) is much lower than that of electrons (2200 cm^2/Vs). These appear to be consistent with the calculated band structure discussed above.

3.2.5 Native Point Defects and Disorder

There are still some issues that need to be addressed. Why $AgSbTe_2$ has a p-type conductivity even in nominally undoped samples? Why there are few, if any, n-type $AgSbTe_2$ samples which have been made successfully? Let us assume that $AgSbTe_2$ can be either a semimetal, a zero-gap semiconductor, or a semiconductor with a small but finite band gap depending on the the synthesis conditions. If there is a gap in the system one should consider if there are defects, especially native point defects, and what role the defects play in determining carrier concentration in the system. To the best of my knowledge, there are no studies on defects in $AgSbQ_2$.

Native point defects. —Among serveral kinds of defects, vacancies at the Ag, Sb, or Te site seem to be most plausible. To see if any of these vacancies is energetically favorable, defect energy calculations were carried out in the AF-IIb structure. A vacancy was created by removing one atom from a 64-atom AF-IIb supercell. The composition of the new supercell was then $Ag_{15}Sb_{16}Te_{32}$ (Ag vacancy), $Ag_{16}Sb_{15}Te_{32}$ (Sb vacancy), or $Ag_{16}Sb_{16}Te_{31}$ (Te vacancy). SOI was not included in these calculations since it does not significantly affect the DOS near ϵ_F and the energy difference between different structures. However, relaxation effects are important. After relaxation, the total energy of the supercell (which includes the vacancy) is decreased by 0.622 eV (~0.3%), 0.896 eV (~0.4%), and 0.885 eV (~0.4%) for Ag, Sb, and Te vacancies, respectively.

The formation energy (E_f^v) of a vacancy V_X at the X site (X=Ag, Sb, and Te)

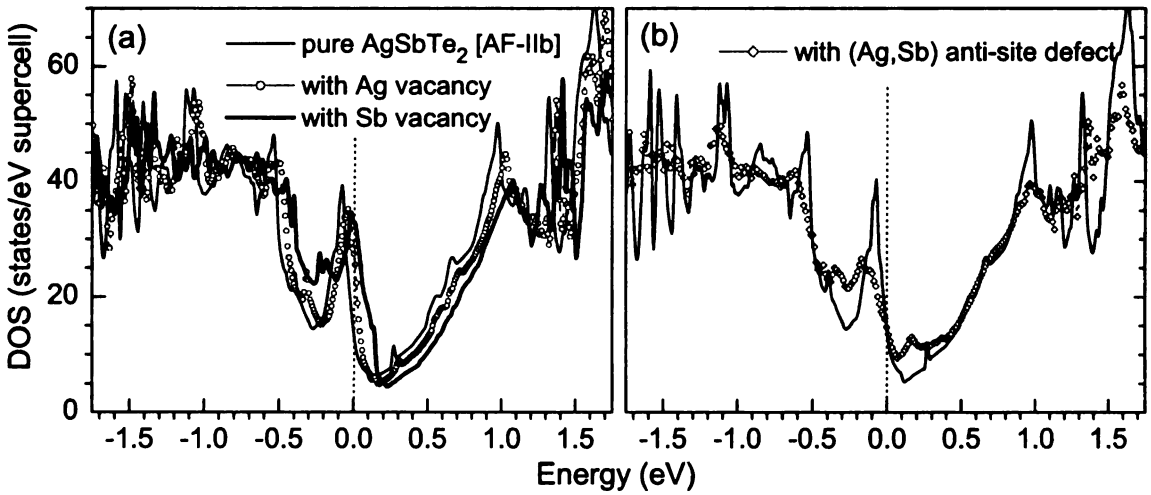

Figure 3.9: DOS of a 64-site supercell of $AgSbTe_2$ (AF-IIb) with the presence of (a) a Ag vacancy or (b) a (Ag,Sb) anti-site defect. The Fermi energy (ϵ_F, at 0 eV) is set to the highest occupied state.

is defined as [91]

$$E_f^v = E_0^v - E_0 + \mu_X, \tag{3.2}$$

where E_0^v and E_0 are, respectively, the total energy of the supercell with and without the vacancy V_X and μ_X is the chemical potential of X; μ_X is calculated as the energy per atom in each standard metallic state. The calculations give $E_f^v \sim 0.023$ eV/vacancy (for Ag vacancy), 0.439 eV/vacancy (Sb vacancy), and 1.244 eV/vacancy (Te vacancy). The formation energy of the Ag vacancy is very small suggesting that $AgSbTe_2$ samples are prone to this native defect. Experimentally, this seems to be the case since it was showed that $AgSbTe_2$ systematically displayed a cationic defect in different samples and that its corresponding formula was rather $Ag_{19}Sb_{29}Te_{52}$ [65]. Sb and Te vacancies are energetically less favorable in the system. Having Ag vacancy is also consistent with the observed p-type conductivity (see below).

It is important to see how the electronic structure of $AgSbTe_2$ gets modified in the presence of vacancies. Fig. 3.9(a) shows the total DOS of $AgSbTe_2$ with a Ag vacancy; DOS of pure $AgSbTe_2$ is also provided for comparison. The two curves resembles each other very well in the region near ϵ_F except for a small rigid shift. This means that

Ag vacancy simply shifts ϵ_F downward in energy to take care of the missing electron due to the removal of the Ag atom to create the vacancy. Combining with the above energetic studies, one can conclude that Ag vacancies are responsible for the p-type conductivity and the high hole concentration in $AgSbTe_2$ samples [65, 90]. Sb vacancy also makes $AgSbTe_2$ behave like p-type semiconductor, although it is energetically less favorable. The shift of ϵ_F is even larger since there are three electrons which are removed for each Sb. In addition, there is rearrangement of electronic states in the region near ϵ_F which puts more states into the region below ϵ_F [Fig. 3.9(a)]. Te vacancy, on the other hand, shifts ϵ_F upward in energy that could make the system behave like a n-type semiconductor. It also disturbs the DOS near ϵ_F significantly and puts more states near the minima (present in the pure system) and near ϵ_F. However, as just discussed above, Te vacancies are not likely to be present in $AgSbTe_2$ due to their high formation energy.

Disorder. —Due to the near degeneracy of AF-II and AF-IIb, one might expect to see mixed phases and disorder effects in the system. To examine the latter, calculations were carried out for (Ag, Sb) antisite defects. A supercell model for these defect calculations were constructed starting from a 64-atom supercell of AF-IIb and interchanged one Ag and one (nearest) Sb atoms. This created some kind of defect complex and "disorder" in the supercell. As seen in Fig. 3.9, the DOS are sensitive to the defect. There is an enhancement of the DOS near ϵ_F and the energy is higher by $\sim$20 meV/defect. This should increase the low T heat capacity. In view of the fact that the measured low T γ value is extremely small [87], I believe that disorder effects are not very significant in the samples under investigation, although energetically it is possible to have the antisite defect (the energy difference is $\sim$20 meV/defect in a 64-atom supercell). Theoretically, disorder in the systems can lead to gap opening, as it was reported in the case of (Pb,Sn)Te, alloys of PbTe and SnTe [92]. It is found that ordered structures give semimetals for some Pb/Sn ratios of these alloys,

whereas disorder opens up a gap. To check this, Ag and Sb in the above supercell have also been allowed to be randomly distributed using "special quasi-random structure" (SQS) scheme proposed by Zunger *et al.* [93] and incorporated in the *Alloy Theoretic Automated Toolkit* (ATAT) [94]. The preliminary results, however, show that this "disorder" just introduces more electronic states in the region near the Fermi energy and makes $AgSbTe_2$ more metallic.

3.3 Other I-V-VI_2 Ternary Chalcogenides

3.3.1 Atomic Structure and Energetics

Some Na-based I-V-VI_2 ternary chalcogenides were prepared and their structures determined about three decades ago by Eisenmann and Schäfer [66]. They reported that $NaSbSe_2$, $NaSbTe_2$, and $NaBiTe_2$ compounds had NaCl structure with the lattice constant $a = 5.966(2)$ ($NaSbSe_2$), 6.317(2) ($NaSbTe_2$), and 6.366(3) Å ($NaBiTe_2$). $NaAsSe_2$, on the other hand, crystallized in a orthorhombic structure with a=5.83±0.01, b=24.27 ±0.05, and c=11.82±0.02 Å; space group *Pbca*. To the best of my knowledge, there has been no reported information about $KSbTe_2$, although the structural properties of the other K-based ternary chalcogenides are available in literature; for example $KAsSe_2$ crystallizes in monoclinic structure (space group Cc) [95] and $KSbSe_2$ can be described by the space group $C2/m$ [96]. There is no information about atomic ordering on the cation (Na) sublattice in these compounds. As regards $AgBiQ_2$ compounds, which were discovered probably at the same time as $AgSbQ_2$, they were reported to possess a statistically disordered NaCl-type structure at high temperatures and a rhombohedral structure at room temperature [64].

In this section, I present the results for $NaSbTe_2$, $KSbTe_2$, $AgAsTe_2$, and $AgBiTe_2$. These four systems are chosen to see how the band gap and electronic structures change by manipulating the two different types of cations, the monovalent and the

Table 3.2: Structural properties, total energies (E) and their differences (ΔE) of different ordered structures of several compounds in the ABQ_2 series (A=Na, K, Ag; B=As, Sb, Bi; Q=Te); f.u.=ABQ_2. The primitive cells of AF-I, AF-II, AF-IIb, and AF-III structures are simple tetragonal (st; $P4/mmm$, 4 atoms/cell), trigonal (rhombohedral; $R\bar{3}m$, 4 atoms/cell), face-centered cubic (fcc; $F\bar{3}dm$, 16 atoms/cell), and body-centered tetragonal (bct; $I4_1/amd$, 8 atoms/cell), respectively. The structures are fully relaxed (volume, cell shape and positions of ions).

Compound	Structure	Lattice parameters	E (eV/f.u.)	ΔE (eV/f.u.)
$NaSbTe_2$	AF-I	a= 4.4608 Å, c= 6.1577 Å	−13.4855	0.3244
	AF-II	a= 4.3896 Å, c=22.4228 Å	−13.8099	0
	AF-IIb	a=12.5950 Å	−13.7989	0.0110
	AF-III	a= 6.1942 Å, c=12.8177 Å	−13.7002	0.1097
$KSbTe_2$	AF-I	a= 4.6605 Å, c= 6.4203 Å	−12.8183	0.8326
	AF-II	a= 4.4250 Å, c=24.6304 Å	−13.7509	0
	AF-IIb	a=13.0600 Å	−13.6524	0.0985
	AF-III	a= 6.4440 Å, c=13.3982 Å	−13.2607	0.4902
$AgAsTe_2$	AF-I	a= 4.1816 Å, c= 5.8644 Å	−13.9832	0.0886
	AF-II	a= 4.1955 Å, c=20.4147 Å	−14.0646	0.0072
	AF-IIb	a=11.8350 Å	−14.0718	0
	AF-III	a= 5.8292 Å, c=12.0881 Å	−14.0621	0.0097
$AgBiTe_2$	AF-I	a= 4.4420 Å, c= 6.1470 Å	−14.0655	0.2975
	AF-II	a= 4.4654 Å, c=21.3798 Å	−14.3629	0
	AF-IIb	a=12.5400 Å	−14.3624	0.0005
	AF-III	a= 6.2493 Å, c=12.4665 Å	−14.2070	0.1559

trivalent. These calculations were carried out by employing the same approach which was used successfully for AgSbQ_2 (Q=S, Se, Te); that is to explore different possible ordered structures and find the one(s) with the lowest energy. AF-I, AF-II, AF-IIb, and AF-III structures were reemployed for this purpose. I have investigated the interplay of atomic and electronic structures and the formation of the electronic states in the band gap, to see how all these change as one replaces one constituent element with another. I have analyzed the changes as one varies Q in the ABQ_2 series in the previous section; I now keep Q fixed (Q=Te) and vary either A (Ag→Na, K) or B (Sb→As, Bi).

The structural properties, total energies and their differences between different

ordered structures of $NaSbTe_2$, $KSbTe_2$, $AgAsTe_2$, and $AgBiTe_2$ are summarized in Table 3.2. The lowest energy structure in all these compounds is found to be either AF-II or AF-IIb. It is the AF-II (rhombohedral) structure in $NaSbTe_2$ and $KSbTe_2$ with the energy difference between AF-II and AF-IIb being rather small in the former (11 meV) and much larger in the latter ($\sim$ 100 meV). For comparison, AF-IIb (not AF-II) has the lowest energy in $AgSbTe_2$, as already discussed in the previous section. This suggests that there is a tendency for the $ASbTe_2$ compounds to adopt the rhombohedral structure if one replaces A=Ag by a more ionic element (such as Na and K). If, instead of changing the cation on the A site, one changes the B site cation, $AgBTe_2$ (B=As, Sb, Bi), one finds that AF-II and AF-IIb structures are almost degenerate. The lattice parameters for $AgBiTe_2$ in AF-II are in excellent agreement with experiment which gives a=4.37(2) Å and c=20.76(5) Å [64]. The calculated values [Table 3.2] are $\sim$2-3% larger than the experimental ones as expected since it is well known that DFT-GGA tends to overestimate the lattice parameters (by the same amounts) [21].

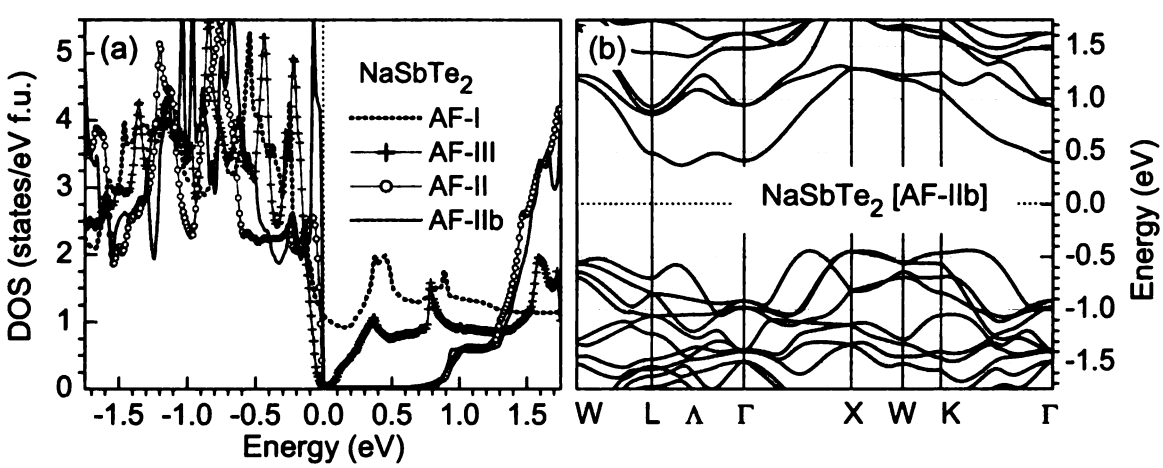

Figure 3.10: Electronic structure of $NaSbTe_2$: (a) DOS in AF-I, AF-II, AF-IIb, and AF-III, and (b) band structure in AF-IIb. The Fermi energy (ϵ_F, at 0 eV) is set to the highest occupied state or in the middle of the gap.

3.3.2 Electronic Structure

The DOS of $NaSbTe_2$ in the four different ordered structures are shown in Fig. 3.10(a). AF-I gives a pseudo gap but with a large DOS at ϵ_F, AF-III a very small (almost zero) negative gap, whereas the two other structures give gaps, 0.6 eV (AF-II) and 0.8 eV (AF-IIb). The physics of formation of the electronic states in the band gap region is similar to $AgSbTe_2$. In AF-I, the states just above ϵ_F are predominantly Sb p, whereas those at and below ϵ_F are predominantly Te p coming from the Sb-Te planes. There is a dramatic suppression of the electronic states near the Fermi energy in going from AF-I to AF-III, where there are mixing of Na and Sb in both the Na-Te and Sb-Te planes [observed in AF-I; see Fig. 3.1(a)]. However, in AF-III, the region just above ϵ_F is still predominantly Sb p. Further interruption of Sb-Te chains (in AF-III) by Na (in AF-II and AF-IIb) cleans up completely the states just above ϵ_F and opens a large gap. The top of the valence band (predominantly Te p) in the DOS is sharp in AF-IIb. The band structure of $NaSbTe_2$ reflects this feature with flat hole bands and multi-peak structure in the valence-band top [see Fig. 3.10(b)]. Because the energy level of Na s is much higher than that of Ag s (see Table 3.3), the conduction band minimum is no longer at the L point but somewhere along the Λ-line and the conduction band bottom is predominantly Sb p. Band structure of $KSbTe_2$ is very similar to that of $NaSbTe_2$. The calculations give $KSbTe_2$ band gaps of 0.02 eV (AF-III), 0.65 eV (AF-II), and 0.82 eV (AF-IIb).

Next I would like to keep the monovalent and divalent atoms fixed and vary the trivalent atom, i.e., look at $AgBTe_2$, where B= As, Sb. and Bi. The DOS of $AgAsTe_2$ in AF-II and AF-IIb are shown in Fig. 3.11(a). This compound also has pseudogap feature similar to what has been found for $AgSbTe_2$ except that there is no sharp peak just below ϵ_F. However, there are also flat hole bands centered around the X points [see Fig. 3.11(b)]. Let us look at some basis differences in the band structures of $AgAsTe_2$ and $AgSbTe_2$ [see Fig. 3.5(a)] in the same AF-IIb structure.

Table 3.3: Energy level of the s and p (or d) orbitals of several A, B, and Q elements taken from the Harrison's *Solid-State Table* (Ref. [84]).

A		Q		B	
Na	−4.96 (s)	S	−24.02 (s)	As	−18.92 (s)
	-		−11.60 (p)		−8.98 (p)
K	−4.01 (s)	Se	−22.86 (s)	Sb	−16.03 (s)
	-		−10.68 (p)		−8.14 (p)
Ag	−5.99 (s)	Te	−19.12 (s)	Bi	−15.19 (s)
	−19.23 (d)		−9.54 (p)		−7.79 (p)

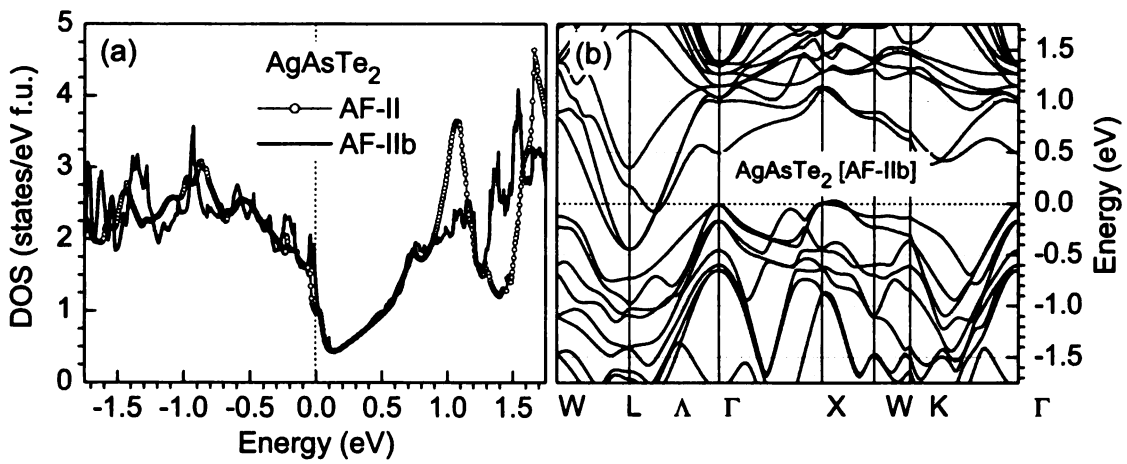

Figure 3.11: Electronic structure of $AgAsTe_2$: (a) DOS in AF-II and AF-IIb, and (b) band structure in AF-IIb. The Fermi energy (ϵ_F, at 0 eV) is set to the highest occupied state.

The top of the bands at the Γ points is much higher in energy compared to that of the Ag compound and touches the Fermi level. This contributes another peak to the valence band top, which is expected to have important implications on the transport properties of $AgAsTe_2$. The "Ag s band" centered at the L points goes down across the Fermi level and reaches ~ -0.4 eV. This makes the negative gap of $AgAsTe_2$ more negative than that of $AgSbTe_2$.

In going from As to Sb to Bi, the pseudogap gets deeper and a small gap opens up in $AgBiTe_2$ (AF-IIb) [see Fig. 3.12(a)]. AF-II gives a very small (almost zero) but a negative gap. Band structure of $AgBiTe_2$ [Fig. 3.12(b)] also shows a lot of similarity with those of the As and Sb compounds. The major differences in the band

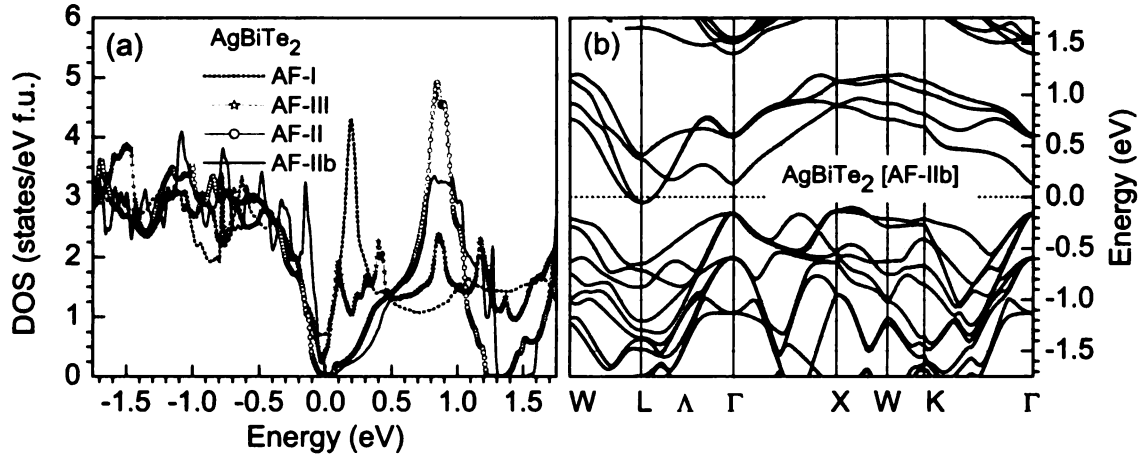

Figure 3.12: Electronic structure of $AgBiTe_2$: (a) DOS in AF-I, AF-II, AF-IIb, and AF-III, and (b) band structure in AF-IIb. The Fermi energy (ϵ_F, at 0 eV) is set to the highest occupied state.

structures of the three compounds are at the L and Γ points. The changes in going from As to Sb to Bi are: (i) the conduction band bottom at the L point moves up in addition to the overall increase in the relative separation between the conduction band bottom and the valence band top, and (ii) the peak in the valence band top at the Γ point is lowered from ϵ_F to ~0.3 eV below ϵ_F. This reflects the increasingly relative separation between the p level of trivalent atoms and that of Te in going from As to Sb to Bi. In addition to the gap (AF-IIb) or the pseudogap (AF-II), $AgBiTe_2$ also has a spin-orbit-induced gap at $\sim$ 1.3 eV above ϵ_F [see Fig. 3.12(a)]. This additional band is formed due to the the large splittings of Bi (Z=83) p orbitals in $AgBiTe_2$ resulting from spin-orbit interaction (SOI).

From a materials point of view, the features near the valence band top of $NaSbTe_2$, $KSbTe_2$, $AgAsTe_2$, and $AgBiTe_2$ are very desirable for thermoelectric applications. Flat hole bands (heavy hole masses), multi-peak structure, highly degenerate bands etc... will all result in high thermopower [59]. However, in order to get an optimal thermoelectric figure of merit (ZT) one needs to engineer the band gap further such as via doping and/or alloying. $NaSbTe_2$ and $KSbTe_2$, for example, have quite large band gaps which is not favorable for good thermoelectrics. They may be good photo-

voltaics. $AgAsTe_2$, $AgSbTe_2$, and $AgBiTe_2$ have very narrow gaps or even negative gaps (after taking into account the underestimation of our DFT-GGA calculations) which can reduce the thermopower due to minority carriers. One can replace Te in $AgAsTe_2$, for instance, by Se to have a better band gap value suitable for thermoelectric applications. Although many of these compounds have been studied in the last several decades, careful experimental studies are still needed in order to understand their fundamental properties. These theoretical studies may help the experimentalists to look at some of the promising systems more carefully.

3.4 Tl-Based III-V-VI_2 Ternary Chalcogenides

3.4.1 Structural Properties and Energetics

$TlSbTe_2$ and $TlBiTe_2$ are potentially excellent thermoelectric materials because all the atoms are heavy which is needed for low lattice thermal conductivity. These systems were first reported to have disordered NaCl-type structures [97]. Hockings and White [98] later found that these two Tl-based tellurides had ordered structures which were isostructural with the intermediate phases of $AgBiSe_2$ and $AgBiS_2$ [64]. These structures are formed by the ordering of the cations in the layers perpendicular to one of the cubic [111] directions (AF-II). Recent studies by Chrissafis *et al.* [99] have shown a solid-solid phase transformation from the rhombohedral (low temperature phase) to the cubic (high temperature phase) symmetry. Other two Bi compounds, $TlBiSe_2$ and $TlBiS_2$, were also found to possess a rhombohedral structure [100, 101]. $TlSbSe_2$ and $TlSbS_2$, on the other hand, were found to have monoclinic (MCN) and triclinic (TCN) structures, respectively [102, 103]. A summary of the experimental lattice parameters of these compounds is given in Table 3.4.

Due to the existence of the rhombohedral symmetry in the majority of the Tl-based compounds, AF-II (space group $R\bar{3}m$) [Fig. 3.1(b)] is selected for the current

Table 3.4: Structural properties, total energies (E) of different ordered structures of $TlSbQ_2$ and $TlBiQ_2$ (Q=Te, Se, S) and their differences (ΔE). The primitive cells of AF-II and AF-IIb structures are, respectively, face-centered cubic (fcc $F\bar{3}dm$, 16 atoms/cell) and rhombohedral ($R\bar{3}m$, 4 atoms/cell). MCN is monoclinic ($P2_1$, 16 atoms/cell) and TCN is triclinic ($P\bar{1}$, 16 atoms/cell). The coordinates for MCN and TCN are taken from experiments.

	Structure	Lattice parameters		Energy (eV/f.u.)	
		Calc.	Expt.	E	ΔE
$TlSbTe_2$	AF-II	a= 4.438, c=23.371 Å	a= 4.425, c=23.303 Å[a]	−13.8979	0
	AF-IIb	a=12.880 Å	-	−13.8796	0.0183
$TlSbSe_2$	AF-II	a= 4.178, c=22.408 Å	-	−14.9271	0
	AF-IIb	a=12.180 Å	-	−14.8773	0.0498
	MCN	a=9.227, b= 4.147, c=12.195 Å β=112.06	a= 9.137(1), b= 4.097(1), c=12.765(2) Å β=111.75(1)[b]	−14.8580	0.0691
$TlSbS_2$	AF-II	a= 4.013 Å, c=21.752 Å	-	−15.9962	0.0879
	AF-IIb	a=11.750 Å	-	−15.9189	0.1652
	TCN	a=6.236, b=6.273, c=11.879 Å α=101.70, β=96.94, γ=104.59	a=6.123(6), b=6.293(10), c=11.838(13) Å α=101.34(7), β=98.39(5), γ=103.21(19)[c]	−16.0841	0
$TlBiTe_2$	AF-II	a= 4.534, c=23.512 Å	a= 4.527, c=22.118 Å[d]	−14.4087	0
	AF-IIb	a=13.075 Å	-	−14.3998	0.0089
$TlBiSe_2$	AF-II	a= 4.264, c=22.478 Å	a= 4.24, c=22.33 Å[e]	−15.4537	0
	AF-IIb	a=12.360 Å	-	−15.4329	0.0208
$TlBiS_2$	AF-II	a= 4.096, c=22.845 Å	a= 4.153, c=10.914 Å (?)[f]	−16.4990	0
	AF-IIb	a=11.920 Å	-	−16.4617	0.0373

[a]Rhombohedral $R\bar{3}m$; Ref. [98].
[b]Monoclinic $P2_1$; Ref. [102].
[c]Triclinic $P\bar{1}$; Ref. [103].
[d]Rhombohedral $R\bar{3}m$; Ref. [98].
[e]Rhombohedral $R\bar{3}m$; Ref. [100].
[f]Rhombohedral $R\bar{3}m$; Ref. [101].

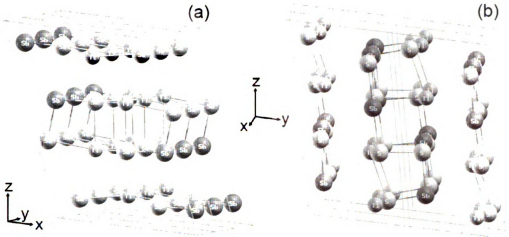

Figure 3.13: (a) Monoclinic (MCN) structure of $TlSbSe_2$ and (b) triclinic (TCN) structure of $TlSbS_2$. The coordinates are taken from experiments (see the text).

studies. AF-IIb [Fig. 3.1(c)] is also selected because of its closeness in energy with AF-II seen in many other ternaries. The possibility of having a transformation between AF-II and AF-IIb in these chalcogenides will be examined. The MCN and TCN structures for $TlSbSe_2$ and $TlSbS_2$ [see Fig. 3.13(a) and 3.13(b)], respectively, which are available in the literature are also analyzed. These two structures are layered structures; however, the local coordination of the atoms in these two structures are very different. In the monoclinic $TlSbSe_2$, which has (double) layers parallel to the (001) plane [Fig. 3.13(a)], Sb and Tl atoms have 5 bonds to Se atoms of 2.576-3.025 Å (for the Sb-Se) or 3.097-3.289 Å (for the Tl-Se) [102]. The shortest distance between the two double layers is 3.625 Å between Tl atoms from one double layer to the Tl atoms in the other. In the triclinic $TlSbS_2$ with layers parallel to the (010) plane [Fig. 3.13(b)], the Sb atoms have 4 bonds to S atoms of 2.41-2.96 Å [103]. The shortest distance between the layers in the TCN structure is ~3.50 Å. In my calculations, the structures are fully relaxed (volume, cell shape and positions of ions) and the results are summarized in Table 3.4 together with the experimental lattice parameters for comparison. The lattice parameters of the rhombohedral primitive cells are given in the hexagonal cell representation. The results for AF-II are in excellent agreement with experiments (within ~1-3% due to the overestimation of DFT-GGA) [21]. MCN

and TCN slightly change their lattice parameters after structural optimization due the rearrangement of the ions in these systems although their bond lengths do not change much (the deviation from those of experiments is less than 1%).

The rhombohedral AF-II is found to be the lowest energy structure in all the compounds, except in $TlSbS_2$ where the lowest one is the triclinic TCN. This is consistent with experiments where the Tl-based ternary chalcogenides (except $TlSbS_2$) have been found to possess a rhombohedral structure. The monoclinic MCN (as seen in the experiments) is not the lowest energy structure of $TlSbSe_2$. It is higher in energy than AF-II by ~70 meV, and even higher than the fcc AF-IIb (by ~20 meV). One, therefore, should reanalyze $TlSbSe_2$ samples to see if the rhombohedral AF-II could give a better fit to the X-ray diffraction data. In $TlSbS_2$, TCN has much lower energy than AF-II and AF-IIb (by ~ 88 and 165 meV, respectively) which suggests that the triclinic TCN is very stable energetically. In $TlBiTe_2$, on the other hand, AF-II and AF-IIb are very close in energy (~9 meV different). Experimentally it was observed that the phase transformation of $TlBiTe_2$ was a multiple-step displacive-martensitic type transformation [99]. Combined with our energetic studies, one may expect to see the system, if annealed from a cubic NaCl-type, pass through the fcc AF-IIb before going to the rhombohedral AF-II lattice. A mechanism for this transformation from AF-IIb to AF-II is probably via vacancies and/or interstitials. To summarize the structural aspects of the Tl-based ternary chalcogenides, the rhombohedral AF-II (for $TlSbTe_2$ and $TlBiQ_2$) and the triclinic TCN (for $TlSbS_2$) are found to be the lowest energy structures, consistent with experiments. The lowest energy structure for $TlSbSe_2$ is, however, AF-II, not the experimental MCN.

3.4.2 Electronic Structure

Figs. 3.14(a) and 3.14(b) show the total DOS of $TlSbTe_2$ and $TlSbSe_2$ in different ordered structures. There is very little difference between AF-II and AF-IIb in the

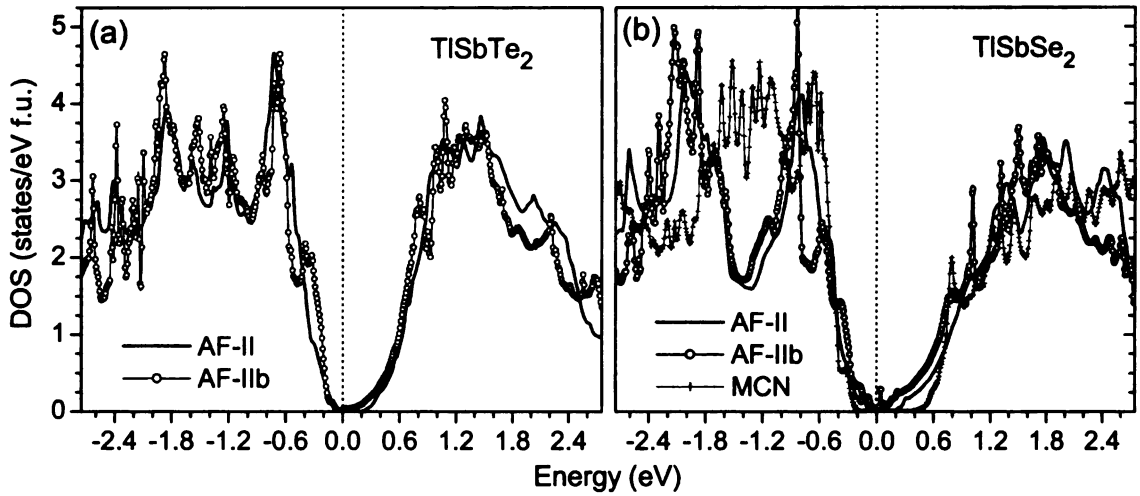

Figure 3.14: DOS of $TlSbQ_2$ (Q=Te, Se) in AF-II, AF-IIb, and MCN structures. The DOS of $TlSbSe_2$ in AF-II and MCN are shifted by ~0.080 eV and 0.166 eV, respectively, so that the bottom of the valence bands matched. The Fermi level (ϵ_F) is set at the highest occupied states (for AF-IIb in the case of $TlSbSe_2$).

DOS of $TlSbTe_2$ near ϵ_F, except for small transfer of the electronic states ranging from ~ -0.4 eV to -0.2 eV to lower energies in going from AF-IIb to AF-II. This results in lowering the energy of AF-II (by ~18 meV; see Table 3.4). From the DOS, we find that the fcc AF-IIb gives $TlSbTe_2$ a pseudo gap (with DOS~0 at ϵ_F), whereas the rhombohedral AF-II gives a band gap of ~0.2 eV. As regards $TlSbSe_2$, the monoclinic (MCN) structure gives the largest band gap of ~0.5 eV compared to ~0.1 eV (for AF-II) and ~0 eV (for AF-IIb). However, as we saw, MCN is not the structure that gives $TlSbSe_2$ the lowest energy (see Table 3.4). This can be explained in terms of the obtained DOS [Fig. 3.14(b)]. Although there is transfer of the electronic states near the valence band top DOS (ranging from -0.4 eV to 0 eV) to lower energies in going from AF-II and AF-IIb to MCN, there is much larger transfer of states from lower to higher energies in the region ranging from ~ -2.5 eV to -0.4 eV. This results in a higher energy for the MCN structure. It is also noted that there are significant differences in the electronic structure in the layered MCN structure compared to that in AF-II and AF-IIb structures.

For $TlSbS_2$, the higher energy AF-II structure gives a band gap of ~0.1 eV,

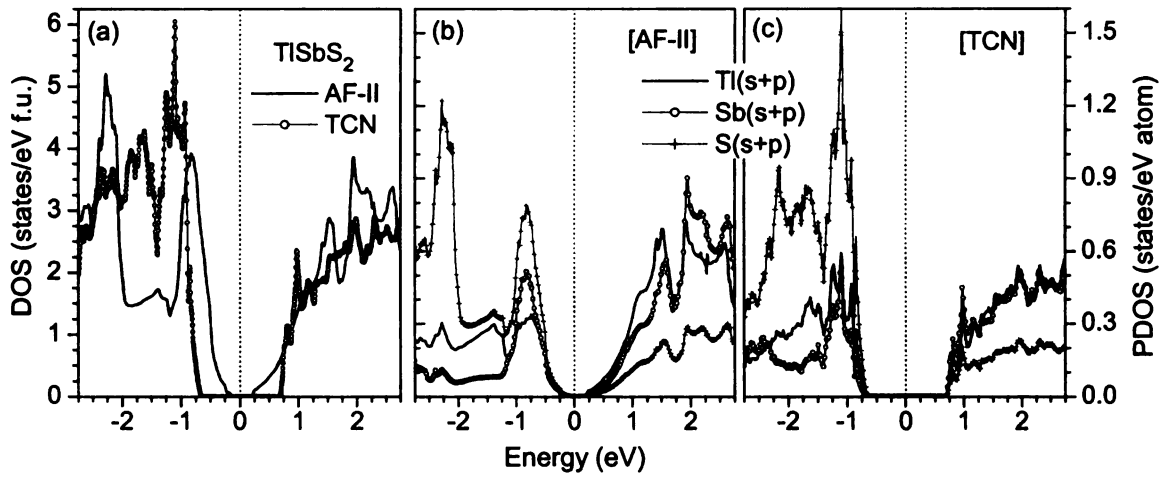

Figure 3.15: DOS and PDOS of $TlSbS_2$ in AF-II, AF-IIb, and TCN structures. The DOS and PDOS in TCN are shifted by ~0.644 eV so that the bottom of the valence bands matched. The Fermi level (ϵ_F) is set at the highest occupied states for AF-II.

whereas the lower energy experimental TCN gives a much larger band gap (~1.3 eV); see the DOS in Fig. 3.15(a). The latter value is comparable with the reported experimental values of 1.42-1.69 eV (at 300 K) [100]. In order to see the nature of the electronic states in the band gap region, the partial DOS (PDOS) associated with the s and p orbitals of Tl, Sb, and S for both AF-II and TCN structures are plotted in Figs. 3.15(b) and 3.15(c), respectively. PDOS analysis shows that the valence-band top is predominantly S p whereas the conduction-band bottom is predominantly Tl p and Sb p [Figs. 3.15(b) and 3.15(c)]. This suggests that Tl behaves like Tl^+ (monovalent) in these compounds. It is also a distinct feature that the p states of the monovalent atom play a role in band gap formation in the Tl-based III-V-VI_2 ternary chalcogenides in contrast to I-V-VI_2 systems where s-state played an important role.

Now I will discuss how the band structures change as one keeps the cations fixed and change the divalent anion, keeping the atomic structure fixed. One expects the degree of splitting between the valence and the conduction bands to increase as one goes from Te → Se → S. The band structures of $TlSbQ_2$ (Q=Te,Se, S) obtained in calculations with and without SOI are shown in Figs. 3.16(a)-3.16(d). These calculations made use of the rhombohedral AF-II structure, although AF-II is not the

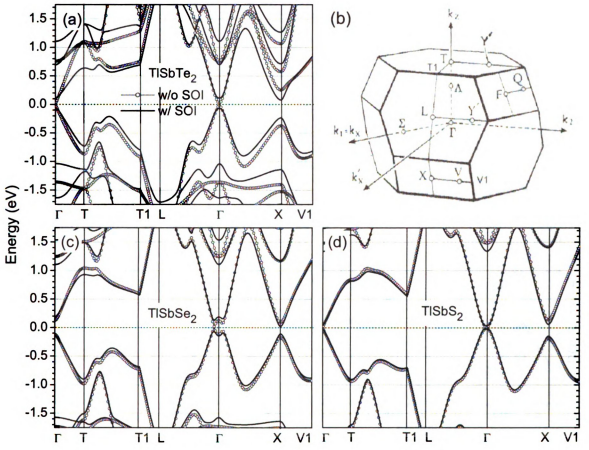

Figure 3.16: Band structure of $TlSbQ_2$(Q= Te, Se, S) along the high symmetry directions of the Brillouin zone of the rhombohedral AF-II structure. The Fermi level (ϵ_F) is set at the highest occupied states.

lowest energy structure of $TlSbS_2$. As seen in the figures, SOI has pronounced effects in the telluride. The band gap of $TlSbTe_2$ (~0.2 eV, a direct gap at the Γ point of the rhombohedral BZ) is a spin-orbit-induced gap. In the selenide, there is spin-orbit-induced gap near the Γ point and along the Γ-L direction of the rhombohedral BZ. This gap and a similar one near Γ and along the Γ-X direction [see Fig. 3.16(c)], which are hybridization induced gaps, create a multi-peak structure near the top of the valence band and near the bottom of the conduction band. However, the smallest gap of $TlSbSe_2$ in the AF-II structure is an indirect gap (of ~0.1 eV) between the maximum along the Γ-L direction and the minimum at the X point. The SOI has very small effect on the band structure near ϵ_F of $TlSbS_2$ as one would expect.

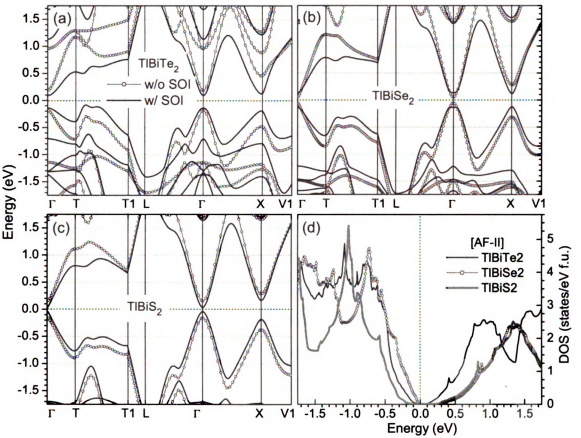

Figure 3.17: DOS and band structure of TlBiQ_2(Q= Te, Se, S) along the high symmetry directions of the Brillouin zone of the rhombohedral AF-II structure. The Fermi level (ϵ_F) is set at the highest occupied states.

The valence-band top and conduction-band bottom of the band structures of TlSbQ_2 compounds are quite symmetric through the Fermi level, except along the T-T1 direction where there is a band asymmetry and the maxima in the valence band is closer to ϵ_F than the minima in the conduction band. In the case of $TlSbTe_2$, the peak (at ~ -0.2 eV) along the T-T1 direction [see Fig. 3.16(a)] can contribute to the transport which results in a large positive thermopower ($\sim$220 μV/K at 630 K; as seen in experiments [78]).

SOI effects should be much stronger in TlBiQ_2 compounds since Bi is heavier than Sb. This can be seen in Figs. 3.17(a)-(c) where the band structures of TlBiQ_2 obtained in calculations with and without SOI in the rhombohedral AF-II structure

are splotted. SOI dramatically changes the band structure of $TlBiQ_2$, especially for Q=Te where all the three elements Tl, Bi, and Te are heavy. From the DOS [Fig. 3.17(d)], $TlBiQ_2$ is found to have a band gap of $\sim$0 eV (for Q=Te), 0.25 eV (Q=Se; at the X point), or 0.07 eV (Q=S; at the Γ point). The band structure of $TlBiTe_2$ shown in Fig. 3.17(a) does not scan all the possible extrema in the whole BZ. Experimentally, it is reported that $TlBiS_2$ and $TlBiSe_2$ have band gap of 0.4 eV and 0.28 eV, respectively [100]; whereas $TlBiTe_2$ has a band gap of 0.11 eV [104]. Among the three compounds, only the calculated band gap of $TlBiSe_2$ is in good agreement with experiments. It is noted that the physics of gap formation in these Tl-based III-V-VI_2 ternary chalcogenides is much more complicated than that of the I-V-VI_2 systems because of the strong spin-orbit effects, hybridization, and the participation of the Tl p bands. This can make the "band gap problem" [23] in these systems even worse.

There is also band asymmetry between the valence-band top and the conduction-band bottom along the T-T1 direction in these Tl-Bi-based compounds, similar to the Tl-Sb-based ones. It is reported that n-type $TlBiTe_2$ has ZT=0.15 at 760 K [77], much smaller than p-type $TlSbTe_2$ which gives ZT=0.87 at 715 K [78]. The smaller ZT value is due to the small (and negative) thermopower in $TlBiTe_2$ ($\sim -70\ \mu$V/K on average) [77]. Based on the calculated band structure, I would suggest that $TlBiTe_2$ should be made p-type to take advantage of the band asymmetry, especially the flat band feature near the T point and along the T-T1 direction [as shown in Fig. 3.17(a)]. This goal, however, may not be trivial in practice since it has been reported that $TlBiTe_2$ consistently shows n-type conductivity [75, 77, 105] whereas $TlSbTe_2$ shows p-type [78]. The reason for this may come from defect complexes and/or secondary phases which are present in the samples but are different in different compounds. Preliminary results for the formation energies of possible vacancies (point defects) in $TlBiTe_2$ and $TlSbTe_2$ do not show any significant difference between the two com-

pounds that can explain why one is n-type and the other is p-type.[4] More theoretical and experimental studies are needed to understand this matter, and also to learn how to control the conductivity of the systems.

3.5 Summary

In summary, I have carried out a detailed investigation of the structural orderings on the cation sublattice of I-V-VII_2 and Tl-based III-V-VII_2 ternary chalcogenides (I=Na, K, Ag, Cu; V=As, Sb, Bi; VII=S, Se, Te) and how they impact on the electronic properties. Total energy calculations identify the rhombohedral AF-II structure as one of the lowest energy structures of $AgSbTe_2$, which is consistent with the observed atomic structure [17]. It is also the lowest energy structure in most of the $TlSbQ_2$ and $TlBiQ_2$ compounds, except for $TlSbS_2$ where theoretical calculations give the triclinic structure (in agreement with experiment). There is, however, disagreement between theory and experiment in the case of $TlSbSe_2$ where experiment gives a monoclinic structure whereas our calculations identify the rhombohedral AF-II as the lowest energy structure. In view of this, I suggest experimentally reexamining the structure.

The highly directional hybridization between the cation (As, Sb, Bi) p states and the anion (S, Se, Te) p states is found to play an important role in the band gap formation of the ternary chalcogenides. This hybridization tends to drive the systems towards (semi)metallicity, which is also consistent with the observation in Chapter 2 where the electronic structures of several $AgPb_mSbTe_{m+2}$ (LAST-m) compounds

[4]Formation energies of Tl, Bi, and Te vacancies in $TlBiTe_2$ are 0.972, 2.096, and 1.632 eV/vacancy, respectively, whereas in $TlSbTe_2$ they are 0.781 (Tl), 1.404 (Sb), and 1.506 (Te) eV/vacancy. These values were calculated using Eq. (3.2) with the chemical potential of the removed atom was calculated as the energy per atom in its standard metallic state. The total energies were obtained in calculations using 64-site AF-II supercell; SOI was not included. It is possible that the elements that form $TlSbTe_2$ (or $TlBiTe_2$) do not come as metals in their standard metallic state, but as, for example, Tl_2Te and Sb_2Te_3 (or Tl_2Te and Sb_2Te_3). One, therefore, should recalculate the chemical potential term in Eq. (3.2) accordingly. Also, SOI should be included.

are discussed. The ordering on the cation sublattice, therefore, has a huge impact on the electronic structure of I-V-VII_2 and Tl-based III-V-VII_2 in the neighborhood of the Fermi energy. In $AgSbQ_2$ compounds, for example, it gives pseudogap structure in some ordered structures (AF-I and AF-III), and either pseudogap (Q=Te) or gap (Q=Se, S) structure in others (AF-II and AF-IIb). The (indirect) band gap of $AgSbQ_2$ (in the AF-IIb structure) goes from negative to positive values in going from Te $\rightarrow$ Se $\rightarrow$ S. The anomalous electronic properties of $AgSbTe_2$ can, however, be understood in terms of a small intrinsic band gap and shallow impurity states.

Besides the p states of the trivalent cations (As, Sb, Bi) and divalent anions (S, Se, Te), s state (in the case of Na and K) or s and d states (in the case of Ag, Cu, and Au) also play an important role in the band gap formation. These states impact the electronic structure near the band gap region through strong hybridization with the p states of the trivalent cations and divalent anions. The s state affects the electronic structure near the conduction-band bottom, whereas the d states affect the electronic structure near the valence-band top. The physics of gap formation is more complicated in the Tl-based III-V-VI_2 ternary chalcogenides because of the strong spin-orbit effects, hybridization, and the participation of the directional and degenerate Tl p bands.

The studies presented in this chapter suggest how to modify a certain ternary by replacing its constituting element(s) such that the electronic structure shows desired features for different applications. The results obtained in *ab initio* electronic structure calculations can provide experimentalists with some guidance as they search for systems with desired properties and also to look at some of the promising systems more carefully. Some systems have been identified as potential p-type thermoelectric materials, as far as the band structure is concerned, such as $NaSbTe_2$, $KSbTe_2$, $CuSbTe_2$, $AgAsTe_2$, $AgAsSe_2$, $AgBiTe_2$, $TlSbTe_2$, and $TlBiTe_2$.

Chapter 4

Defects in Narrow Band-Gap Semiconductors

The nature of defect-induced electronic states in PbTe is studied using density functional theory and supercell models. I discuss how the defect states associated with different substitutional impurities and native point defects found in bulk PbTe are modified in the film and cluster geometries. I also look at the energetics of the defects and discuss their implications in doping mechanism and the distribution of the defects in bulk PbTe with grain boundaries and in PbTe nanostructures.

4.1 Introduction

Lead chalcogenides (PbTe, PbSe, and PbS) are IV-VI narrow band-gap semiconductors whose studies over several decades have been motivated by their importance in infrared (IR) detectors and lasers, light-emitting devices, photovoltaics, and high temperature thermoelectrics [106, 107, 108, 109, 5]. PbTe in particular is the end-compound of several ternary and quaternary high performance high temperature thermoelectric materials [15, 18, 19, 110, 111, 112, 113]. It has been used not only as bulk but also as films [114, 115, 116, 117], quantum wells [118], superlattices [119, 120],

nanowires [121], and colloidal and embedded nanocrystals [122, 123, 124, 125]. PbTe films doped with group III (Ga, In, Tl) impurities have been studied recently [126, 127, 128, 129, 130, 131, 132, 133]. These studies have revealed some of the interesting features that had been seen in bulk PbTe, such as Fermi level pinning and, in the case of Tl, superconductivity [134].

As it has been discussed in the introduction, the transport and optical properties of semiconductors are dominated by the electronic states in the neighborhood of the band gap. Thus it is important to understand the nature of these states and how they change in the presence of defects. In PbTe, which has very large dielectric constant and small effective masses,[1] one usually has "deep" defect states (rather than the "shallow" ones which are described by a hydrogenic model) dominated by the short-range atomic-like defect potential and changes in the local bonding.[2] The problem of defect states in PbTe has been theoretically studied by numerous authors using different methods: from a simple chemical theory [135], a Slater-Koster model [136], $X\alpha$ scattered-wave (XSW)-cluster method [138], an ionic lattice approach [139], Green's function method [140], to *ab initio* electronic structure calculations [141, 41, 142, 143, 144, 145]. *Ab initio* calculations carried out recently for a large class of substitutional impurities and vacancies on the Pb and Te sites showed that the single-particle density of states (DOS) near the top of the valence band and the bottom of the conduction band get significantly modified for most of the defects [144]. Although PbTe films doped with group III impurities have been experimentally studied [126, 127, 128, 129, 130, 131, 132, 133], to the best of my knowledge, there are no theoretical studies on the nature of the defect states in PbTe thin films and nanoclusters. A natural question then arises: how do these states change as one

[1] In PbTe, the dielectric constant ϵ ~30-400 and the effective masses m ~0.02-0.31m_0 (Ref. [100]).

[2] We define "deep" and "shallow" defect states not in terms of their relative positions to the band edges but by the localization of the wave functions. For a recent discussion of shallow versus deep defects and the role of defects in semiconductors, see, for example, H. J. Queisser and E. E. Haller, Science **281**, 945 (1998).

goes from bulk to film to nanocluster geometry? In addition, the surfaces (in the thin films and in the nanoclusters) are themselves extended defects, which can also help manipulate the electronic states near the band gap region.

Another fundamental issue is the energetics of defects. Although doping is fundamental to controlling the properties of bulk semiconductors and semiconductor nanostructures, efforts to dope semiconductor nanocrystals, despite some successes, have failed in many cases (see Ref. [146] and references therein). The reason for this is usually ascribed to the so-called "self-purification", an intrinsic mechanism whereby impurities are expelled. Using kinetic arguments, Erwin *et al.* [146] argued that the underlying mechanism that controlled doping was the initial adsorption of impurities on the nanocrystal surface during growth, i.e., they suggested that impurities were incorporated into a nanocrystal if they could bind to its surface for a residence time comparable to the reciprocal growth rate. The adsorption was in turn determined by surface morphology, nanocrystal shape, and surfactants in the growth solution [146]. Dalpian and Chelikowsky [147] have recently argued that the "self-purification" mechanism can be explained through energetic arguments. They found that the formation energy of defects in CdSe nanocrystals increased as the size of the nanocrystals decreased, thereby explaining why it is difficult to dope nanocrystals. This also sheds some light about the expulsion of dopants from small clusters. They, however, did not study the dependence of the formation energy on the position of the defects which can be very important in large nanocrystals with well-defined surfaces. Energetic studies of defects in thin films (with well characterized surface) will help in addressing this issue. Moreover it is necessary to know how stable the defects are in the surface and subsurface layers and what are their preferential sites. This will help us understand the doping mechanisms and the distribution of these defects in PbTe films, and is a first step to understand defect distribution at the grain boundaries in sintered PbTe [148], and near the interfaces in nanoscale structures embedded PbTe-

based bulk materials [15, 18, 19, 110, 111]. It is also interesting to see if there is "self-purification" in PbTe nanoclusters.

Although surface relaxation and electronic structure of undoped PbTe(001) films have been studied by Satta and de Gironcoli *et al.* [149] and, recently, by Ma *et al.* [150] using DFT, in this chapter I revisit the films in more detail and with larger supercells to confirm and supplement the results of the earlier theoretical works. A large part of this chapter, however, concerns with point defects in PbTe films and nanoclusters, which have not been studied previously. The nature of the defect states associated with different impurities and native point defects is studied using supercell models. The impurities discussed here include group III elements which have been studied extensively in bulk PbTe in relation to the deep defect states [134], various monovalent (Ag, Na, K), divalent (Zn, Cd), and other trivalent (Sb, Bi) impurities. All these impurities have significance in thermoelectric applications. As regards the native defects, we study Pb and Te vacancies. Other native point defects such as self-interstitials and antisite defects might be important but will not be considered here. The effects of atomic relaxation and spin-orbit interaction (SOI) will be discussed. We also calculate the formation energy associated with different defects in various geometries and discuss the possible implications on the ability to dope PbTe films with these defects and their distribution in films and also in bulk materials.

The arrangement of this chapter is as follows. In Sec. 4.2, I describe the supercell model and discuss briefly the method used to perform structural optimization and electronic structure calculations. In Sec. 4.3, I present results for pure PbTe(001) films. The nature of defect states in bulk PbTe and PbTe(001) films is presented in Sec. 4.4 where the available experimental data are discussed in the light of theoretical results. Studies of undoped and doped PbTe nanoclusters are presented in Sec. 4.5. Finally, I give a brief summary of results in Sec. 4.6. A major part of this chapter has been published in *Physical Review B* [151] and *Physica B* [152].

4.2 Modeling of Defects

4.2.1 Supercell Models

The (001) surface is the typical cleavage face in PbTe. In PbTe(001) films, each layer parallel to the film surface has an equal number of anions and cations. The pure PbTe (001) film and the film with point defects were modeled in the supercell geometry by respectively (1 × 1) and (2 × 2) slabs[3] of N atomic layers (N=7-15) alternately separated by M equivalent vacuum layers (M=5, thickness of ~20 Å). In the (1 × 1) slab, each layer contains 4 atoms; whereas in the (2 × 2) slab, there are 16. The central 3 layers of the slabs were held at their bulk configuration to mimic the bulk structure while the remaining $(N-3)/2$ layers on each side of the slab were allowed to relax laterally and vertically without any symmetry constraint. The first (surface) layers of the top and the bottom sides of the slab were taken to be identical which makes the undoped film centrosymmetric [153]. I will refer to a surface supercell as (1 × 1) or (2 × 2) when the system contains N-layer (1 × 1) or (2 × 2) slabs separated by M equivalent vacuum layers.

The impurities in PbTe thin films were studied using the 9-layer (2×2) slabs. A single Pb atom in the first (surface) layer on the top side of the slab is replaced by an impurity atom R. To place the corresponding atom in the bottom layer, one can use either the reflection symmetry about the central layer or inversion symmetry about the slab center. If the impurities are far apart, it should not matter. In the present calculations, I have preserved the reflection symmetry. The supercell has the composition $R_2\mathrm{Pb}_{n-2}\mathrm{Te}_n$ (n=72). To study the site preference of the impurities, the impurity atoms were also placed in a similar way at the Pb sites either in the second or in the third layer. This gives three geometric configurations in total for our current studies of defects in PbTe films. The two impurity atoms (one on each side) are

[3]The numerics being used to name the slab here are in terms of the lattice constant of bulk PbTe; not in terms the number of anions and cations in each atomic layer like in some earlier works.

equivalent in this model. Because of the lateral periodicity, there is a periodic array of impurity atoms in each layer, the minimum distance between the two impurities being ~13 Å. This is the typical distance which has been used for the study of defects in the corresponding bulk system [143, 144]. The vacancies in PbTe(001) films were created in the same manner by removing a single Pb or Te atom in the corresponding atomic layer (on each side of the slab).

Two bulk supercells of sizes $(1\times1\times1)$ [8 atoms/cell] and $(2\times2\times2)$ [64 atoms/cell] were also used as reference systems for the (1×1) and (2×2) surface supercells, respectively. The defects and impurities in the bulk were studied using the $(2\times2\times2)$ or larger, $(3 \times 3 \times 3)$ [216 atoms/cell], supercells. The impurity-impurity distance in the (2×2×2) supercell is ~13 Å, whereas that in the (3×3×3) is ~20 Å.

4.2.2 Computational Details

Structural optimization, total energy and electronic structure calculations were performed within the density functional theory (DFT) formalism, using the generalized-gradient approximation (GGA) [55] and the projector-augmented wave (PAW) [56] method as implemented in VASP [57]. The outermost s and p electrons of Pb and Te were treated as valence electrons and the rest as cores; scalar relativistic effects and a dipole correction [154] along the z direction [normal to the (001) surface] were included. Spin-orbit interaction (SOI) was not included in all the calculations (see discussions in Sec. 4.3 and 4.4). The energy cutoff was set up to 300 eV, and the convergence was assumed when the total energy difference between consecutive cycles was within 10^{-4} eV. Structural optimization was carried out without SOI since it is found that the inclusion of SOI did not have significant influence on the structural properties [58]. All the atomic coordinates (except for those in the central 3 layers of the slabs, unless otherwise noted) were relaxed using the conjugate-gradient algorithm [155] with a tolerance factor of 10^{-3} eV/Å for the force minimization.

For the (1×1) surface supercells, $7 \times 7 \times 1$ and $9 \times 9 \times 1$ Monkhorst-Pack [156] **k**-point meshes were used, respectively, for the structural optimization and for total energy and charge density calculations; whereas for the (2×2) surface supercells, they are $3 \times 3 \times 1$ and $5 \times 5 \times 1$. For the bulk supercells, similar **k**-point meshes were used but the number of subdivisions along the third reciprocal lattice vector were equal to those of the first two. Larger **k**-point meshes were used in non-selfconsistent calculations using charge density from the previous selfconsistent runs to obtain high quality single-particle density of states (DOS). The DOS was calculated using the tetrahedron method with Blöchl corrections [157] and then smoothed using a 3-point Fast Fourier Transform (FFT) filter. The optimized bulk lattice constant a=6.55 Å was used to set up initial structures in all the calculations- with and without defects (see the discussion on the use of the optimized bulk lattice constant in Sec. 4.3.1).

It is known that there are fundamental issues with the use of supercell method in studying defects in semiconductors because of the finite size and the artificial periodicity of the supercells [158, 159]. I, however, expect that the method is adequate in the current studies since PbTe has a large dielectric constant which can help screen the long-range Coulomb interaction. Moreover, most of the defect states in PbTe are of localized "deep" type, not the extended "shallow" one, which makes supercell method a reasonable choice.

4.3 Pure PbTe Thin Films

Structure analysis of PbTe(001) surface performed by Lazarides *et al.* [160] using low-energy electron diffraction showed that there was a damped oscillatory relaxation normal to the surface and a large (~7%) rumpling of the surface with the top-layer Pb atoms sinking below the plane containing the anions. Theoretical calculations within the framework of DFT carried out by Satta and de Gironcoli [149] and later by Ma *et al.* [150] showed a qualitative consistency with the experiment. Ma *et al.* also studied

the electronic properties of the PbTe(001) and claimed that the electronic structure of the PbTe(001) was similar to that of PbS(001) and there were bound surface and surface resonance states in the system. However, they did not provide explicitly their results for the PbTe(001). SOI was also not included in their calculations. In this section we revisit the PbTe(001) surface in more detail and with larger supercells [151].

4.3.1 Geometric Relaxation

Since Pb-Te bonds have strong ionic character one expects to see effect of the long-range Coulomb interaction on the geometric relaxation of PbTe(001) films in spite of screening effects. In Fig. 4.1(a), I show the optimized geometry of a 11-layer (1 × 1) centrosymmetric slab with two equivalent (001) surfaces (one on the top and the other

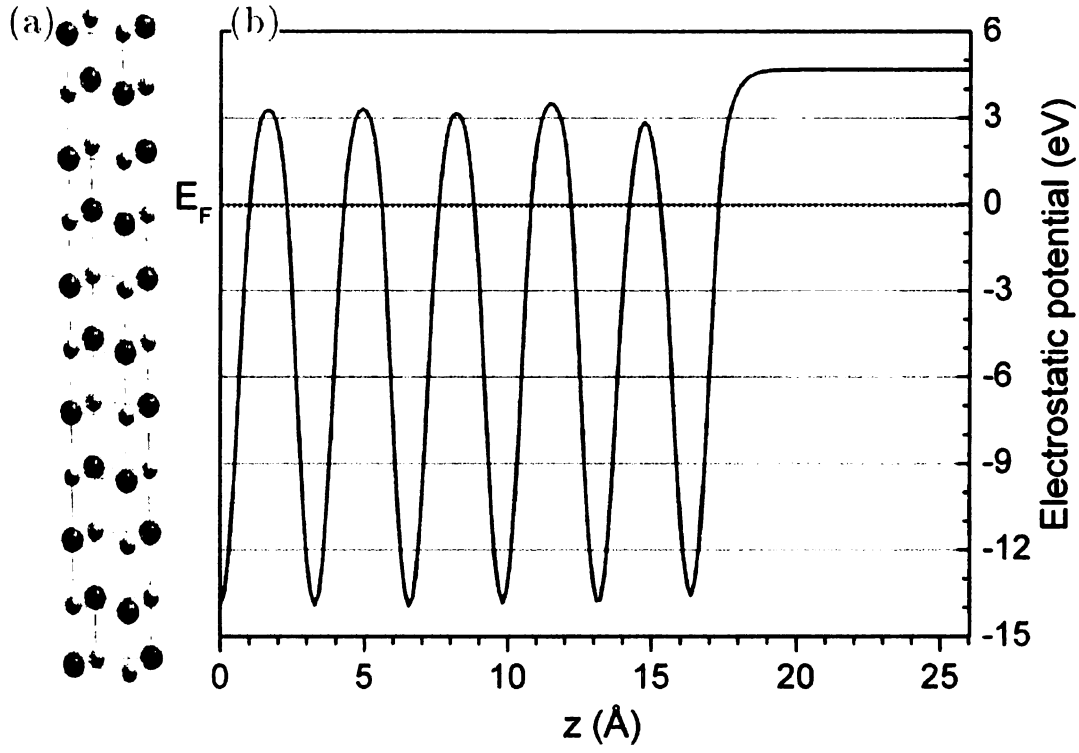

Figure 4.1: (a) Optimized geometry of the PbTe(001) film [11-layer (1 × 1) slab], and (b) planar-averaged electrostatic potential of the optimized film (the potential of half of the slab is shown with the origin in the central atomic layer). Large balls are Pb atoms, small balls are Te.

Table 4.1: The change in the interlayer distance for the Pb(Te)-sublattice ($\delta_{ij}^{\mathrm{Pb(Te)}}$), their average values [$\widehat{\delta}_{ij}$=($\delta_{ij}^{\mathrm{Pb}}$ + $\delta_{ij}^{\mathrm{Te}}$)/2], and the intralayer rumpling (ζ_i) of the relaxed PbTe(001) surface. The results of earlier studies are also given.

N	Average (%)					Rumpling (%)				
	$\widehat{\delta}_{12}$	$\widehat{\delta}_{23}$	$\widehat{\delta}_{34}$	$\widehat{\delta}_{45}$	$\widehat{\delta}_{56}$	ζ_1	ζ_2	ζ_3	ζ_4	ζ_5
7	−4.65	2.75				−5.67	3.44			
9	−4.84	3.59	−0.99			−6.71	4.70	−2.04		
11	−4.89	3.42	−1.17	0.78		−6.90	5.03	−2.88	1.30	
15	−4.99	3.68	−1.34	0.92	−0.22	−6.50	4.62	−2.95	−0.82	0.66
7[a]	−4.1	2.1	−0.1			−5.3	−1.4			
9[b]	−4.3	1.82	−0.29	0.70		−3.18	1.70	−0.01	0.11	
Expt.[c]	−4	2				−7				

[a]Ref. [149]
[b]Ref. [150]
[c]Ref. [160]

at the bottom) where 8 out of 11 layers are allowed to relax. The surface exhibits a damped oscillatory relaxation along the z (vertical) direction starting with contraction. There is also the rumpling in each (sub)surface layer. No lateral relaxation is found in these calculations, even when larger supercells are used [up to 16 atoms per atomic layer in the (2×2) slab]. Anions (cations) in a particular atomic layer relax as a whole along the z direction but their x and y coordinates do not change. This is known in nonpolar (001) surface of rocksalt structure [153].

In order to quantify the vertical relaxation of the PbTe film, one defines two parameters. One, δ_{ij}^{X}, to describe the change in the interlayer distance on the X-sublattice (X=Pb or Te) measured by taking the distance between the vertical positions of its ith and jth layers (with the coordinate origin in the central atomic layer), scaled to the bulk interlayer distance d_0:

$$\delta_{ij}^{\mathrm{X}} = \frac{(z_i^{\mathrm{X}} - z_j^{\mathrm{X}}) - d_0}{d_0}, \tag{4.1}$$

where z_i^X is the position of X atoms along the z direction in a given layer i; d_0=3.275

Å. The second parameter, ζ_i, describes the rumpling in a given layer i, and is defined as

$$\zeta_i = \frac{(z_i^{\mathrm{Pb}} - z_i^{\mathrm{Te}})}{d_0}. \tag{4.2}$$

The results for slabs of N=7, 9, 11, and 15 are summarized in Table 4.1. As seen from the values of δ_{ij}^{X}, there is contraction (expansion) in the Pb (Te) sublattice. Since the contraction is much larger than the expansion, there is still a net contraction of the average position of the atomic (Pb-Te) layers. This behavior persists even when all the layers of the 11-layer slab are allowed to relax in an independent calculation. This is surprising, since it is thought that for the (001) rocksalt surface both sublattices should relax inward [153]. The diffuse nature of Te p orbitals might be responsible for the observed expansion of the Te-sublattice. This opposite relaxation of the anions and cations (in addition to the difference in their core radii) causes a large surface rumpling seen in experiments [160]. As pointed out by Satta and de Gironcoli [149] the relaxed geometry near the surface can be understood in terms of the competition between the long-range electrostatic interaction and the short-range Pauli repulsion between the ionic cores. The oscillatory layer relaxation can be traced back to the electrostatic part of the cohesive energy, whereas the rumpling is due to the asymmetric relaxation present in PbTe (but absent in PbS and PbSe) [149].

The present results for the change in the average interlayer distance ($\widehat{\delta}_{ij}$) and the intralayer rumpling (ζ_i) [see Table 4.1] are qualitatively consistent with earlier works [149, 150] and in agreement with experiments [160]. Especially, the rumpling in the first atomic layer in our calculations for $N = 9$ (-6.71%) is about a factor of 2 larger than that obtained by Ma *et al.* [150] (-3.18%) and is much closer to the experimental value ($\sim -7\%$). The reason for this discrepancy might be related to the relaxation methods used; it is neither because of the different lattice constants used (a=6.45 Å in the work by Ma *et al.*, whereas 6.55 Å in the present work) nor the different GGA versions (PW91 [161] in Ma *et al.*, PBE [55] in the present work)

since the calculations with a=6.45 Å using PW91 and PBE versions give, respectively, $\zeta_1 = -7.48\%$ and -7.83%, also ~ 2 times larger than that from Ma *et al.* (in these particular calculations all the 9 layers were allowed to relax, like Ma *et al.* did).

It is noted that the optimized lattice constant of bulk PbTe obtained in GGA calculations (a=6.55 Å) is ~1% larger than that of experiment (6.462 Å at 300 K) [100]. This is not unexpected since it is well known that GGA tends to overestimate the lattice parameters (and therefore the volume); local-density approximation (LDA) [162], on the other hand, underestimates them (our calculations give a=6.38 Å) [163]. The surface relaxation of PbTe(001) films is, however, not greatly affected by the choice of GGA or LDA. In the 11-layer (1×1) slab, for example, LDA calculations give $\widehat{\delta}_{12}$=−4.51%, $\widehat{\delta}_{23}$=2.26% and ζ_1=−6.29%, also comparable with experiment (see Table 4.1). GGA and LDA calculations using experimental lattice constant (6.462 Å), on the other hand, do not show good consistency with experiment; $\widehat{\delta}_{12}$=−3.15%, $\widehat{\delta}_{23}$=4.87%, and ζ_1=−7.41% (in GGA), $\widehat{\delta}_{12}$=−5.93%, $\widehat{\delta}_{23}$=1.46%, and ζ_1=−5.67% (in LDA). This suggests that, whichever choice of the approximation (GGA or LDA) is made, it is important that the calculations should be carried out using the theoretical bulk lattice constant properly optimized in the chosen approximation. In defect calculations using supercell models, in general, it is advised that the calculations should be carried out using the theoretical bulk lattice constant in order to avoid the spurious elastic interactions with defects in the neighboring supercells [158].

4.3.2 Energetics

In Fig. 4.1(b), the planar-averaged electrostatic potential as a function of the z coordinate (normal to the surface) for the optimized 11-layer (1×1) slab is shown. The vacuum energy $\epsilon^{vac} \approx$4.7 eV above the Fermi level. The depth of the potential valleys increases in going from the surface to the central layer. This is due to the rumpling in the corresponding atomic layers. The potential barrier between the second and

the third atomic layers (where the Pb-sublattice expands most) is the highest and is 0.2-0.5 eV higher than the others. I have also calculated the surface energy and work function for the PbTe films, not done previously by the other authors. The surface energy (γ) is defined as

$$\gamma = \frac{1}{2}(E^{slab} - E^{bulk}), \tag{4.3}$$

where E^{slab} is the total energy of a supercell of N atomic layers and E^{bulk} is the total energy of a bulk supercell with equal number of atoms; γ will be scaled to have the units of eV per surface Pb-Te pair. The factor 1/2 appears because there are two surfaces. The work function $\Phi = \epsilon^{vac} - \epsilon_F$, where ϵ^{vac} and ϵ_F are the vacuum energy and the Fermi energy, respectively. ϵ_F was put at the top of the valence band. The calculations give γ=0.227, 0.223, 0.213, 0.209 (eV per surface Pb-Te pair) and Φ=4.662, 4.726, 4.695, 4.679 (eV) for N=7, 9, 11, 15, respectively. The calculated work function ~4.6-4.7 eV is in excellent agreement with the experimental value (4.5±0.3 eV) [164]. The surface energy and the work function converge well as one increases the number of layers. The evolution of γ and Φ as a function of N and the characteristics of the surface relaxation and rumpling of slabs with different thicknesses (Table 4.1) suggest that, in order to simulate the PbTe(001) film, slabs with 11 or 15 layers are reasonable. The dipole correction [154] along the z direction, which was intended to remove the artificial electrostatic interaction which arises due to the periodic boundary conditions, is found to have negligible contribution (less than 0.001 %) to the total energy. This is expected since the (001) surface is nonpolar.

4.3.3 Electronic Structure

The total DOS of the bulk and the 11-layer (1 × 1) slab are shown Fig. 4.2(a). One finds that there are surface states near the top of the Te 5s band [at ~ −10 eV; marked by an arrow in Fig. 4.2(a)]. The Pb 6s band (in the energy range −8.3 eV to −5.7 eV) has very little change in going from the bulk to the thin film. There

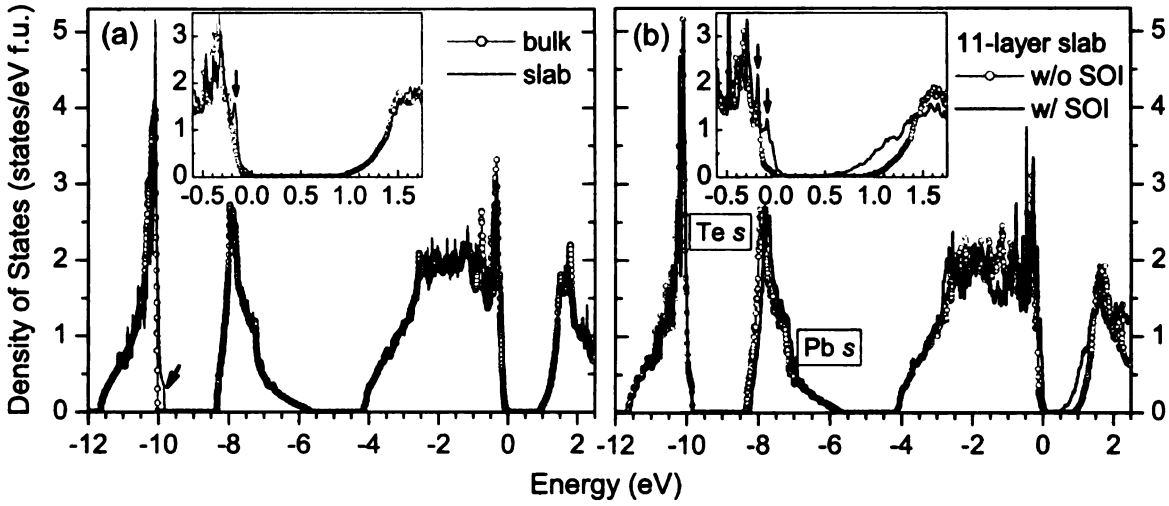

Figure 4.2: (a) DOS of the bulk and the 11-layer (1 × 1) slab of PbTe without SOI and (b) DOS of the slab with and without SOI; the insets showing the details of the DOS near the valence-band top. The DOS of the slab in (a) was shifted by a small amount (+0.012 eV) so that the lower edge of the Pb 6*s* band DOS of the bulk and the film matched; the DOS with SOI in (b) was shifted by +0.118 eV so that the valence-band bottom of the two matched. The zero of the energy is chosen at the highest occupied state for the bulk [in (a)] and for the slab without SOI [in (b)].

is an additional peak near the top of the valence band [one at ~ -0.18 eV, marked by the vertical arrow in the inset of Fig. 4.2(a)] that could be identified as a surface resonance state.

To look further into this, the local density of states (LDOS) was calculated in each atomic layer of the slab. The results are shown in Figs. 4.3(a)-4.3(d), where the LDOS of the first (surface) layer is plotted and the bulk-like sixth (central) layer is used as a reference. In Fig. 4.3(a), plots of the Pb 6*s* character of the two layers match well with each other. This is the reason why in Fig. 4.2(a) and in some of the following figures we shifted the total DOS of the film by a small amount so that the lower edge of the Pb *s* band DOS of the bulk and the film matched before making comparison between the rest of the DOS for the two systems. As shown in Fig. 4.3(c), the Te 5*s* state is pushed upward in energy and a surface state is created on the top of that band. The difference in the behaviors of the Pb 6*s* and Te 5*s* states in the first layer can be understood in terms of the relaxed geometry, where the Te atoms form the outermost surface layer (in the first atomic Pb-Te layer, Te atoms relax slightly

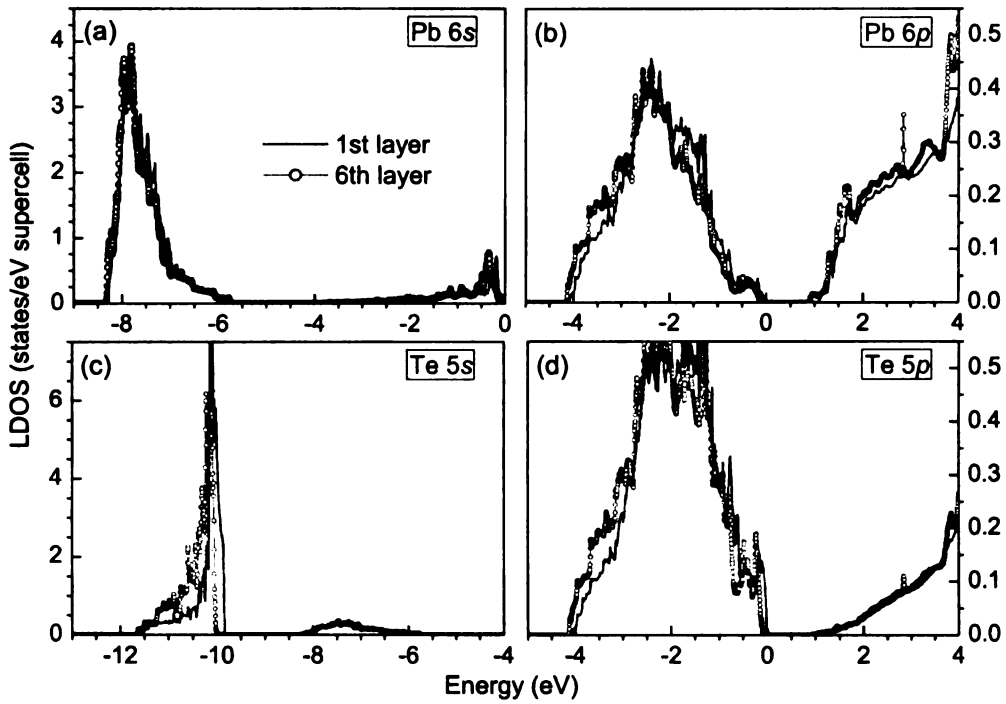

Figure 4.3: Local density of states (LDOS) of the 11-layer (1 × 1) PbTe slab in the first (surface) and the sixth (bulk-like) layers: (a) Pb 6*s*, (b) Pb 6*p*, (c) Te 5*s*, and (d) Te 5*p*. The zero of the energy is chosen at the highest occupied state.

outward, whereas Pb atoms relax inward). In Figs. 4.3(b) and 4.3(d), I show the Pb 6*p* and Te 5*p* characters in the first and the sixth layers. There are some indications for surface resonance states near the top (bottom) of the valence (conduction) band that had been already identified by Ma *et al.* [150]. In order to properly characterize these surface (resonance) states, one should carry out careful analysis based on projected band structure [153] (which we have not done independently). Because of the strong coupling between the *p* states on the surface and other states in the bulk, surface states do not appear in the fundamental gap.

4.3.4 Spin-Orbit Effects

In order to see the effects of spin-orbit interaction (SOI), I show in Fig. 4.2(b) DOS of the 11-layer (1×1) PbTe slab with and without SOI. The major effect of SOI is to reduce the band gap, similar to what had been seen in bulk PbTe (where our

calculations showed that the band gap is reduced from ~0.8 eV to ~0.1 eV). If one shifts the DOS with SOI by a small amount so that the bottom of the valence band of the two curves matches [see Fig. 4.2(b)] then the top of the valence band (predominantly Te $5p$) shifts upward in energy by ~0.1 eV and the bottom of the conduction band (predominantly Pb $6p$) shifts downward by ~0.5 eV. The Pb $6s$ band is also shifted upward by ~0.12 eV (In the crystal, it is not a pure s-state). There is no noticeable change due to SOI near the top of the Te $5s$ band DOS (where one has the surface state). There are now two major peaks (instead of one, originally at ~ -0.18 eV) near the top of the valence band due to the spin-orbit splitting, one at ~ -0.18 eV and the other at ~ -0.09 eV [with respect to the zero of energy in the DOS without SOI; marked by arrows in the inset of Fig. 4.2(b)].

Besides the difficulty with the lattice parameters, DFT is also known to usually underestimate the band gaps of semiconductors [23]. In bulk PbTe, for example, our DFT-GGA calculations give a direct band gap of ~0.1 eV at the L point, which is a factor of two smaller than the experimental value (0.19 eV at 4 K) [60]. This "band gap problem" can be severe in semiconductor defect physics since DFT calculations may not give the exact position of the defect levels in the band gap region [165]. In my studies, I have therefore focused mainly on the chemical trends of the defect levels and how the defect states are modified in going from bulk to thin films.

4.4 Defects in Bulk and Thin Films of PbTe

4.4.1 Group III (Ga, In, and Tl) Impurities

The problem of deep defect states (DDSs) in narrow band-gap semiconductors with large electronic dielectric constants such as PbTe has been studied for several decades from both theoretical and experimental sides [134]. Inhomogeneous mixed-valence models have been proposed to explain the experimental data of group III doped

PbTe which show interesting properties such as amphoteric nature (both donor- and acceptor-like behavior for In), Fermi surface pinning (for all three), and superconductivity with large T_C (for Tl) [166]. In these models, it is suggested that In impurities exist in two valence states because In^{2+} valence state is unstable and dissociates into In^{1+} and In^{3+} (i.e., $2In^{2+} \Rightarrow In^{1+}+In^{3+}$), stabilized by strong electronic and ionic relaxations, modeled by a negative-U Hubbard model [134]. Extensive studies of these defect states have been carried out using *ab initio* DFT and supercell models where two types of defect states are found [143, 144]. One is a doubly occupied hyperdeep defect state (HDS) lying below the valence-band bottom, about 5 eV below the Fermi level. The other is a deep defect state (DDS) in the neighborhood of the narrow band gap. I will explore the physics of these defect states and see how they can help understand the experiments. As I will argue later, these calculations do not support the energetic possibility of the trivalent state.

As regards the applied aspects of the problem, which is of great interest, PbTe-based alloys doped with group III impurities have been shown to be promising for highly sensitive far-IR [134] and terahertz radiation [167] detections owing to the unique properties of the defect states. For the thermoelectric applications, functionally graded materials based on In-doped PbTe have been successfully made [168]. These materials show a large and practically constant value of the thermopower, which is necessary in order to obtain an optimal ZT value, over a wide temperature range. Since the group III doped PbTe thin films have been experimentally studied [126, 127, 128, 129, 130, 131, 132, 133], it is also necessary to find out if these localized states persist in films, or how they change compared to the bulk.

4.4.1.1 Hyper-Deep (HDS) and Deep (DDS) Defect States

Figs. 4.4(a)-4.4(c) show the DOS of PbTe doped with Ga, In, and Tl obtained in calculations where SOI was included, together with the ones without SOI. The lo-

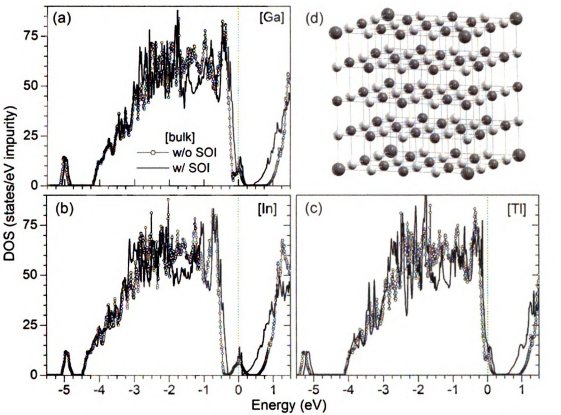

Figure 4.4: DOS of bulk PbTe doped with (a) Ga, (b) In, and (c) Tl substitutional impurities; obtained in calculations with [solid curves] and without [circled curves] SOI. The one with SOI was shifted [by $\sim +0.055$ eV (Ga), -0.008 eV (In), and $+0.081$ eV (Tl)] so that the bottom of the valence band of the two curves matched. The zero of the energy is chosen at the highest occupied state for the DOS without SOI. The (2×2×2) supercell model is shown in (d).

calized state below the bottom of the valence band (at ~ -5.0 eV) is identified as the hyper-deep defect state (HDS) and the localized (or resonant) state in the band gap region is identified as the deep defect state (DDS). The Fermi level is pinned in the middle of the localized band formed by the DDS. HDS is ~5 eV below the Fermi level and is filled (with two electrons), DDS is half-filled (with one electron up to the Fermi level). Projected DOS analysis shows that HDS is predominantly In s with some hybridization with the neighboring Te p, whereas DDS has more Te p character (compared to the HDS). We believe that these results strongly argue against the above mixed-valence model since it is too costly energetically to remove the two elec-

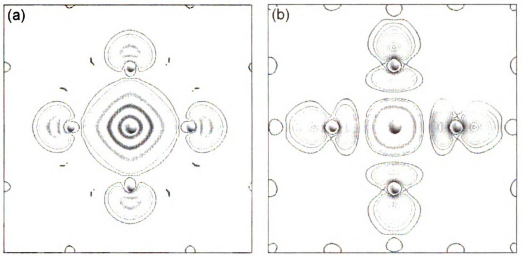

Figure 4.5: Partial charge density associated with (a) HDS (bonding) and (b) DDS (anti-bonding) created by an In substitutional impurity in bulk PbTe [in the (100) plane containing the impurity]. The results were obtained in calculations using the (3×3×3) supercell; spin-orbit interaction (SOI) was not included. The isolines in the two figures were plotted with the same scale. Large balls (at the centers) are for In, small balls are for its neighboring Te atoms.

trons from HDS to make In^{3+}. However, one can not exclude the possibility of having mixed valency of a different kind, e.g., the coexistence of In^{1+} and In^{1-}, where the electron occuping the DDS associated with one In impurity is transferred to the DDS associated with another In impurity. The first one becomes In^{1+}, whereas the second one becomes In^{1-}. More theoretical and experimental studies are needed to clarify this situation.

In order to visualize the nature of the deep defect states, I show in Figs. 4.5(a) and 4.5(b) the partial charge densities associated with HDS and DDS. As seen in the figures, HDS and DDS are predominantly the bonding and anti-bonding states of the In $5s$ and its neighboring Te $5p$. These states are strongly localized within ~6 Å around the impurity atom. The HDS is predominantly In $5s$, whereas the DDS has more contribution from Te $5p$. These strongly bound states are similar to the electrically inactive "hyperdeep level" and the electrically active "deep level" proposed by Hjalmarson *et al.* [169].

Spin-orbit effects.—In the previous section, it was shown that SOI had strong effect on the electronic structure of PbTe, especially in reducing the band gap. In this section, I would like to discuss the effects of SOI on the defect states associated with the group III impurities. Understanding of these effects in PbTe bulk may help speculate what will happen when one turns on SOI in doped PbTe films, without carrying out such calculations. As seen in Figs. 4.4(a)-4.4(c), the band gap gets reduced significantly due to the SOI with a large downward shift in energy of the bottom of the conduction band and a smaller upward shift of the top of the valence band. HDS and DDS (predominantly In s) are expected not to change much due to SOI because of their predominantly s-symmetry. Due to some non-s-character, HDS gets shifted slightly towards the bottom of the valence band. DDS in the case of In is pushed upward and gets narrower as the band gap is reduced; whereas in the case of Ga and Tl, DDS slightly sinks into the valence band. To summarize, it is important to take into account the effects of SOI in studying the defect states associated with different impurities in PbTe, although we did not include SOI in all our thin film calculations because of excessive computational time. One, however, expects to see similar bulk-like effects in PbTe films.

Larger supercell sizes.—To see how the HDS and DDS associated with the group III impurities change as one increases the impurity-impurity distance, i.e., lowers the impurity concentration, calculations using (3×3×3) supercells (the impurity-impurity distance being $\sim$ 20 Å) were carried out and SOI was included. The results are shown in Figs. 4.6(a)-4.6(c). The large supercells help reduce the impurity-impurity interaction thereby narrowing the width of the localized bands formed by HDS and DDS. The position of the DDS in the band gap region is also better reflected in these calculations. As seen in the figures, the DDS in the case of In and Ga are localized states near the conduction band bottom and near the valence band top, respectively; whereas the DDS of Tl is a resonant state near the valence band top.

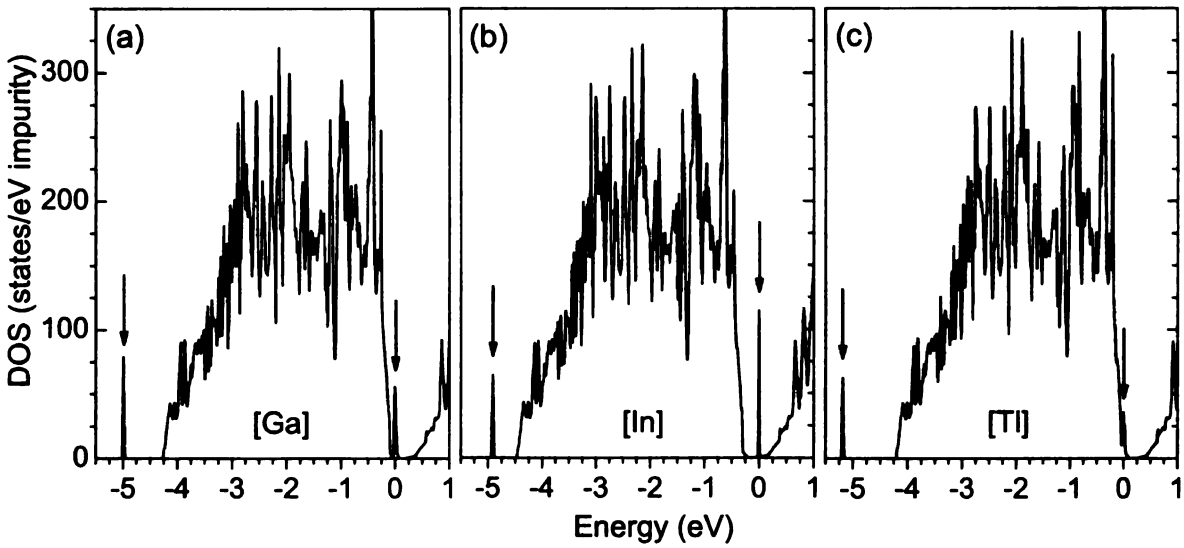

Figure 4.6: Density of states (DOS) of PbTe doped with (a) Ga, (b) In, and (c) Tl substitutional impurities obtained in calculations using (3×3×3) supercells; spin-orbit interaction (SOI) was included. The HDS and DDS are marked by arrows. The zero of the energy is set to the highest occupied state.

Interstitials at the tetrahedral sites.—Since group III impurities are believed to go into PbTe also as interstitials [129, 130], one would like to see how these interstitials affect the electronic structure of PbTe. In Figs. 4.7(a)-4.7(c), the DOS of PbTe doped with group III interstitial impurities at the tetrahedral sites obtained in calculations using (2×2×2) supercells are given. There are also HDS and DDS, similar to the substitutional case. An interstitial impurity at the tetrahedral site has 4 Te and 4 Pb atoms as the nearest neighbors (instead of 6 Te atoms as in the case of the substitutional impurity at the Pb site). This reflects in the changes in the positions and shapes of the localized bands formed by HDS and DDS. HDS is shifted downward in energy (towards the band predominantly formed by Pb 6*s*) by $\sim$ 0.4 eV (Ga and In) or 0.3 eV (Tl); whereas DDS is shifted upward (towards the conduction-band top predominantly formed by Pb 6*p*) by $\sim$ 0.2 eV (Ga), 0.02 eV (In), or 0.1 eV (Tl). DDS is filled and the Fermi level lies in the conduction band, in contrast to the substitutional case where the Fermi energy is pinned to the DDS, which is half-filled. Each interstitial atom introduces one electron to the conduction band and the Fermi level is shifted upward as one adds more interstitial atoms into the supercell. This

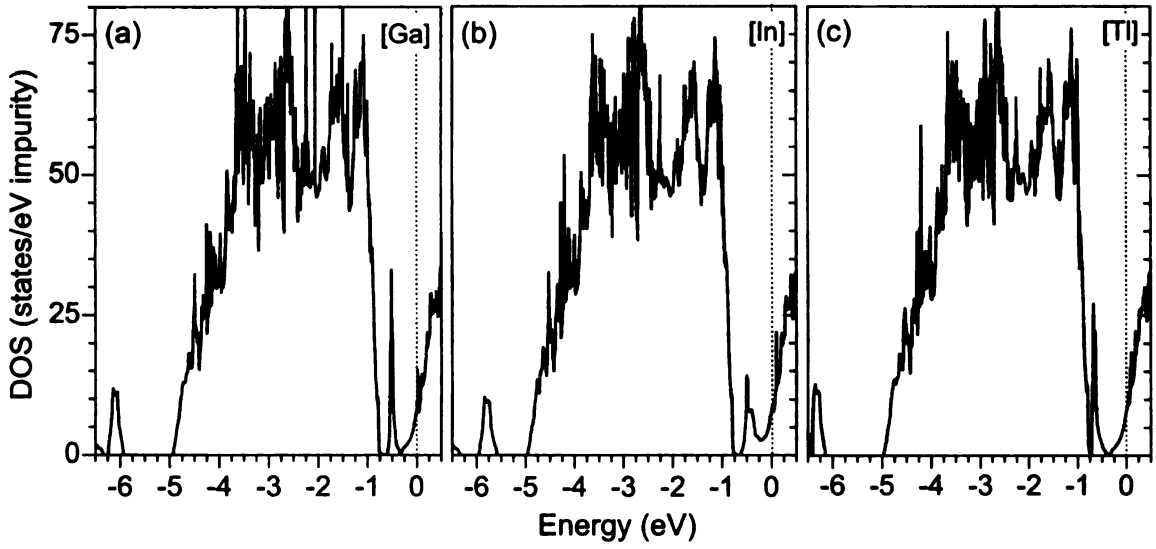

Figure 4.7: Density of states (DOS) of PbTe doped with (a) Ga, (b) In, and (c) Tl interstitial impurities at the tetrahedral sites. The results were obtained in calculations using the (2×2×2) supercell; spin-orbit interaction (SOI) was included. The zero of the energy is set to the highest occupied state.

means that the group III interstitial impurities can not lead to Fermi level pinning.

4.4.1.2 Relaxation Effects in Film Geometry

For the PbTe(001) thin films, we started with the undoped (2×2) slab as a benchmark and found that it did not show any noticeable difference in the optimized geometry compared to the (1×1) slab. For the films doped with the group III impurities, Table 4.2 gives the distances between the impurities and their neighboring Te atoms. When the impurity R is in the first layer, there are five R-Te bonds with two different bond lengths (four bonds of the same type and one bond different); whereas in the second and the third layers, there are six bonds with three different bond lengths. The impurities relax inward by different amounts. The bond lengths parallel to the surface are very close to their bulk values, whereas there are major changes in the bond lengths along the z direction. This is a consequence of the surface relaxation and periodicity constraint along the x and y directions. The anisotropy in the local environment of the impurity atoms is expected to have impact on the electronic structure of these systems. The relaxation energy is slightly different when the impurity atoms are embedded in

Table 4.2: Nearest-neighbor distance table of Ga, In, and Tl impurities substituting Pb atoms in different layers of the 9-layer (2×2) slab, and in the (2×2×2) bulk supercell. For comparison the distances from the substituted Pb atom to its neighboring Te atoms in an undoped 9-layer (2×2) slab are also given (in the last row). The integer numbers in parentheses in front of the bond length values indicate the number of bonds with similar bond lengths. The bond lengths (measured in Å) are listed in an order that the Te atoms participating in the bonds in the outer layers are given first.

Impurity	Bond	1st layer	2nd layer	3rd layer	bulk
Ga	Ga-Te	(4) 3.17	(1) 2.86	(1) 3.43	(6) 3.18
		(1) 2.88	(4) 3.17	(4) 3.18	
			(1) 3.44	(1) 3.02	
In	In-Te	(4) 3.23	(1) 3.06	(1) 3.33	(6) 3.23
		(1) 3.06	(4) 3.23	(4) 3.21	
			(1) 3.33	(1) 3.19	
Tl	Tl-Te	(4) 3.32	(1) 3.28	(1) 3.39	(6) 3.32
		(1) 3.27	(4) 3.31	(4) 3.32	
			(1) 3.46	(1) 3.26	
{undoped}	Pb-Te	(4) 3.28	(1) 3.15	(1) 3.35	(6) 3.28
		(1) 3.09	(4) 3.28	(4) 3.28	
			(1) 3.43	(1) 3.21	

different layers. It is ~1.147, 1.179, and 1.176 eV/supercell for the (2×2) slab with In impurities in the first, the second, and the third layers, respectively; larger than that of the undoped (2×2) slab (1.137 eV/supercell) by ~1-4%. For comparison, the relaxation energy of the (2×2×2) bulk supercell doped with In is 0.023 eV/supercell (it is 0.071 and 0.014 for Ga and Tl, respectively).

4.4.1.3 HDS and DDS in Films

The detailed electronic structure associated with these impurities in films will be discussed now. In Figs. 4.8(a)-4.8(c), the DOS of the PbTe(001) film doped with In are given. Besides the surface state (at ~ -10 eV; not shown in the figures) and surface resonant states [one at ~ -0.51 eV marked by the vertical arrow, see Figs. 4.8(a)] as seen in the case of the undoped PbTe slabs [Fig. 4.2(a)], there are additional (localized) defect states, one below the bottom of the valence band and

the other in the band gap region. These two states are identified as respectively HDS and DDS, similar to those in bulk PbTe [143]. As one goes from the bulk to subsurface to surface layers, the localized band formed by the HDS gets narrower and moves towards the bottom of the valence band. The shape of HDS reflects a change from three-dimensional (3D) to two-dimensional (2D) band DOS. In the bulk, where the impurity-impurity distance l ~13 Å, the HDS shows typical 3D nearest-neighbor tight-binding cubic lattice band structure with characteristic van Hove singularities in the DOS [see Fig. 4.4(b)]. In films, if the impurity-impurity distance is large ($l \gtrsim 20$ Å along the z direction), e.g., when the two In impurity atoms (one on each side of the slab) are in the first or the second layer of a 9-layer (2×2) slab, then the HDS shows a 2D square lattice band structure DOS with a sharp peak at the center of the DOS [see the circled and crossed curves in Fig. 4.8(b)]. As the two impurity atoms come closer, e.g., when they are in the third layer of each side (l ~13 Å along the z direction), the HDS shows a double-peak feature in the DOS due to the impurity-impurity interaction (along the z direction) and can be thought of as two coupled 2D band DOS [see the solid curve in Fig. 4.8(b)].

The features of the HDS discussed above can be qualitatively understood in terms of a simple tight-binding (TB) model taking into account the fact that the impurity-impurity interaction and the interaction between the impurity atom and its neighbors are smaller when the impurities are in the (sub)surface layer(s), due to the film geometry. In the case of the DDS, however, there are double- and triple-peak structures in the DOS which might not be describable in terms of a simple TB model because this band overlaps (hybridizes) with the neighboring valence and conduction bands. DDS of the In atom in the second layer gets shifted upward in energy and gets narrower [the solid curve in Fig. 4.8(b)] which possibly reflects the special local environment due to the geometric relaxation of the film. Ga and Tl show similar features [see Figs. 4.9(a)-4.9(c) and Figs. 4.10(a)-4.10(c)].

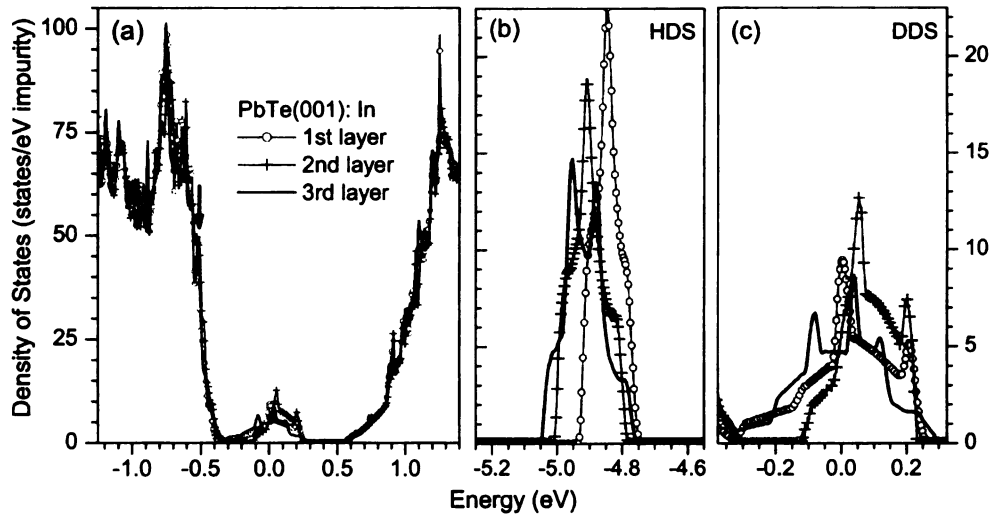

Figure 4.8: DOS of PbTe films with In substituting Pb in either the first, the second, or the third layer of the slab: (a) showing the valence-band top, the band region, and the conduction-band bottom, (b) and (c) focusing on the HDS and DDS. They were shifted by a small amount so that the bottom of the valence band DOS of the three geometric configurations matched. The vertical arrow [in (a)] marks a major peak associated with the surface resonance state(s). The zero of the energy is chosen at the highest occupied state for the slab with the impurity atoms in the third layer.

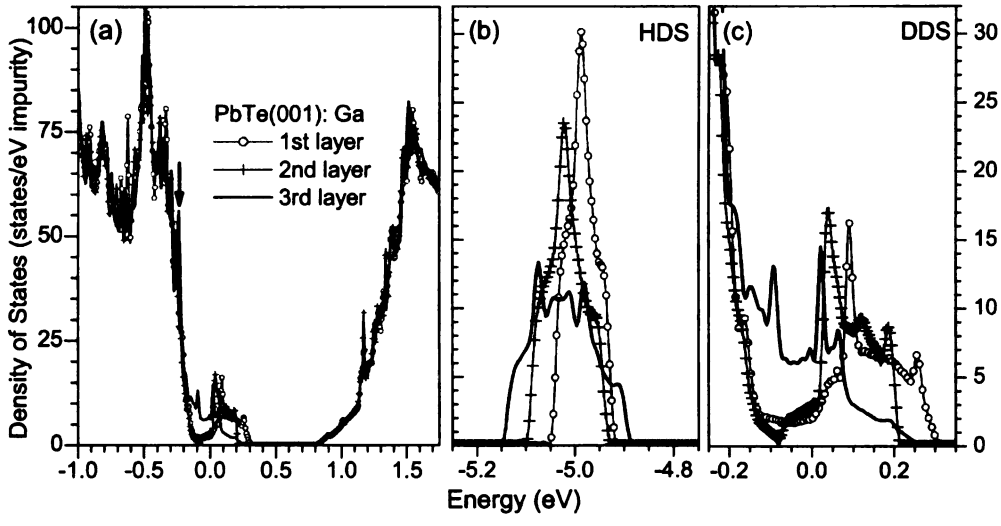

Figure 4.9: DOS of PbTe films with Ga substituting Pb in either the first, the second, or the third layer of the slab: (a) showing the valence-band top, the band region, and the conduction-band bottom, (b) and (c) focusing on the HDS and DDS. They were shifted by a small amount so that the bottom of the valence band DOS of the three geometric configurations matched. The vertical arrow [in (a)] marks a major peak associated with the surface resonance state(s). The zero of the energy is chosen at the highest occupied state for the slab with the impurity atoms in the third layer.

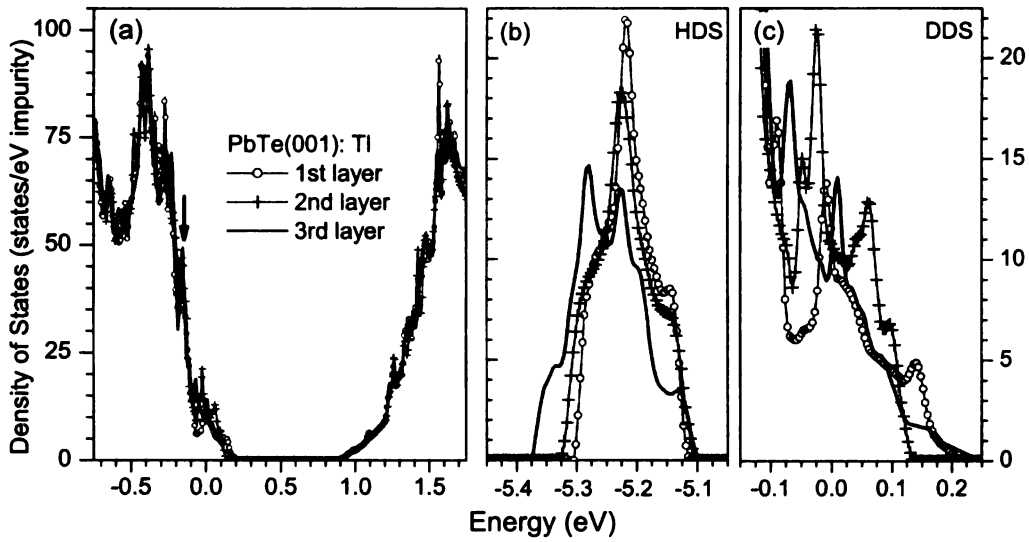

Figure 4.10: DOS of PbTe films with Tl substituting Pb in either the first, the second, or the third layer of the slab: (a) showing the valence-band top, the band region, and the conduction-band bottom, (b) and (c) focusing on the HDS and DDS. They were shifted by a small amount so that the bottom of the valence band DOS of the three geometric configurations matched. The vertical arrow [in (a)] marks a major peak associated with the surface resonance state(s). The zero of the energy is chosen at the highest occupied state for the slab with the impurity atoms in the third layer.

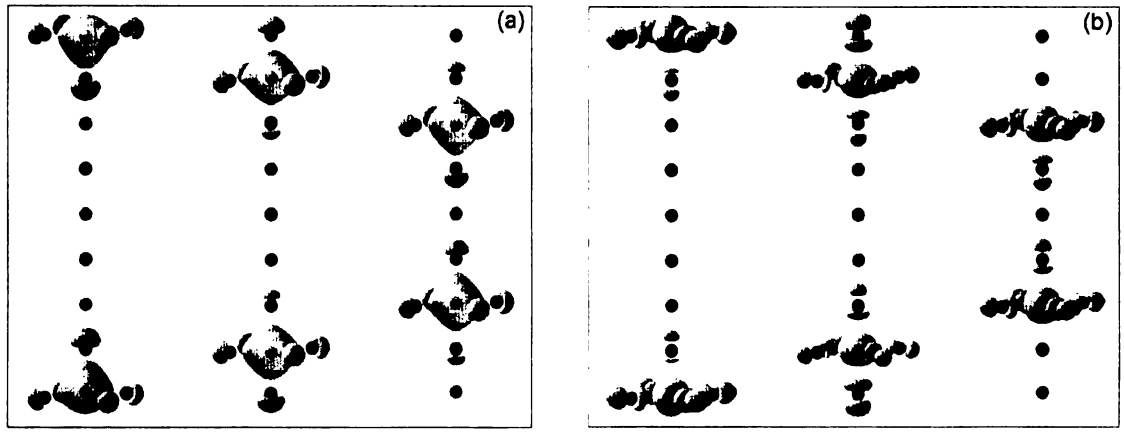

Figure 4.11: Partial charge density of In-doped PbTe films showing the nature of (a) the hyperdeep defect state (HDS, energy range: -5.1 eV to -4.7 eV) and (b) the deep defect state (DDS, energy range: -0.3 eV to 0.3 eV). The substitutional impurity (In) atoms were embedded in either the first, the second, or the third layer of the slab [from the left in the figures]. The energy was measured with respect to the Fermi level [see Figs. 4.8(a)-4.8(c)], and the isosurface is corresponding to (charge density)$\times$(supercell volume)=100. Only Pb and Te atoms which are neighboring and/or along the line connecting the two In atoms (along the z direction) are shown.

Figs. 4.11(a) and 4.11(b) show the partial charge densities associated with HDS and DDS of the substitutional In impurity embedded in either the first, the second, or the third layer of the 9-layer (2×2) slab. As seen in the figures, HDS [Fig. 4.11(a)] and DDS [Fig. 4.11(b)] are predominantly formed by In s with some hybridization with the neighboring Te p. They are actually the bonding and antibonding states of the In $5s$ and Te $5p$ and are strongly localized within ~6 Å around the impurity atom. In the film geometry, the charge distribution gets modified and depends on the location of the impurities in the slab and the distance between the impurity atoms. Because of the geometric relaxation, there is a difference in the bond length between the impurity atom and its neighboring Te atoms (see Table 4.2). A particular Te atom may have larger contribution to the partial charge density associated with HDS (DDS) than the other Te atoms because of its shorter distance from the impurity. The charge distribution of the In atom also gets distorted because of this. In the case of HDS, there is a large and localized charge density on one side of the impurity atom (In) where it has the shorter bond with the neighboring Te atom (along the z direction) [Fig. 4.11(a)]; whereas in the case of DDS, the highest charge density region is on the other side towards the surface [see the first picture from the left in Fig. 4.11(b)] or along the longer bond with the neighboring Te atom along the z direction [see the second and the third pictures from the left in Fig. 4.11(b)]. This again confirms the bonding and anti-bonding picture that was mentioned previously. The impurity-impurity interaction may also affect the charge redistribution when the two impurity atoms are brought closer (along the z direction).

Since it is well known that the transport and optical properties are very sensitive to the change of the DOS in the band gap region, one would expect to see some change in the properties of these impurities in PbTe films as compared to the bulk PbTe. However, since the DDS is not dramatically modified by the surface geometry, I believe that the main characteristics of these impurities (such as, Fermi level pinning

and, in the case of Tl, superconductivity) are preserved in PbTe films (as will be discussed in Sec. 4.4.5).

4.4.2 Other Substitutional Impurities in PbTe Films

Besides group III (Ga, In, and Tl), other impurities (R): monovalent (Ag, Na, and K), divalent (Cd and Zn), and trivalent (Sb and Bi) are also of great interest, especially for thermoelectric applications. PbTe with a large concentration of the above elements (~10%) appears to be quite promising for high temperature thermoelectric applications [15, 18, 19]. Recent *ab initio* calculations [144, 143] have shown that the DOS gets perturbed over the entire valence and conduction bands when a Pb atom is substituted by R and there are major changes in the DOS near the band gap region for most R, which should have significant impact on the transport properties of these compounds. It is found that Na does not change the DOS within ~0.5 eV of the band maxima; thus it is an ideal acceptor whereas the other alkali atoms and Ag (and Cu) give rise to an increase in the DOS near the top of the valence band and negligible change in the DOS near the bottom of the conduction band. Divalent (Zn, Cd, and Hg) and trivalent (As, Sb, and Bi) impurities give rise to strong resonant states near the bottom of the conduction band which makes these systems promising n-type thermoelectrics [144]. It is therefore very important to see how these defect states change as one goes from bulk to film geometry.

4.4.2.1 Defect States

Figs. 4.12(a)-4.12(c) show the DOS of the 9-layer (2×2) PbTe(001) slab with monovalent impurities (Ag, Na, K) in different layers. In general, the top of the valence band gets perturbed as one substitutes Pb in the (sub)surface layer by monovalent atoms and is pushed upward in energy. For Ag, this perturbation is quite strong. The defect states formed by the Ag atoms embedded in the first and the second layers get

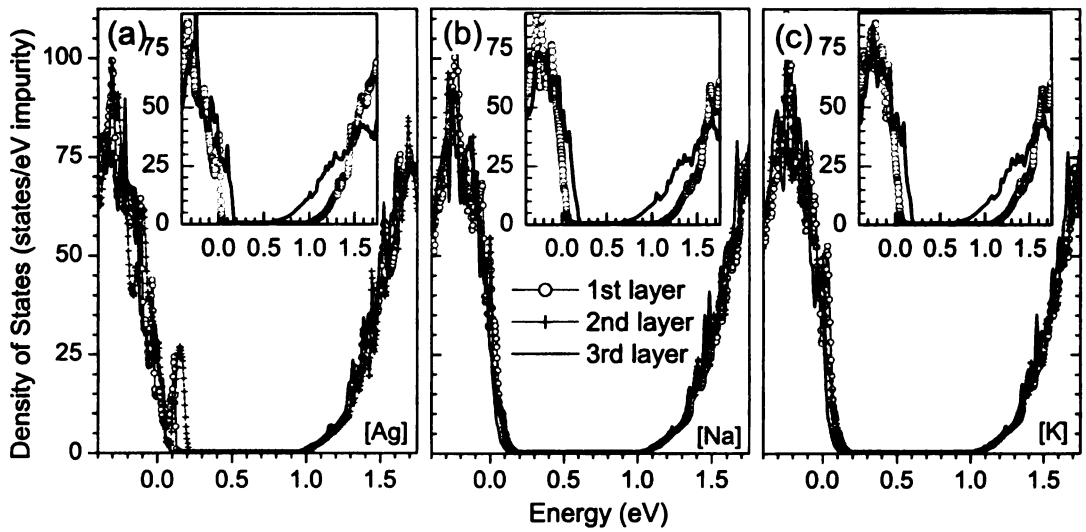

Figure 4.12: DOS of PbTe films with monovalent impurities (a) Ag, (b) Na, and (c) K substituting Pb in either the first, the second, or the third layer of the slab. They were shifted by a small amount so that the bottom of the valence band DOS of the three geometric configurations matched. For comparison, DOS of the corresponding substitutional impurity in bulk [with SOI (black curve) and without SOI (grey circled curve)] are also given [inset]; the one with SOI was shifted [by $\sim$+0.104 eV (Ag), +0.112 eV (Na), and +0.115 eV (K)] so that the bottom of the valence bands matched. The zero of the energy is chosen at the highest occupied state for the slab with the impurity atoms in the third layer (figure), and also for the bulk without SOI (inset).

shifted to the band gap and reduce the gap significantly [Fig. 4.12(a)]. To compare the DOS for different positions of the (same) impurity, we made a constant shift such that the valence band minimum coincided for all the systems. The Fermi levels shift accordingly. They are at +0.032 eV, +0.148 eV, and 0.0 eV for Ag embedded in the first, the second, and the third layer of the slab, respectively; for Na they are at +0.040 eV, +0.030 eV, and 0.0 eV; and for K they are at +0.041 eV, +0.036 eV, and 0.0 eV. The shifts of the Fermi levels are monotonic in the case of Na and K as one goes from the third to the second to the first layer, but non-monotonic for Ag.

The DOS of Zn and Cd doped PbTe(001) films also get modified in going from bulk to film and from surface to subsurface layers [see Figs. 4.13(a) and 4.13(b)]. There are possible additional resonant states near the top of the valence band which were not seen in the bulk. The defect states near the bottom of the conduction band

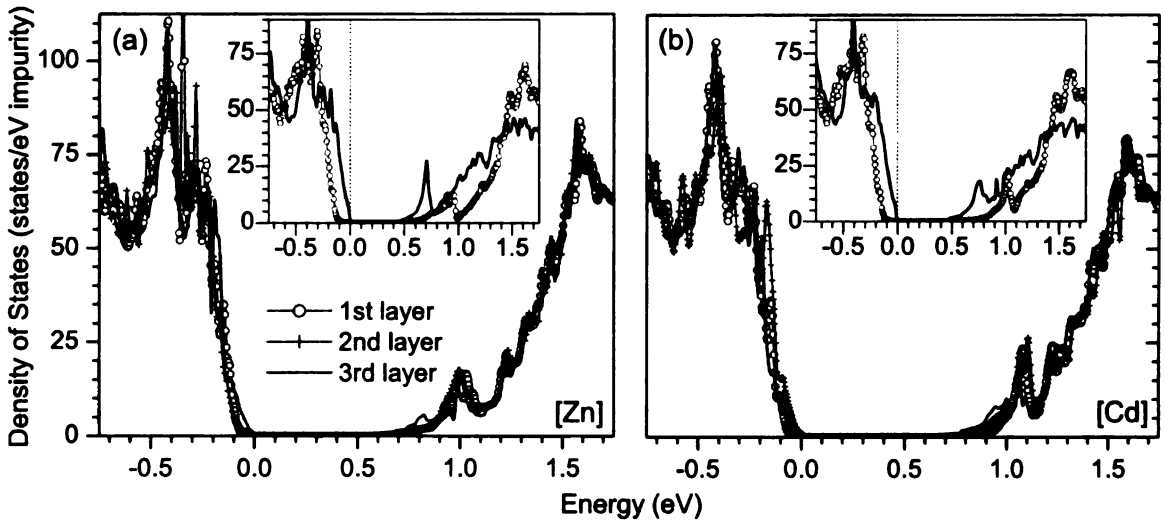

Figure 4.13: DOS of PbTe films with divalent impurities (a) Zn and (b) Cd substituting Pb in either the first, the second, or the third layer of the slab. They were shifted by a small amount so that the bottom of the valence band DOS of the three geometric configurations matched. For comparison, DOS of the corresponding substitutional impurity in bulk [with SOI (black curve) and without SOI (grey circled curve)] are also given [inset]; the one with SOI was shifted [by ∼+0.144 eV (Zn) and +0.142 eV (Cd)] so that the bottom of the valence band of the two curves matched. The zero of the energy is chosen at the highest occupied state for the slab with the impurity atoms in the third layer (see figure), and also for the bulk without SOI (inset).

get shifted. The DOS of Sb and Bi doped PbTe(001) films are shown in Figs. 4.14(a) and 4.14(b). For these impurities, the Fermi level is in the conduction band. There are sharp resonant states near the bottom of the conduction band. The Fermi level gets shifted monotonically, in going from the first to the second to the third layers; they are, respectively, at +0.059 eV, +0.035 eV, and +0.0 eV in the case of Sb, +0.020 eV, +0.017 eV, and +0.0 eV in the case of Bi. There are additional resonant states near the top of the valence band when Pb atoms in the third layer are substituted by Sb or Bi atoms. This is possibly due to the strong impurity-impurity interaction along the z direction in this geometric configuration.

4.4.2.2 Spin-Orbit Effects

Since the defect states associated with some of these impurities have a predominantly p-symmetry, spin-orbit interaction (SOI) is expected to have larger effects on these

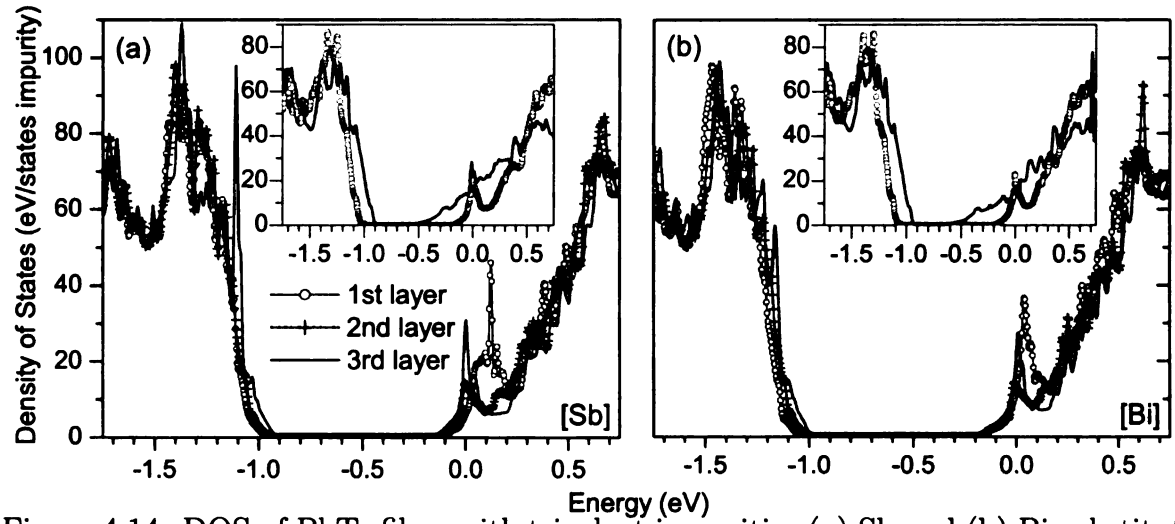

Figure 4.14: DOS of PbTe films with trivalent impurities (a) Sb and (b) Bi substituting Pb in either the first, the second, or the third layer of the slab. They were shifted by a small amount so that the bottom of the valence band DOS of the three geometric configurations matched. For comparison, DOS of the corresponding substitutional impurity in bulk [with SOI (black curve) and without SOI (grey circled curve)] are also given [inset]; the one with SOI was shifted [by ~ -0.243 eV (Sb) and -0.323 eV (Bi)] so as the bottom of the valence band of the two curves matched. The zero of the energy is chosen at the highest occupied state for the slab with the impurity atoms in the third layer (see figure), and also for the bulk without SOI (inset).

states (besides reducing the band gap). I give in the insets of Figs. 4.12(a)-4.12(c), Figs. 4.13(a) and 4.13(b), and Figs. 4.14(a) and 4.14(b) the DOS of the bulk systems obtained in calculations where SOI was included, together with the ones without SOI (only scalar relativistic effects were included) for comparison. As seen in these figures, the band gap gets reduced significantly with a large downward shift in energy of the bottom of the conduction band and a small upward shift of the top of the valence band. Except for the band gap shrinking, the DOS of PbTe bulk doped with Ag, Na and K do not show any other noticeable change [Figs. 4.12(b)-4.12(c)]. The average position of the defect states in the case of the divalent impurities with s valence electrons [$4s^2$ (Zn) and $5s^2$ (Cd)] is mainly determined by the scalar relativistic effects which were included in all the calculations. They shift downward in energy (to the middle of the band gap region) as one goes from Zn (Z=30) to Cd (Z=48) [see the circled grey curves in the insets of Figs. 4.13(a) and 4.13(b)]. When SOI is turned on, the bottom of the conduction band is pushed downward significantly and also

the defect states get narrower [see the black curves in the insets of Figs. 4.13(a) and 4.13(b)]. SOI also affects the average position of the defect states since these states (predominantly s-character) have some non-s-character. In the case of the trivalent impurities (Sb and Bi) of p-type, the defect states are strongly affected by SOI because of their predominantly p-character [see the insets in Figs. 4.14(a)-4.14(b)]. Therefore it is essential to take into account the effects of SOI in studying the defect states associated with these types of impurities in PbTe (either bulk or films).

4.4.3 Pb and Te Vacancies

Pb and Te vacancies in bulk PbTe were theoretically studied a long time back by Parada and Pratt [136] using a Slater-Koster model and Wannier function basis constructed out of a finite number of PbTe bands, and by Hemstreet [138] using the XSW-cluster method. These studies showed that a single Pb vacancy gave two holes in the valence band, producing p-type PbTe, whereas each Te vacancy produced two electrons outside of a filled valence band, giving to n-type PbTe. However there is some difference between the results obtained in these two works. Parada and Pratt found that the defect state (accommodating the two extra electrons) associated with the Te vacancy was in the conduction band; whereas Hemstreet found it was in the gap region just below the conduction-band edge. The discrepancy was then ascribed to the self-consistent relaxation of the electronic states that was not included in Parada and Pratt's calculations [138]. Recent *ab initio* studies [144] provide more details on the effects of Pb and Te vacancies in PbTe, e.g., the DOS enhancement near the top of the valence band in the case of the Pb vacancy and the nature of the additional states appearing in the band gap region and near the bottom of the conduction band associated with the Te vacancy, which was not seen in earlier calculations [136, 138]. It should be noted that atomic relaxation, which can be important in the presence of the vacancies, was not included in all the above mentioned works. It's effects are

taken into account in the following calculations.

4.4.3.1 Bulk

We started with vacancies in bulk PbTe created at the center of the (2×2×2) supercells. For the Pb vacancy, the 6 nearest-neighbor Te atoms relax slightly outward (towards the supercell boundaries) by ∼0.024 Å (0.7% of the Pb-Te bond length in pure PbTe bulk), the 12 next nearest-neighbor Pb atoms relax inward (towards the center of the supercell) by ∼0.05 Å. In the case of Te vacancy, the 6 nearest neighbor Pb atoms relax inward (towards the center of the supercell) by ∼0.07 Å, and the 12 next nearest-neighbor Te atoms also relax inward by ∼0.012 Å. The difference between the Pb and Te vacancies is due to the difference in their atomic radii and the asymmetric relaxation of their respective neighboring atoms. Atomic relaxation results in lowering the energy of the systems, by ∼60 and ∼26 meV/supercell for Pb and Te vacancies, respectively. As regards the electronic structure, there are noticeable changes in the DOS due to the relaxation. The top of the valence band DOS together with the peak (in the case of Pb vacancy) shifts downward in energy by ∼0.04 eV. The top of the valence band DOS does not change in the case of Te vacancy but the defect state in the band gap region shifts downward by ∼0.1 eV. This leads to a stronger overlap of the Pb vacancy state with the valence band, whereas the Te vacancy goes deeper into the band gap. However, the atomic relaxation leaves the remaining part of the DOS almost unaffected, except in the case of Pb vacancy where the top of the Te 5s band DOS (at ~ -9.8 eV) is pushed downward by ∼0.05 eV (the lower part of the Te 5s band DOS is unaffected).

Vacancy-induced states.—In the insets of Figs. 4.15(a) and 4.15(b) the DOS of PbTe (bulk) with Pb and Te vacancies, respectively, are given. In the case of Pb vacancy, there is a peak (half-width of ∼0.1 eV) near the top of the valence band with the Fermi level passing through it. This peak was not clearly seen, possibly

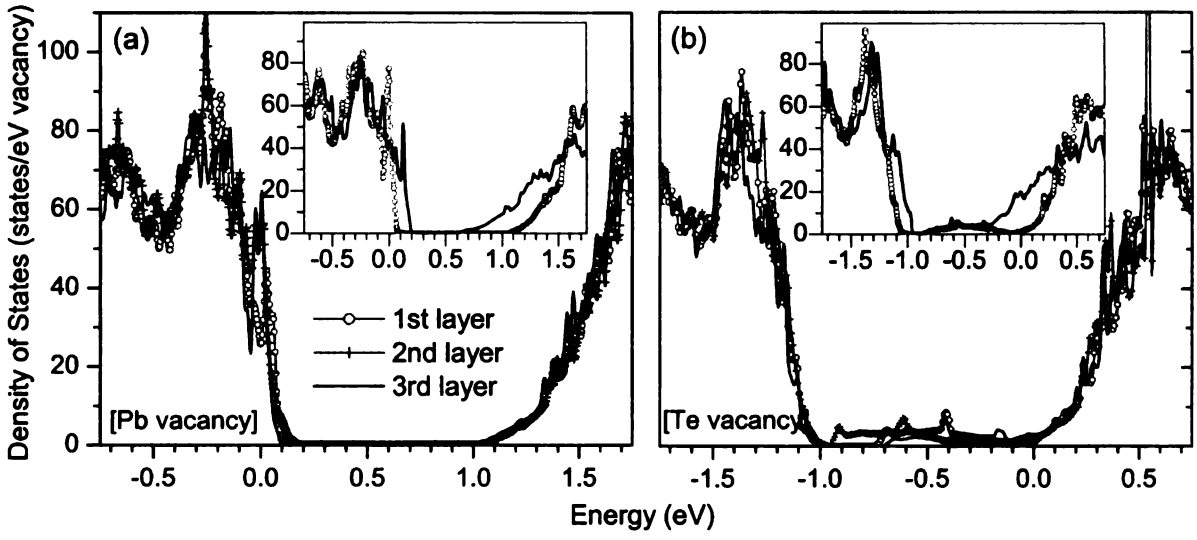

Figure 4.15: DOS of the PbTe films with (a) Pb and (b) Te vacancies created in either the first, the second, or the third layer of the slab. They were shifted by a small amount so that the bottom of the valence band DOS of the three geometric configurations matched. For comparison, DOS of the corresponding substitutional impurity in bulk [with SOI (black curve) and without SOI (grey circled curve)] are also given [inset]; the one with SOI was shifted [by $\sim$+0.106 eV (V_{Pb}) and -0.336 eV (V_{Te})] so that the bottom of the valence band of the two curves matched. The zero of the energy is chosen at the highest occupied state for the slab with the vacancies in the third layer (see figure), and also for the bulk without SOI (see inset).

due the smearing method used in obtaining the DOS, in the earlier work [144]. Pb vacancies, therefore, act like acceptors. In the case of Te vacancy, there is a defect state in the band gap region and near the bottom of the conduction band, which was however seen in earlier calculations without relaxation [144]. This makes Te vacancies act like donors. SOI has strong effects on the defect states associated with both Pb and Te vacancies. There is a splitting of the peak near the top of the valence band in the case of Pb vacancy after turning on the SOI, with the smaller peak pushed towards the band gap region and lying just above the Fermi level [at $\sim$0.106 eV above the original Fermi level; see the black curve in the inset of Fig. 4.15(a)]. SOI reduces the band gap in the case of Te vacancy without changing the defect state much, except that there are possible additional resonant states near the valence-band top.

Nature of the vacancy-induced states.—To see the spatial characteristics of these vacancy-induced defect states, in Figs. 4.16(a) and 4.16(b), the partial charge densities

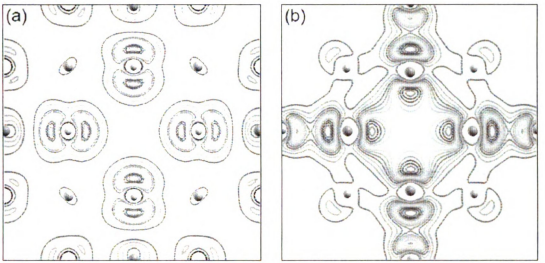

Figure 4.16: Partial charge densities [in the (100) plane containing the vacancy] associated with defect states created by (a) Pb (energy range: -0.05 eV to 0.15 eV) and (b) Te (energy range: -1.0 eV to 0.0 eV) vacancies in PbTe (bulk). The energy was measured with respect to the Fermi level [see the insets of Figs. 4.15(a) and 4.15(b)]. The isolines in the two figures were not plotted with the same scale. Only Pb (large balls) and Te (small balls) atoms which are neighboring and/or along the lines connecting the vacancies are shown.

associated with the peak near the top of the valence band (for Pb vacancy) and with the defect state in the band gap region (for Te vacancy), respectively, are given. The Pb-vacancy state is formed predominantly by the p states of the six Te atoms enclosing the Pb vacancy, whereas the Te-vacancy state is formed predominantly by the p states of the six Pb atoms enclosing the Te vacancy. Ahmad *et al.* [144] also came up with a similar conclusion after carrying out PDOS analysis. As clearly seen in Figs. 4.16(a) and 4.16(b), these vacancy-induced defect states are highly localized with the majority of their total charge density around the neighboring atoms of the vacancies. These results do not support the statement by Hemstreet [138] that the wave functions associated with the holes (in the case of Pb vacancy) were expected to be delocalized within the solid. This is because it was thought that the upper valence band (predominantly Te $5p$) was unaffected by the presence of the Pb vacancy [138], which is not the case as seen in the inset of Fig. 4.15(a).

4.4.3.2 Films

Next we discuss the results for the vacancy-induced states in film geometry. One expects that SOI has similar effects in PbTe films as in the bulk. However, it was not included in the present calculations due to excessive computing time. Atomic relaxation is expected to be large in the films due to the reduced constraint, especially when the vacancies are in the surface and the subsurface layers. The relaxation patterns are found to be very different depending on the position of the vacancy and the vacancy type. They are also more complicated than the bulk and are highly anisotropic because of the film geometry and the surface relaxation. There is significant change in the bond length along the z direction (perpendicular to the film) in the presence of the vacancies.

For Pb vacancy in the first (surface) layer, the Te atom in the second layer (nearest neighbor of the removed Pb atom) relaxes outward (towards the vacancy) by ~0.018 Å, the Pb atom in the third layer relaxes outward by ~0.184 Å. This results in a shortening in the bond length between these two atoms by ~0.166 Å (5%). For the Te vacancy in the same configuration, the Pb atom in the second layer relaxes outward (towards the Te vacancy) by ~0.461 Å and the Te atom in the third layer relaxes inward by 0.017 Å which shortens their bond length by ~0.5 Å (14%). In the second configuration where a Pb (Te) vacancy is in the second layer, the Te (Pb) atom in the first layer relaxes outward (inward) by ~0.299 Å (0.457 Å), the Te (Pb) atom in the third layer relaxes inward by ~0.087 Å (0.055 Å). For the third configuration where a Pb (Te) vacancy is in the third layer, the relaxation is similar to that in the bulk but with some anisotropy due to the surface and the constraint in the fourth layer (kept fixed in bulk geometry). There are also lateral relaxations in the presence of the vacancies. The Te (Pb) neighboring atoms of the Pb (Te) vacancy in the plane parallel to the surface move away from (towards) the Pb (Te) vacancy by ~ 0.066 Å (0.001 Å) in the first configuration, 0.003 Å (0.096 Å) in the second

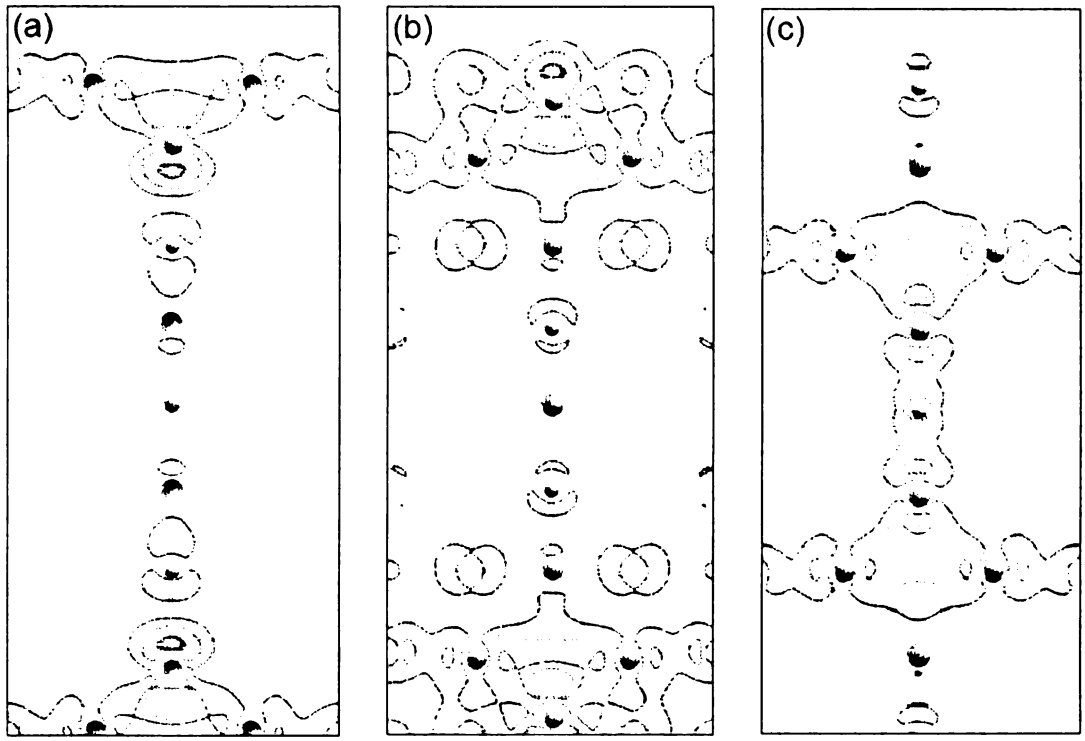

Figure 4.17: Partial charge density [in the (100) plane containing the vacancies] associated with the defect state (in the energy range: -1.0 eV to 0 eV) formed by Te vacancies in the PbTe(001) films. The vacancies were created in (a) the first, (b) the second, and (c) the third layer of the slab. The energy was measured with respect to the Fermi level [see Fig. 4.15(b)]. Only Pb (large balls) and Te (small balls) atoms which are neighboring and/or along the line connecting the two Te vacancies (along the z direction) are shown.

configuration, and 0.038 Å (0.040 Å) in the third configuration. All the positions are measured with respect to the fixed central layer; and the comparisons are made with the corresponding undoped slab.

Vacancy-induced states and the effects of the surface geometry.—The DOS of the PbTe(001) films with Pb and Te vacancies are shown in Figs. 4.15(a)-4.15(b). There is a rearrangement of the states near the top of the valence band and the bottom of the conduction band, and in the band gap region. The peak near the top of the valence band associated with the Pb vacancy created in the first layer is shifted significantly towards the energy gap [see Fig. 4.15(a)]. The Fermi levels get shifted monotonically, in going from the first to the second to the third layers; they are ,

respectively, at +0.021 eV, +0.012 eV, and +0.0 eV. The defect state associated with the Te vacancies created in the second layer is pushed downward in energy towards the top of the valence band [see Fig. 4.15(b)]. In order to see the nature of the defect states associated with the Te vacancies and their evolution in going from the first to the second, to the third layers, we show in Figs. 4.17(a)-4.17(c) the isolines (lines connecting points of equal value) of the partial charge density associated with these states in the (100) plane (in the energy range −1.0 eV to 0 eV). There is large charge density below the Pb atom neighboring the Te vacancy in the first layer [Fig. 4.17(a)] and above the Pb atom neighboring the Te vacancy in the second layer [Fig. 4.17(b)]. These are the Pb lone pairs formed in the presence of a Te vacancy in the system since there is no Te atom to take two electrons from the Pb atom.

4.4.4 Defect Formation Energy

Energetic studies of defects in PbTe films can shed some light on the doping mechanisms of these elements in PbTe nanostructures and might tell us something about their distribution in nano-dot embedded PbTe-based bulk materials [15, 18, 19, 110, 111]. The formation energy (E_f) of a neutral impurity atom R replacing a Pb atom in the Pb sublattice is defined as

$$E_f = E_0^R - E_0 + \mu_{\mathrm{Pb}} - \mu_R, \tag{4.4}$$

where E_0 and E_0^R are respectively the total energy of the supercells of pure PbTe and one with one impurity R, and μ_i's are the chemical potentials of the constituent elements. This equation is adapted from Hazama *et al.* [142], where the chemical potentials are calculated from the energy per atom in each standard metallic state.[4]

The formation energies (E_f) for various substitutional impurities in different lay-

[4]The total energy (eV/atom) of some elements in their standard metallic states used in this chapter: −3.572 (Pb), −3.139 (Te), −2.871 (Ga), −2.560 (In), −2.245 (Tl), −2.826 (Ag), −1.308 (Na), −1.028 (K), −1.269 (Zn), −0.911 (Cd), −3.875 (Bi), and −4.116 (Sb).

Table 4.3: Formation energies (E_f, in eV/defect) of different substitutional impurities and native defects embedded in the first, the second, or the third layer of the 9-layer (2×2) slab, and in the (2×2×2) bulk supercell. Relative formation energies ($E_0^R - E_0$) are also included in the brackets.

Defect	1st layer	2nd layer	3rd layer	bulk
Ag	1.370 (2.116)	1.354 (2.100)	1.439 (2.185)	1.459 (2.205)
Na	−0.299 (1.965)	−0.277 (1.987)	−0.281 (1.983)	−0.280 (1.984)
K	−0.535 (2.009)	−0.351 (2.193)	−0.338 (2.206)	−0.317 (2.227)
Zn	0.774 (3.077)	0.774 (3.077)	0.875 (3.178)	0.938 (3.241)
Cd	0.308 (2.969)	0.278 (2.939)	0.345 (3.006)	0.367 (3.028)
Sb	1.345 (0.801)	1.259 (0.715)	1.310 (0.766)	1.303 (0.759)
Bi	1.035 (0.732)	0.959 (0.656)	0.983 (0.680)	0.974 (0.671)
Ga	0.785 (1.485)	0.836 (1.536)	0.851 (1.551)	0.856 (1.556)
In	0.441 (1.453)	0.509 (1.521)	0.472 (1.484)	0.475 (1.487)
Tl	0.541 (1.868)	0.694 (2.021)	0.636 (1.963)	0.655 (1.982)
V_{Pb}	2.006 (5.578)	2.178 (5.750)	2.144 (5.716)	2.187 (5.759)
V_{Te}	1.928 (5.067)	1.920 (5.059)	2.152 (5.291)	2.135 (5.274)

ers of a 9-layer (2×2) slab have been calculated and the results are summarized in Table 4.3. As seen in Table 4.3, the formation energies of Na and K are negative, indicating that these two impurities are readily incorporated into PbTe. The monovalent impurities have the highest E_f in the bulk (Ag and K) or in the second layer but very close to the bulk value (Na); E_f tends to decrease in going from bulk to the subsurface and the surface layers. The divalent impurities (Zn and Cd) have the highest E_f in the bulk and E_f seems to decrease in going from the bulk to the subsurface and the surface layers (Zn) or has a shallow valley with the lowest E_f in the second layer (Cd). The difference between E_f values for the bulk and the first (surface) layer is 164 meV (Zn) and 59 meV (Cd). The two trivalent impurities (Sb and Bi) all have the highest values of E_f in the first layer which are also higher than that in the bulk by 42 meV (Sb) and 61 meV (Bi). In addition, there is a valley in between the first and bulk-like layers with the lowest E_f in the second layer.

The formation energy for Ga increases as one goes from the first (surface) to the

second and the third (subsurface) layers and to the bulk. There is an increase of 51 meV in E_f as one goes from the first to the second layer, 15 meV from the second to the third layer, and 5 meV from the third layer to the bulk. These results suggest that Ga likes to be on the surface. In and Tl also have the lowest E_f in the first layer. However, unlike Ga, these two substitutional impurities have highest E_f in the second layer, even higher (34 meV and 39 meV for In and Tl, respectively) than that in the bulk. Therefore, there is a potential barrier in the second layer in the case of In and Tl. This barrier also creates a shallow valley between the second and the bulk-like layers acting like a trap to keep the impurity atoms. This difference between Ga and In(Tl) should have important consequences in doping these elements into PbTe films and nanocrystals. One expects that Ga atoms will be easily annealed out to the surface whereas In and Tl atoms can be trapped in the subsurface layers.

The formation energy of Ag and Sb in bulk PbTe when they are both present and infinitely separated apart from each other is 2.762 eV (obtained by summing over the formation energy of Ag and that of Sb); in agreement with the value (2.70 eV) obtained by Hazama *et al.* [142].

The formation energy ($E_f^{v,i}$) of a vacancy V_X at the X site (X=Pb, Te) or an interstitial X_i is defined as [91]

$$E_f^{v,i} = E_0^{v,i} - E_0 \pm \mu_X, \tag{4.5}$$

where $E_0^{v,i}$ and E_0 are respectively the total energy of the supercell with and without the vacancy V_X or the interstitial X_i, and μ_X is the chemical potential of X (with a + sign for vacancy and a − sign for interstitial). The formation energy of the vacancies at the Pb and Te sites in PbTe(001) films and in bulk PbTe are given in Table 4.3. Both types of vacancies have their lowest formation energies in the first layer of the slab. Pb vacancy, like In and Tl impurities, has a barrier potential in the second layer (although its relative formation energy is 9 meV lower than that in the

bulk); whereas the Te vacancy has a potential barrier in the third layer (E_f^v of the vacancy in this layer is 17 meV higher than that in the bulk). The formation energy of Te vacancy is lower than that of Pb vacancy by about 50 meV. As in the case of the substitutional impurities, one expects that these features may have implication on the mechanism of creating vacancies in PbTe surfaces/thin films and nanocrystals. It is noted that static-lattice calculations carried out by Duffy *et al.* [170] in MgO also showed that formation energies of vacancies were not monotonic functions of distance from the (001) surface to the bulk, but there was a potential barrier in the second (for the anion vacancy) or the third (for the cation vacancy) layer.

To check the robustness of our results, the number of layers was increased to N=11 (176 atoms/supercell) from N=9 (144 atoms/supercell). The results for for 11-layer (2×2) In-doped PbTe (001) slab did not have any noticeable difference from the 9-layer one. Formation energies of In in the first, the second, and the third layer of a 11-layer slab are respectively 0.444 eV, 0.500 eV, and 0.478 eV which are very close (within 1%) to those obtained in a 9-layer slab (Table 4.3). The localized bands formed by HDS and DDS in a 11-layer slab simply get narrower because of the reduced impurity-impurity interaction along the z direction. Therefore the 9-layer (2×2) slabs are good enough for the present purposes. Neither atomic relaxation nor the removal of the constraint on the 3 central layers of the 9-layer (2×2) slab (i.e. all layers are allowed to relax) made any significant change the energy landscapes of the systems. The formation energies for the same series of calculations are 0.446 eV, 0.530 eV, and 0.492 eV [for unrelaxed 9-layer (2×2) slabs]; and 0.445 eV, 0.508 eV, and 0.470 eV (when all layers of the slabs were allowed to relax).

4.4.5 Theoretical Results *vis-à-vis* Experimental Data

I will now discuss the available experimental data of PbTe films and try to explain them in the light of the theoretical calculations. It is known that PbTe has a range

of nonstoichiometry accompanied by either Pb or Te vacancies, even in nominally undoped samples. One usually has to take them into account to interpret the experimental data [114, 171, 117, 129, 130, 126]. Tunneling spectroscopy studies by Esaki *et al.* [171] in PbTe-Al_2O_3-metal junctions revealed the existence of an atomic-like spectrum and spin splitting arising from imperfections (possibly Te vacancies) in the vicinity of PbTe surface. Although the energies of major (deep) levels in the spectrum are well represented by $E_n - E_c = 1.6/n^2$, where n is an integer and E_c is the conduction band edge, they can not be explained in terms of a hydrogenic model without assuming an extremely small dielectric constant of PbTe. This series of deep defect states was also observed in Pb(Tl)Te films by Murakami *et al.* [133] and was thought to exist near the surface region where the p-type majority carriers (due to Tl impurities) and the n-type minority carriers (due to Te vacancies or excess Pb atoms) co-exist. The calculations for PbTe films (with and without defects) also show a series of resonant states near the conduction-band bottom; however, I can not say with certainty if they are related to the observed states without further analysis.

Polycrystalline n-type PbTe films were shown to have larger Seebeck coefficient and lower electrical conductivity than in the bulk at the same carrier concentration (see Ref. [117] and references therein). This was explained by potential scattering from the Te vacancies at the grain boundaries. The argument was based on the fact that the films were prepared on heated glass substrates in vacuum where there was re-evaporation of the material during film preparation, resulting in a depletion of the volatile element (chalcogen atoms) in the grain boundary region. This is consistent with our energetic studies which show that it is easier to create a Te vacancy than a Pb vacancy (either in the bulk or in films). Single phase $Pb_{1-x}In_xTe$ films on Si substrates were produced by Samoilov *et al.* [129, 130] using a modified hot-wall method and vapor-phase doping. The lattice parameter of the films was found to vary nonmonotonically with In content, suggesting that In atoms were possibly

incorporated into the films as interstitials. It is noted that our *ab initio* calculations of bulk PbTe with group III interstitial impurities at the tetrahedral site show that group III interstitials can not lead to Fermi level pinning. One should, therefore, carry out transport measurements to confirm if there are In interstitials present in the samples. Bocharova *et al.* [172] in another study claimed that the interstitial In atoms were neutral and did not contribute to the carrier concentration. This can be understood if both substitutional and interstitial impurities are present simultaneously.[5]

$Pb_{1-x}Ga_xTe$ films on Si and SiO_2 substrates were produced by Ugai *et al.* [127, 128] using a modified hot-wall method. The incorporation of Ga into PbTe films has strong effects on the carrier (hole) concentration and mobility; the $Pb_{1-x}Ga_xTe$ films with $0.004 < x < 0.008$ have low carrier concentration and high carrier mobility. In another work by Akimov *et al.* [126], *n*-Pb(Ga)Te epitaxial films were prepared by the hot-wall technique on $BaF_2(111)$ substrates. The main properties of the films were found to be similar to those of bulk *n*-Pb(Ga)Te single crystals with the Fermi level pinned within the band gap. Besides, the resistivity of the Pb(Ga)Te films depended strongly on the substrate temperature, reducing from 10^8 down to 10^{-2} Ω cm at 4.2 K. The resistivity reduction was claimed to be associated with a slight excess of Ga, disturbing the Fermi level pinning within the energy gap of *n*-Pb(Ga)Te films [126]. This can be understood in terms of the presence of Ga interstitials in these systems (see Section 4.4.1.1), where it behaves like a *n*-type impurity.

Tl doped PbTe films have been studied mainly in connection with superconductivity. Murakami *et al.* [131] studied Pb(Tl)Te films prepared by hot-wall epitaxial (HWE) method and showed that there was a superconducting transition ($T_C^{max} \sim 1.4$ K at the hole concentration $\sim 10^{20}$ cm^{-3}, for Tl concentration of $\geq$0.5-0.6 at.%) with

[5]Energetically, it is more favorable to have substitutional and interstitial In impurities simultaneously than just the latter. The formation energies of In impurities [eV per impurity or impurity complex]: +0.476 (substitutional at the Pb site), +1.981 (interstitial at the tetrahedral site), +1.509 (the substitutional at the center of the supercell and the interstitial at the first tetrahedral site from the center present simultaneously). The results were obtained in calculations using the (2×2×2) supercell; spin-orbit interaction was not included.

strong reduction in the carrier mobility. Higher superconducting T_C was realized with stronger suppression in mobility, suggesting a correlation between superconductivity and resonance scattering of carriers with quasi-localized Tl impurity states. The existence of resonant states associated with Tl impurities is consistent with my calculations. Murakami *et al.* [132] found via tunneling measurement that there were two Tl impurity states separated by 13-15 meV; the upper state with a half-width of ~6 meV, about a half of that for the other state. One possible source of this splitting is when two Tl impurities come close to each other, the coupling between two resonant states splits their degeneracy.

Finally, I would like to point out that there are possibilities of simultaneously having two or more types of defects and/or some sort of defect complexes in real samples of bulk PbTe and films; and the experimental data may not be interpreted in terms of single point defects alone. It will be interesting to see how different defects behave when they co-exist (see the following chapter). Furthermore, the defect calculations might be only considered as the first-order approximation to the real systems, especially for some of the heavily doped thermoelectric materials such as $AgPb_mSbTe_{2+m}$ [15], $Ag(Pb_{1-y}Sn_y)_mSbTe_{2+m}$ [18], $Na_{1-x}Pb_mSb_yTe_{2+m}$ [19], and $K_{1-x}Pb_mSb_yTe_{2+m}$ [20], where they may not be considered as solid solutions because of the nanostructuring and secondary phases present in the systems [17]. Besides, it is not always straightforward to make a connection between the electronic structure obtained in the zero-temperature DFT calculations and the measured transport properties at finite, particularly high temperatures [173].

4.5 Doped PbTe Nanoclusters

Recently, there has been a great deal of interest in colloidal lead chalcogenide (PbS, PbSe, and PbTe) nanoclusters/nanocrystals because of their potential applications in thermoelectric, electronic, and optoelectronic devices [122, 123, 174, 175, 176, 177].

Nano- and microcrystals of various morphologies, including face-open nanoboxes, microflowers, semi-microflowers, cubic nanoparticles, spherical nanoparticles, nanorods etc... have been observed in experiments [122, 123, 174, 175, 176, 177]. Theoretically, although there are several studies of PbS and PbSe (nano)clusters [178, 179, 180], to the best of my knowledge, there are very few, if any, reported works on PbTe (nano)clusters. Since it is known that surface relaxation is stronger in PbTe compared to the other two lead chalcogenides [149] (also see the discussion in Sec. 4.3), one expects to see interesting properties in both the atomic and electronic structures of PbTe (nano)clusters.

As in the bulk semiconducting materials, to make semiconductor nanocrystals suitable for different applications, one has to be able to control their "carrier concentration". In modern semiconductor technology, this can be done by doping or by charging [181]. Recently, attempts to dope PbSe nanocrystals with Mn have been carried out [175]. It is, therefore, important to see how doping is possible in different lead chalcogenide nanocrystals and how the impurities behave in these systems compared to their bulk counterpart. Unlike doped silicon nanocrystals where there are many theoretical works have been done [182, 183, 184, 185, 186], to the best of my knowledge, nothing much has been done on doped lead chalcogenide nanocrystals.

In this section, structural properties of undoped PbTe clusters in different sizes (up to 343 atoms) and shapes (spherical and cubic-shaped) are discussed. Comparison with PbSe and PbS clusters will be made where it is relevant. The energetic studies of various impurities in PbTe clusters have been carried out to see if there is "self-purification" [146, 147] (also see the discussion in Sec. 4.1). The impurities under consideration are Na, K (monovalent), Cd (divalent), Ga, In, and Tl (trivalent) which have been studied in the previous sections dealing with bulk and thin films. We will see how the HDS and DDS associated with the group III (Ga, In, Tl) impurities look like in the cluster geometry.

4.5.1 Structural Relaxation

In order to study the effects of surface relaxation on the structural properties of PbTe clusters, two classes of cubic-shaped clusters, stoichiometric and non-stoichiometric, are considered. Both classes are constructed as cubes of size $(Na/2)(1 \times 1 \times 1)$ cut from the bulk, where the stoichiometric clusters take N=1, 3, 5,... and the non-stoichiometric ones take N=2, 4, 6,...; a=6.55 Å is the calculated bulk lattice constant. Compositions of these stoichiometric and non-stoichiometric clusters are Pb_nTe_n and $Pb_{n+1}Te_n$, respectively. All the surfaces are (001) type. In a supercell model, the clusters from the neighboring supercells were separated by a vacuum of ~10 Å in thickness. All atoms were allowed to relax to their minimum energy positions.

In Figs. 4.18(a)-(c), the structures of several Pb_nTe_n clusters (n=4, 32, 108) after structural relaxation are shown. We start with Pb_4Te_4, the tetramer of PbTe, which is the smallest cluster under investigation. The relaxed structure of Pb_4Te_4 is a distorted cube [see Fig. 4.18(a)]. Let the Te-Pb-Te angle be denoted as α and the Pb-Te-Pb angle as β, which are both equal to 90° in the unrelaxed structure. In the relaxed structure of Pb_4Te_4, α=96.1° and β=83.6°. The deviation of α and β from the right angle is quite large, ~7%. This is a result of the asymmetric surface relaxation of the cation and anion atoms as discussed earlier in the case of the PbTe(001) thin films. The Pb-Te bondlength is also reduced considerably, by ~6.8%. Similar results are found for Pb_4Se_4 (a=6.20 Å) and Pb_4S_4 (a=5.99 Å). The reduction in the Pb-Se (Pb-S) bondlength is 8.1% (9.1%); and the deviation of α and β from the right angle is ~4% (for Pb_4Se_4) or 1.6% (for Pb_4S_4). This indicates that the distortion of the relaxed structure of Pb_4Q_4 decreases in going from Q=Te to Se to S. This reflects the fact that the ionicity of the Pb-Q bonds increases in going from Q=Te to Se to S. The surface relaxation is smaller (and, therefore, the cube is less distorted) in a system where the cation-anion bonds are more ionic.

For larger Pb_nTe_n clusters (n=32, 108), there seems to be tertramerization. The

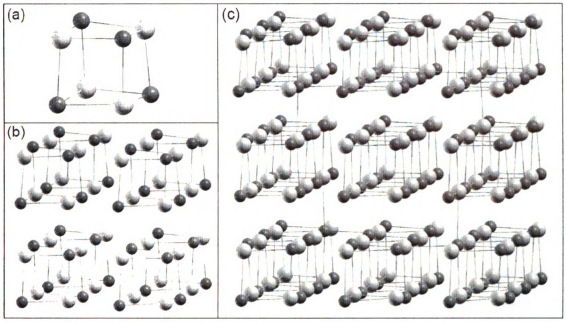

Figure 4.18: Relaxed structures of the stoichiometric Pb_nTe_n clusters: (a) n=4, (b) n=32, and (c) n=108). Large balls are for Pb, small balls are for Te.

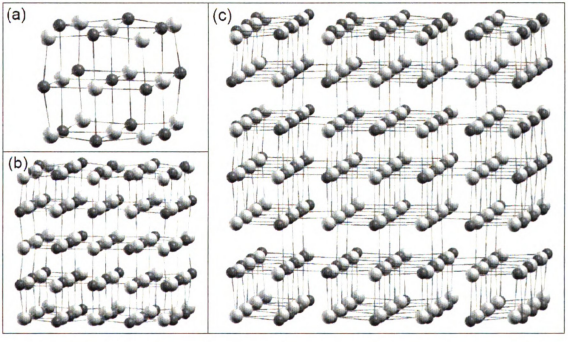

Figure 4.19: Relaxed structures of the non-stoichiometric $Pb_{n+1}Te_n$ clusters: (a) n=13, (b) n=62, and (c) n=171). Large balls are for Pb, small balls are for Te.

original cubes tend to split into tetramers (Pb_4Te_4) which are the distorted cubes with the eight atoms connected in Figs. 4.18(b) and 4.18(c). The inter-tetramer bondlengths are larger than the intra-tetramer ones by ~5-10%, where the differences are larger for the outer bonds and decrease towards the center of the cluster. The distortion of the tetramers is also larger for those near the surface. In the cluster with n=108 [see Fig. 4.18(c)], the deviation of α and β from the right angle in the tretramer at one of the corners of the cluster is ~7.5%, whereas in the central tetramer it is ~5%. Without going to larger cluster sizes and just based on what has been learned about the surface relaxation in the PbTe(001) surface from the previous sections, one can now state that the atoms which are near the surfaces of the Pb_nTe_n nanoclusters tend to tetramerize (i.e., split into tetramers of PbTe) whereas those far away from the surfaces preserve their bulk symmetry. Similar asymmetric relaxation is observed with the non-stoichiometric $Pb_{n+1}Te_n$ clusters (n=13, 62, 171) which are, however, geometrically much more symmetric [see Figs. 4.19(a)-(c)] than the Pb_nTe_n clusters.

4.5.2 Energetics

Besides the cubic-shaped clusters, spherical clusters of PbTe have also been constructed. These are built by considering all the bulk Pb and Te atoms contained in a sphere (centered on the Pb-Te bond). These spherical clusters are, therefore, stoichiometric with the same numbers of Pb and Te atoms; the composition is Pb_nTe_n. Such spherical have been studied previously for CdSe systems [147]. In Fig. 4.20, I plot the total energies (per PbTe pair) of different spherical and cubic-shaped stoichiometric Pb_nTe_n clusters (relative to the bulk PbTe energy) with and without relaxation as a function of the cluster size. The energies decrease as one increases the cluster size. As one increases the cluster size further, the energies should reach the bulk energy (the zero level in Fig. 4.20). As can be seen clearly from the figure, the cubic-shaped clusters are lower in energy than the spherical ones. For n=108, the energy difference

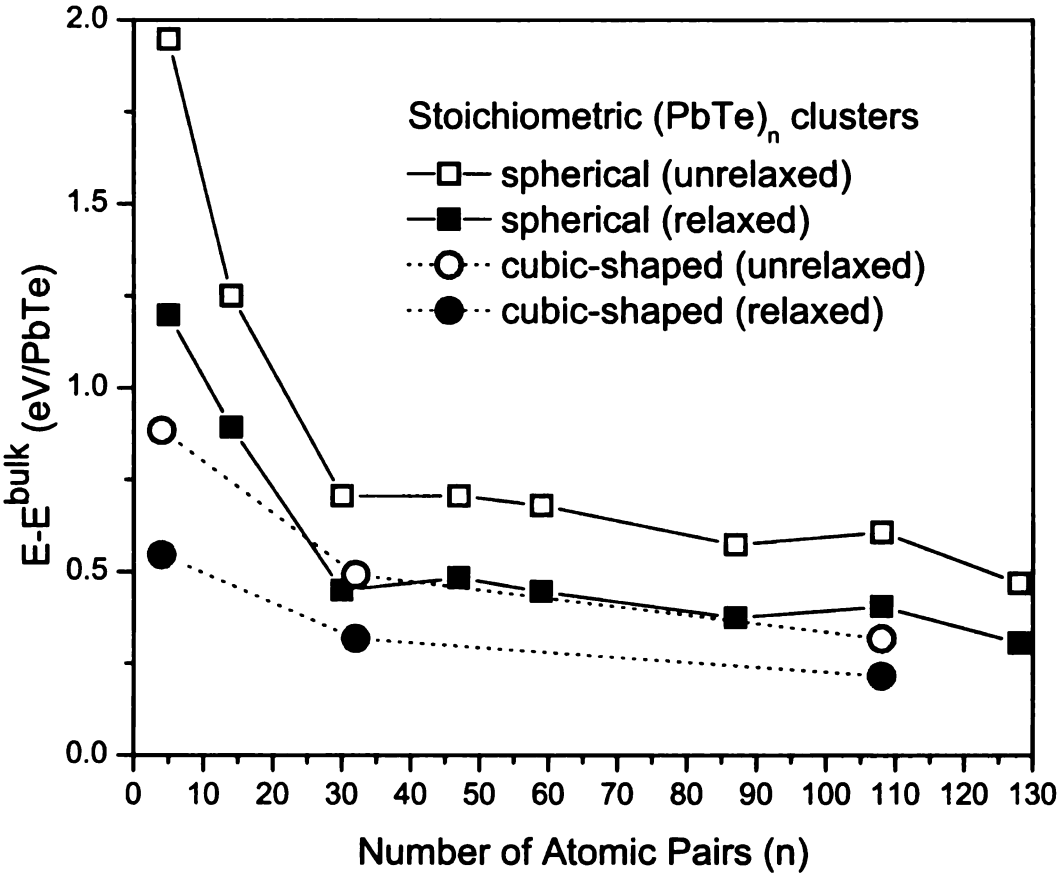

Figure 4.20: Total energy of the stoichiometric Pb_nTe_n clusters, with respect to the bulk PbTe energy, as a function of cluster size. SOI was not included.

is ~0.189 eV/PbTe; the energy difference is much larger in smaller clusters. This suggests that the cubic-shaped Pb_nTe_n clusters with the (001) surface are relatively more stable energetically, which is consistent with the observation of nanoscale PbTe cubes in experiments [123].

The relaxation energy, which is the difference between the "relaxed" and "unrelaxed" curves in Fig. 4.20, also decreases as the cluster size increases. The relaxation energy (per PbTe) goes from 0.750 eV (n=5) to 0.163 eV (n=128) for the spherical clusters, whereas for the cubic clusters, it goes from 0.339 eV (n=4) to 0.101 eV (n=108). The change in the relaxation energy with increasing n for a given type of cluster results from the change in the ratio of the number of atoms on and near the surface to the number of atoms inside the cluster. The relaxation energies in the cubic-shaped clusters are smaller than in the spherical ones because the latter usually

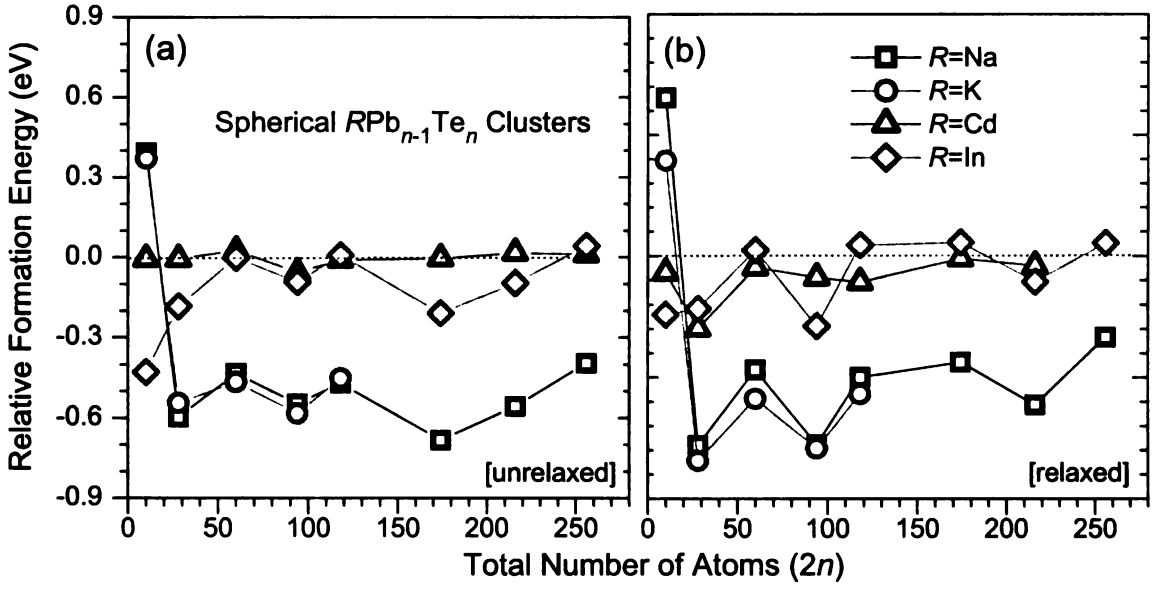

Figure 4.21: Relative formation energies of various impurities (R) in the spherical $R\mathrm{Pb}_{n-1}\mathrm{Te}_n$ clusters as a function of cluster size. SOI was not included.

have atoms on the surface which are loosely bound to the rest of the cluster.

Defect formation energy.—In order to to see how the defect formation energy depends on the cluster size, different systems were doped with several impurities, R=Na and K (monovalent), Cd (divalent), and In (trivalent). We start with spherical clusters $R\mathrm{Pb}_{n-1}\mathrm{Te}_n$ where the impurity R replaces the Pb atom closest to the center of the clusters. The defect formation energy $E_f^{cluster}$ is calculated according to Eq. (4.4). In Figs. 4.21(a) and 4.21(b), the formation energies of the impurities without and with relaxation, measured with respect to their formation energies in bulk PbTe, $\Delta E_f = E_f^{cluster} - E_f^{bulk}$ (called as the relative formation energies, RFE) are given. Excepting for very small clusters, one finds that RFE<0, i.e., defects prefer to go into the clusters compared to the bulk. A general feature of RFE is oscillatory n-dependence with an average increase with n, approaching 0 (as it must as $n \to \infty$). The monovalent defects (Na and K) have RFE lower by ~0.5 eV compared to the divalent (Cd) and trivalent (In). The difference between Na, K, Cd, and In in the spherical $R\mathrm{Pb}_{n-1}\mathrm{Te}_n$ clusters can be understood in terms of the difference between

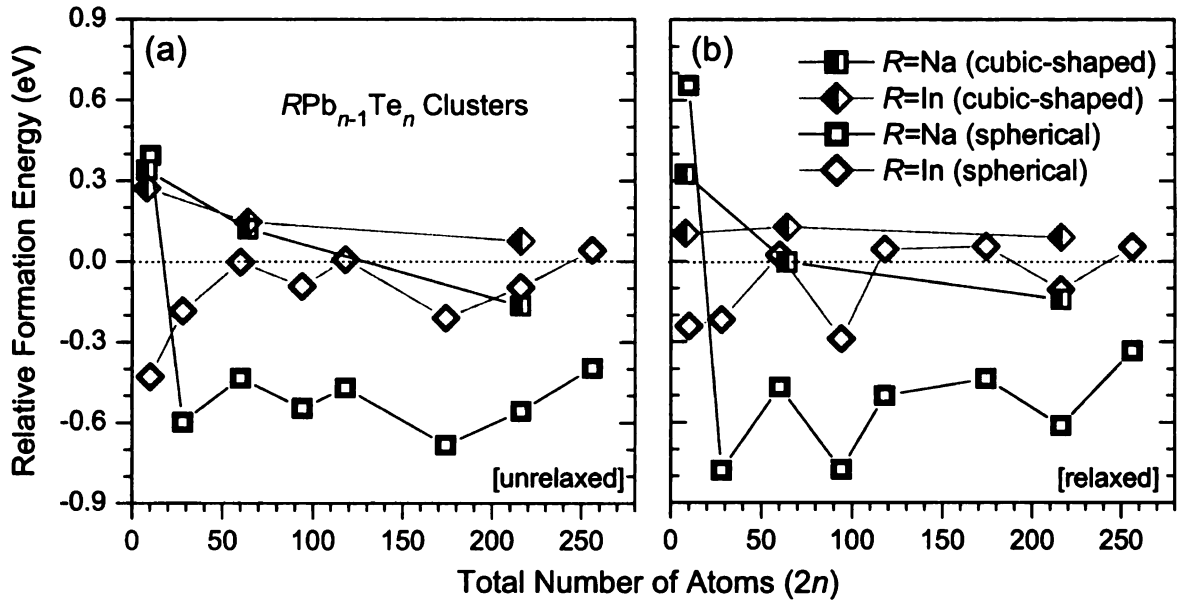

Figure 4.22: Relative formation energies of various impurities (R) in the cubic-shaped and spherical $R\mathrm{Pb}_{n-1}\mathrm{Te}_n$ clusters as a function of cluster size. SOI was not included.

the valences of the host and the impurity atoms. These results also suggest that it may be easier for the impurities to be put into PbTe clusters than into the bulk. Especially, Na and K can readily enter PbTe nanocrystals because of their large negative formation energies.

To see how the formation energy depends on the shape of the clusters, Figs. 4.22(a) and 4.22(b) give the relative formation energies of R=Na and In in the cubic and spherical $R\mathrm{Pb}_{n-1}\mathrm{Te}_n$ clusters as a function of the cluster size. For both the impurities, the formation energy in the clusters is higher than in the bulk at small sizes and decreases as increasing n, except for that of In at n=5 due to strong relaxation effect. For n=108, the formation energy of In is still above the bulk value (at 0 eV), whereas that of Na is below the bulk value.

To summarize, the results for spherical PbTe clusters (up to 256 atoms) are in disagreement with the results of Dalpian and Chelikowsky [147] for spherical CdSe clusters (up to 293 atoms) doped with Mn. They reported that the formation energy of defects in CdSe nanocrystals increased as the size of the nanocrystals decreased,

thereby explaining why it was difficult to dope nanocrystals. In contrast, I find that Na in spherical PbTe clusters shows a negative formation energy excepting for very small clusters. For In, the formation energy varies around its bulk value (RFE$\approx$0) but slightly below. For the cubic-shaped clusters, I do observe that the relative formation energy decreases with increasing cluster size, but it is close to the bulk value. The formation energy is even smaller than than bulk value for Na in the cluster with n=108. One, therefore, can not say with certainty about a general trend for the relative formation energy in the cubic-shaped PbTe clusters without further studies of larger clusters. The situation is also similar for the spherical clusters where the relative formation energy might reach the bulk value (the zero level) or cross the zero level for certain n, and then decreases with n and approaches the bulk value at very large cluster size. It is also noted that the largest size of the clusters in the present studies (also in Dalpian and Chelikowsky's), is $\sim$ 2.6 nm, still much smaller than that in experiments (5-20 nm).

4.5.3 Electronic Structure

Electronic structure of unopded PbTe nanoclusters.—Figs. 4.23(a) and 4.23(b) give the total density of states (DOS) of the cubic-shaped Pb_nTe_n (n=108; $\sim$1.6 nm in size) obtained in the absence of SOI. The overall DOS of the cluster resembles very well that of the bulk. However, the energy difference between the highest occupied molecular orbital (HOMO) and the lowest unoccupied molecular orbital (LUMO) is $\sim$1.22 eV, much larger than the band gap of bulk PbTe (of $\sim$0.8 eV), as expected, because it is well known that quantum confinement effects shift the valence-band maximum down to lower energies and the conduction-band minimum to high energies [187]. In order to see the nature of the HOMO and LUMO, I show in Fig. 4.24 their corresponding charge densities. As seen from the figure, the HOMO is predominantly associated with Te atoms which are at the corners of the cubic cluster (see the upper picture Fig. 4.24).

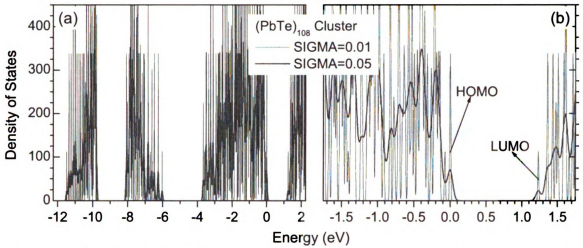

Figure 4.23: (a) DOS of the stoichiometric Pb_nTe_n (n=108) cluster and (b) the blowup of the DOS showing the highest occupied molecular orbital (HOMO) and the lowest unoccupied molecular orbital (LUMO). The states have been Gaussian broadened by SIGMA=0.01 eV or 0.05 eV. SOI was not included; the zero of the energy is set to the highest occupied level.

It is, therefore, the surface state(s) of the cluster. These states are associated with the unbonded states of the corner Te atoms. The LUMO, on the other hand, consists of predominantly Pb atoms, which are in the middle of the cluster (see the lower picture of Fig. 4.24).

Electronic structure of the group III doped PbTe nanoclusters.—As discussed earlier, the group III (Ga, In, Tl) impurities show extremely interesting features in bulk and films of PbTe. In order to see how robust the defect states are in different geometries, I have studied PbTe nanoclusters doped with group III (Ga, In, Tl) substitutional impurities. The impurity atom was introduced at the Pb site in the middle of the cluster. Figs. 4.25(a)-4.25(c) give the DOS of the PbTe cluster doped with Ga, In, and Tl, respectively. There are serval defect states, one in the band gap region and the other $\sim$ 5 eV below the former. These two states can be easily identified as DDS and HDS, respectively, as in bulk PbTe and PbTe films. In going from the bulk to the cluster, the HDS-DDS distance increases in the case of Ga ($\sim$ 5.5%) and In ($\sim$ 2.0%) and decreases by $\sim$ 2.3% in the case of Tl. This indicates that HDS and DDS are extremely robust. The DDS lies above the surface state(s) for all the three

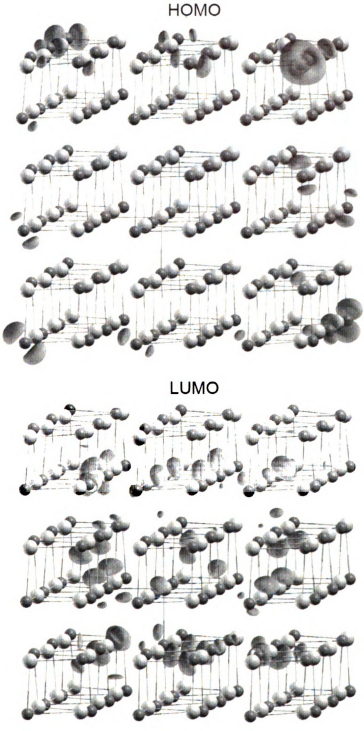

Figure 4.24: The highest occupied molecular orbital (HOMO; upper picture) and the lowest unoccupied molecular orbital (LUMO; lower picture) of the stoichiometric $Pb_{n+1}Te_n$ (n=108) cluster. Large balls are for Pb, small balls are for Te.

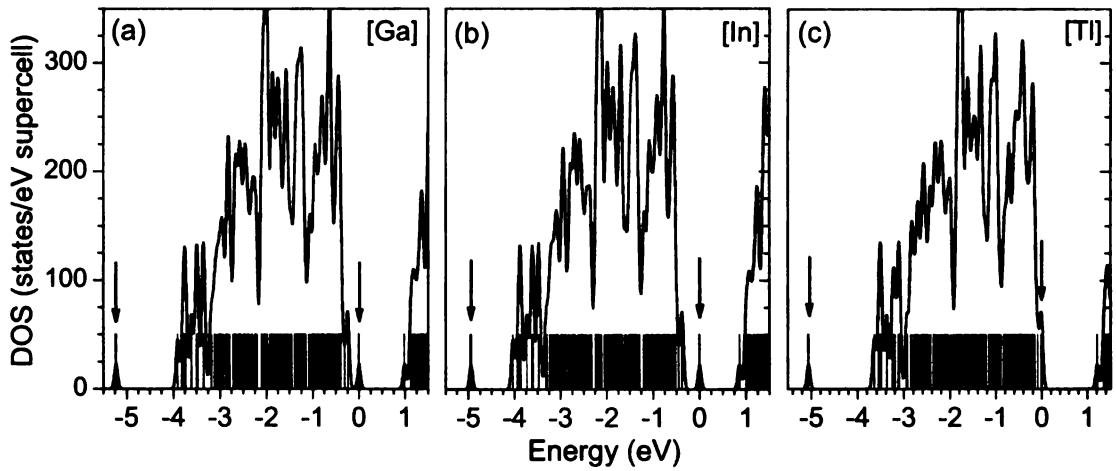

Figure 4.25: DOS of the 216-atom cubic-shaped PbTe nanocluster doped with (a) Ga, (b) In, and (c) Tl substitutional impurities. The states have been Gaussian broadened by 0.05 eV. HDS and DDS are marked by arrows. The dashes are the eigenvalues of the cluster. Spin-orbit interaction (SOI) was not included. The zero of the energy is set to the highest occupied level.

impurities, but in the case of Tl they are very close.

4.6 Summary

In summary, I have presented in this chapter the results of studies of pure PbTe(001) films and surfaces with larger supercells and in more detail compared to earlier studies. My results agree qualitatively with these earlier studies [149, 150] but are in excellent agreement with experiment [160]. There is no lateral relaxation of Pb and Te atoms, but a damped oscillatory relaxation along the z direction (perpendicular to the surface). Surface energy of PbTe(001) is found to be $\sim$0.21 eV per surface Pb-Te pair; work function is $\sim$4.6-4.7 eV, in excellent agreement with the experimental value (4.5$\pm$0.3 eV) [164]. There are surface states near the top of the Te 5s band and indications of surface resonance states near the top of the valence band and the bottom of the conduction band that were identified previously by Ma *et al.* [150]. The structural relaxation in PbTe nanoclusters with the (001) surfaces can be understood in terms of the observed surface relaxation.

The defect states associated with different substitutional impurities and native defects that were found in PbTe bulk are preserved in the film geometry. HDS and DDS have been identified in group III (Ga, In, and Tl) doped PbTe films, similar to those in PbTe bulk. As one goes from the bulk to subsurface to surface layers, the localized band formed by the HDS gets narrower and moves towards the bottom of the valence band, and exhibits a crossover from 3D to 2D band structure due to the change in the impurity-impurity interaction along the z direction in the supercell models. The DDS associated with the group III impurities in the first and the second layer of a 9-layer (2×2) slab tends to be shifted upwards (towards the conduction-band bottom) compared to that in the third layer. The partial charge density analysis shows that HDS and DDS are the bonding and anti-bonding states of In $5s$ and its neighboring Te $5p$. The defect states associated with various monovalent (Ag, Na, and K), divalent (Cd and Zn), other trivalent (Sb and Bi) impurities, and Pb and Te vacancies also get modified as one goes from the bulk to films, and from one layer to another. Anomalies are usually found in connection with the defects in the first and the second layer of the slab due to the special local environment of the defects, resulting from surface relaxation. These modifications in the defect states, which usually occur in the neighborhood of the band gap, should have an impact on the properties of the systems. However one expects that some of their main characteristics will be preserved in the films. Both the HDS and DDS preserve their characteristic features in PbTe (nano)clusters.

Energetic studies of different substitutional impurities and native defects embedded in bulk PbTe and in different layers of PbTe films have shown different energy landscapes, depending on the nature of the defects. Formation energies of most of the defects vary non-monotonically in going from the surface to the bulk. This has important implications in doping mechanism in PbTe-bulk and nanostructures, and the equilibrium distribution of the defects in these systems. Some defects can be

annealed out to the surface, whereas some others can be trapped in the subsurface layers. The formation energy of the impurities in a PbTe cluster depends on the size and shape of the cluster and can be either smaller or larger than that in the bulk depending on the type of impurity (monovalent, divalent, or trivalent). These results are in disagreement with recent reports on Mn defects in CdSe nanocrystals [147].

Chapter 5

Energetics of Defect Clustering and Impurity Bands: Symmetry Breaking, Band Splittings, and Hybridization

Although DOS gives a broad general picture of the defect states in semiconductors, one needs to study the detailed features of the impurity bands to have a deeper physical understanding. Results of comprehensive studies of the impurity bands associated with various defects and impurities in PbTe, SnTe, and GeTe are presented in this chapter. I discuss how different impurity related properties of these systems can be understood in terms of the calculated band structures. I also look at the defect clustering and possible off-centering of the atoms in these systems.

5.1 Introduction

Most of the studies of defect states in PbTe have been so far based on the single-particle density of states (DOS) [141, 41, 142, 143, 144, 145, 151] including the results

presented in Chapter 4. Mahanti and Bilc [141], however, have reported the band structure of PbTe doped with Ag and Sb impurities, and Hase and Yanagisawa[145] have discussed some on the band structure of the compound $Tl_\delta Pb_{1-\delta}Te$ (δ=0.125). Impurity levels associated with Pb and Te vacancies in PbTe have been studied by Parada and Pratt [136] using a Slater-Koster model and Wannier function basis constructed out of a finite number of PbTe bands, and then by Hemstreet [138] using the XSW-cluster method. However, to the best of my knowledge, no one has presented complete band structures showing the vacancy-induced bands obtained in *ab initio* electronic structure calculations. In fact, a band structure can provide us with more information on the electronic structure, especially on the "impurity bands"(i.e., the energy bands associated with the impurity or defect in the system) and their formation. Band structure is extremely helpful in understanding the transport properties of a system.

Although the nature of the defect states associated with different defects and impurities has been carefully studied in the previous chapter, there are still some issues that need to be cleared up. One is about the group III impurities in PbTe where the impurity levels were not well defined because of their overlap with the valence and/or conduction bands. The other is about the PbTe, SnTe, and GeTe-based thermoelectric materials. Investigations of different defects and impurities in these systems have provided us with a general understanding of the nature of the defect states which has helped us suggest possible candidates for good thermoelectrics. However, the relationship between the transport properties of a system and its electronic structure is more subtle and a detailed band structure is needed in order to have a better understanding of the transport properties of the system. A general theory of defect states in narrow band-gap semiconductors is also extremely helpful in searching for novel materials with desired properties.

In this chapter, I present the results of comprehensive studies of the impurity bands

associated with various defects and impurities in PbTe, SnTe, and GeTe. I discuss how the properties of these systems can be understood in terms of the calculated band structures, in particular those features which are sensitive to the impurities. I have also looked at defect clustering and possible off-centering of the atoms in these systems using *ab initio* energy calculations which goes beyond the simple ionic model. The arrangements of this chapter is as the following. In Sec. 5.2 supercell models with two impurity atoms are introduced, these will be used to study the defect clustering, off-centering (presented in Sec. 5.3), and impurity-impurity interaction in various systems. Impurity bands associated with different defect atoms in PbTe, SnTe, and GeTe are presented in Sec. 5.4 and 5.5. In Sec. 5.6 vacancy-induced bands in PbTe, SnTe and GeTe are discussed. I conclude this chapter with a brief summary in Sec. 5.7.

5.2 Modeling of Defects

Besides the (2×2×2) supercell model with a single impurity (or native point defect) that has been used in previous chapters, the same (2×2×2) supercell is used to investigate the properties of an impurity pair (R,R'); see Fig. 5.1. The composition of this supercell is then $RR'\mathrm{M}_m\mathrm{Te}_{m+2}$ (m=30), where M={Pb, Sn, Ge} and R and R' are the impurity atoms. The two impurity atoms are either the first, the second, the third, the fourth, or the fifth nearest neighbors (n.n.) of one another with the impurity-impurity distance equal to $a/2$, a, $a\sqrt{3/2}$, $a\sqrt{2}$, and $a\sqrt{3}$, respectively, where a is the undoped bulk lattice constant; a=6.55 Å (for PbTe), 6.40 Å (SnTe), and 6.02 Å (GeTe).[1] This model has been used by Bilc *et al.* [41] and then by Hazama *et al.* [142] both for (R,R')=(Ag,Sb). The configuration where R and R' are the second n.n. is also called the "Ag-Sb chain" model in Bilc *et al.*'s work.

[1]The experimental value of the lattice constants of SnTe and GeTe are 6.327 Å and 5.996 Å, respectively; see Ref. [60].

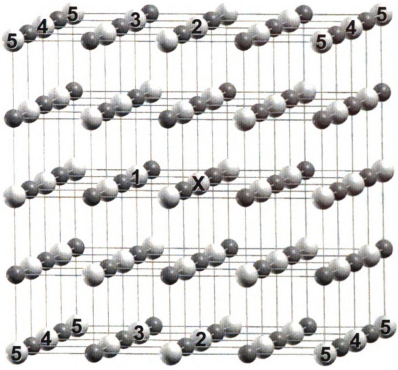

Figure 5.1: The (2×2×2) supercell with an impurity pair (R,R'). Large balls are for the cations, small balls are for the anions. R is at the center of the cell (marked by the cross) and R' is either the first ("1"), the second ("2"), the third ("3"), the fourth ("4"), or the fifth ("5") nearest neighbor of R.

In this chapter, I will focus primarily on the group III impurities (Ga, In, Tl) impurities. Some other dopants which are usually found PbTe-, SnTe-, and GeTe-based thermoelectric materials will also be discussed. Structural optimization, total energy and electronic structure calculations were performed in VASP [57] (see the previous chapters for the computational details). All the atomic coordinates were relaxed; SOI was included in the calculations to obtain band structures, unless otherwise noticed.

5.3 Defect Clustering and Off-Centering in Bulk Thermoelectrics

In order to see how the impurity atoms arrange themselves in a host material, the formation energy of different impurity pairs was calculated as a function of the pair

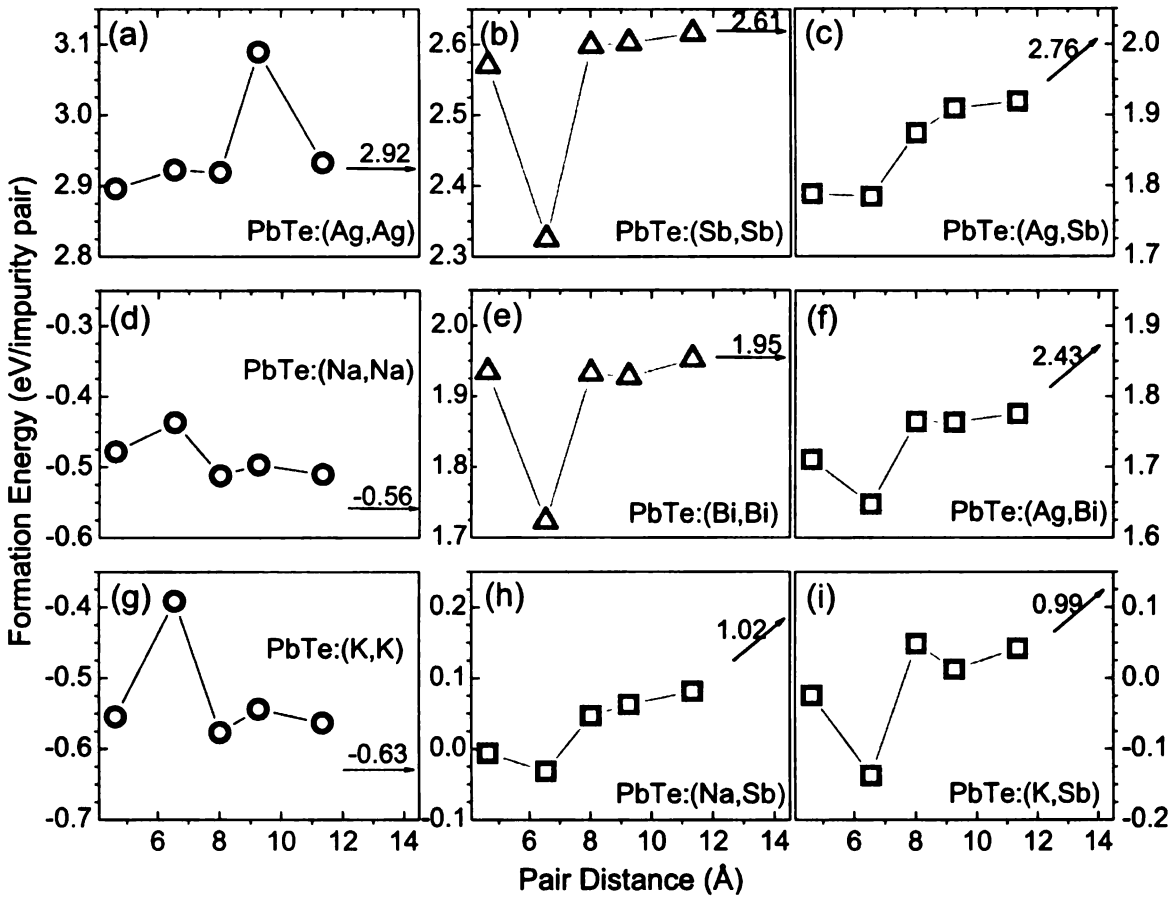

Figure 5.2: Formation energies of various impurity pairs in PbTe as a function of pair distance. The results were obtained in calculations using (2×2×2) supercells; spin-orbit interaction (SOI) was not included. The values given with the arrows are the formation energies of the pairs at infinitely large pair distance.

distance. The formation energy E_f of an impurity pair (R,R') is defined as [142]

$$E_f = E(RR'\mathrm{M}_m\mathrm{Te}_{m+2}) - E(\mathrm{M}_{m+2}\mathrm{Te}_{m+2}) + 2\mu_{\mathrm{M}} - (\mu_R + \mu_{R'}), \qquad (5.1)$$

where E is the total energy of the system and μ is the chemical potential of the constituent elements. The latter is calculated as the total energy per atom in each standard metallic state. The formation energies for single defects have been discussed in Chapter 4.

Defect clustering.—Figs. 5.2(a)-(i) give plots of the formation energy of (R,R')=(Ag, Ag), (Sb,Sb), (Ag,Sb), (Bi,Bi), (Ag,Bi), (Na,Na), (Na,Sb), (K,K), and (K,Sb) in PbTe as a function of the pair distance. The formation energies of the pairs at infinitely

large pair distance are also given (the values given with the arrows in the figures). Different impurity atoms behave quite differently. While Ag atoms tend to come close to each other [E_f is low for small pair distances; see Fig. 5.2(a)], Na (and K) atoms tend to repel each other [E_f is low for large pair distances; see Figs. 5.2(d) and 5.2(g)]. Just as in the single defect case (see Table 4.3), the formation energies of (Na,Na) and (K,K) pairs are negative suggesting that they readily come into the Pb sites in PbTe. On the other hand, E_f for (Ag,Ag) pairs is positive. The energy landscape of the (Sb,Sb) pair is similar to that of (Bi,Bi); the latter, however, has lower E_f than the former because Bi is more compatible with Pb in size and electronic structure which make Bi atoms easier to go into the Pb sites. In contrast to the monovalent case, the trivalent impurity pairs of Sb and Bi show completely different behavior. There is a large drop in E_f at the second n.n. distance. This can be explained in terms of the highly directional interaction between the p states of the trivalent atoms through hybridization with Te p which tends to form 1D bands along the Te-Sb(Bi)-Te chains. This effect is also apparent for pairs made from one monovalent and trivalent atoms, they all have a minimum in E_f at the second n.n. distance [Figs. 5.2(c), 5.2(f), 5.2(h), and 5.2(i)]. The first n.n. distance also gives a smaller E_f compared to other distances. In fact, for the (Ag,Sb) pair, E_f for the first and the second n.n. distances are comparable. It is also observed that the system gains energy (up to $\sim$1 eV) when simultaneously doped with one monovalent and one trivalent atom. To summarize, formation energy calculations show that many impurity atoms in PbTe tend to come close to each other and form clusters or some kind of nanostructures. This is consistent with experiments where nanostructuring has been found in $AgPb_mSbTe_{2+m}$ [15, 17], $Ag_{1-x}Pb_mBiTe_{2+m}$ [112], $Na_{1-x}Pb_mSb_yTe_{m+2}$ [19], and $K_{1-x}Pb_{m+\delta}Sb_{1+\gamma}Te_{2+m}$ [20] systems.

For SnTe and GeTe, I have looked at different pairs made of only the monovalent Ag and trivalent Sb and Bi. The formation energy of (Ag,Ag) in SnTe and in GeTe

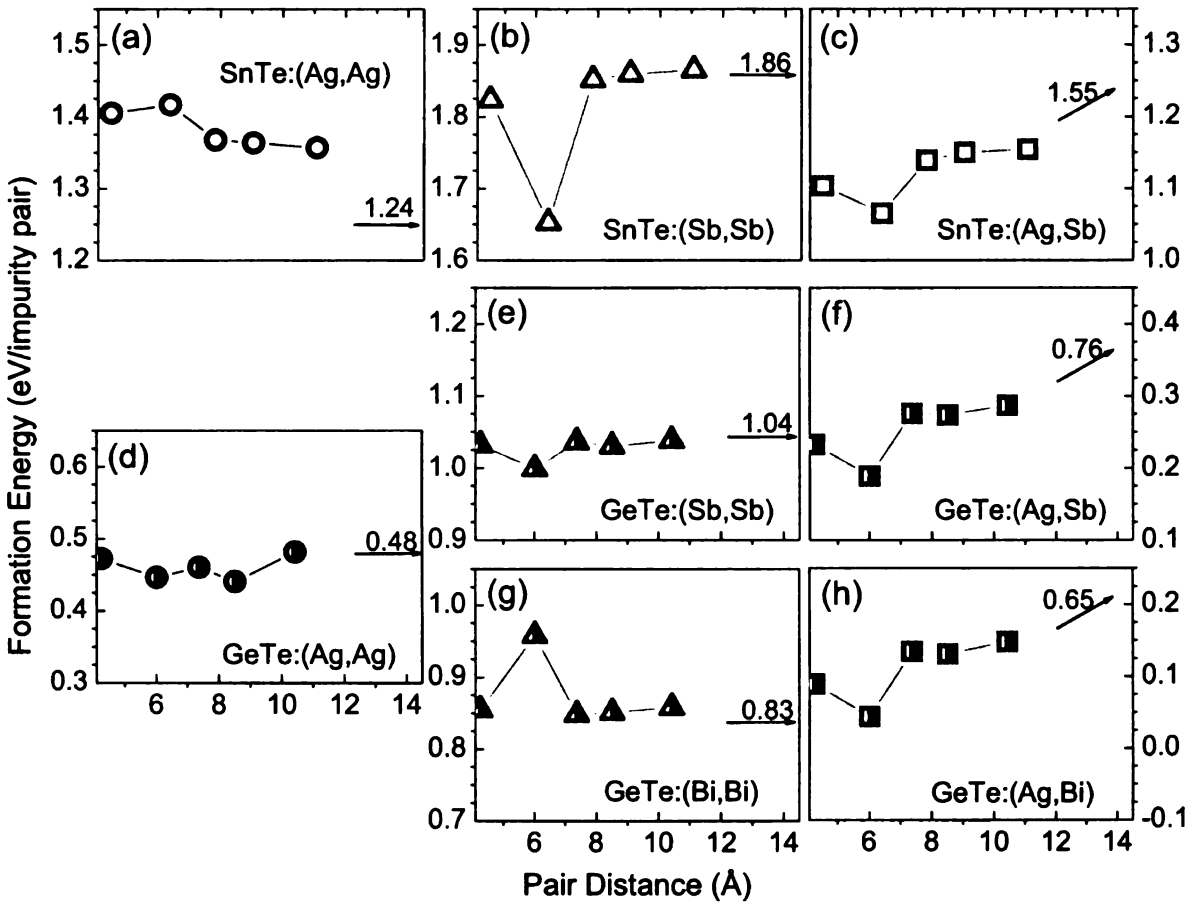

Figure 5.3: Formation energy of various impurity pairs in PbTe as a function of pair distance. The results were obtained in calculations using (2×2×2) supercells; spin-orbit interaction (SOI) was not included. The values given with the arrows are the formation energies of the pairs at infinitely large pair distance.

does not change much as one varies the pair distance, although the Ag atoms in SnTe tend to repel each other [see Fig. 5.3(a)] and show shallow minima in GeTe [see Fig. 5.3(d)]. The (Sb,Sb) pair in SnTe, on the other hand, has a large drop in E_f at the second n.n. distance [Fig. 5.3(b)], similar to what has been seen in PbTe. The minimum of E_f at the second n.n. distance of the (Sb,Sb) in GeTe is much less pronounced [Fig. 5.3(e)]. The formation energy of (Bi,Bi) in GeTe, on the other hand, has the maximum at the second n.n. distance [Fig. 5.3(g)]. Although the energy landscape of different pairs made from two atoms of the same element can be very different, any combination of one monovalent and one trivalent again has the lowest E_f at the second n.n. distance [Figs. 5.3(c), 5.3(f), and 5.3(h)].

This seems to be a generic feature of simultaneous doping of two impurities which are valence-compensated. However, there are also some differences in the energy landscape of these types of pairs. This should result in different types of clustering or nanostructuring patterns in different hosts. Of course, synthesis conditions should also play an important role since they control the kinetics of the system which is not included in our calculations. Experimentally, nanostructuring has been found in $Ag_{1-x}SnSb_{1+x}Te_3$ [25]. For the GeTe-based systems, in addition to the solid-solution-like distribution of defects [5, 113], microstructure was also observed in some systems [188].

Off-centering caused by defect clustering.—The local structure around an impurity pair can be strongly distorted when the two atoms in the pair are made of one monovalent atom and one trivalent atom when they come closer to each other. There are, however, small local relaxation effects when the defects are far away from each other. We observe that some of the Te atoms which are the neighbors of the (R,R') impurity pair and, sometimes, the impurity atoms themselves go "off-center" (i.e., not on the regular lattice sites). This results in two or more different R-Te and/or

Table 5.1: Different bond lengths (in Å) observed in PbTe simultaneously doped with monovalent and trivalent atoms. The two atoms in a pair are either the 1st, the 2nd, the 3rd, or the 5th n.n. of one another. Only bondlengths which are different by ~0.2 or more in a given configuration are explicitly listed. The Pb-Te bondlength in bulk PbTe is 3.275 Å.

		1st n.n.	2nd n.n.	3rd n.n.	5th n.n.
(Ag,Sb)	Ag-Te	3.07, 3.20, 3.31	3.12, 3.41	-	-
	Sb-Te	2.93, 3.19, 3.44	-	2.96, 3.18, 3.38	-
(Ag,Bi)	Ag-Te	-	3.14, 3.33	-	-
	Bi-Te	3.09, 3.22, 3.33	-	-	-
(Na,Sb)	Na-Te	-	3.26, 3.45	-	-
	Sb-Te	2.93, 3.18, 3.42	-	2.96, 3.18, 3.37	-
(K,Sb)	K-Te	-	-	-	-
	Sb-Te	2.94, 3.18, 3.41	-	-	-

R'-Te bondlengths. This off-centering occurs only when the two atoms in a pair are the first, the second, and/or the third n.n. of one another. Some bondlengths which are different by ~0.2 or larger for a given pair configuration are explicitly listed in Table 5.1. Nearest neighbor (Sb,Sb) pairs are anomalous. Even if the two atoms are the same, there is large off-centering with three different Sb-Te bondlengths; 3.05, 3.22, and 3.35 Å. Off-centering is also found with other impurity pairs and pair configurations in PbTe, SnTe, and GeTe. However, the bondlength differences are considerably smaller (<0.2 Å). These small distortions may not be detected, for instance, in X-ray absorption fine structure (XAFS) analysis [189]. The local bondlength change results from a combination of (i) the difference in the atomic radii of the impurity and the host (Pb, Sn, or Ge) atoms which causes the relaxation of the neighboring Te atoms and (ii) the interaction between p states of the trivalent atoms and Te p. The off-centering observed in PbTe-based systems is expected not to have significant effects on the thermopower but on the electrical and thermal conductivities. The degree of off-centering may also depend sensitively on the lattice constant (pressure). Experimental studies are needed to confirm if there is off-centering and further experimental and theoretical studies are needed to understand the role played by the off-centering in the transport properties in these mixed systems.[2]

5.4 Impurity Bands in PbTe

5.4.1 Band Structure of Undoped PbTe

Before introducing the band structure of PbTe doped with various impurities, I would like to briefly review the band structure of undoped PbTe (fcc structure) focusing on the highest valence band and the lowest conduction band. Since a cubic supercell is used in the impurity studies, one would like to know how the band structure of pure

[2]Note that pair distribution function (PDF) analysis (see, e.g, Ref. [190]) may not be able to detect the off-centering presented here because of the low impurity concentration.

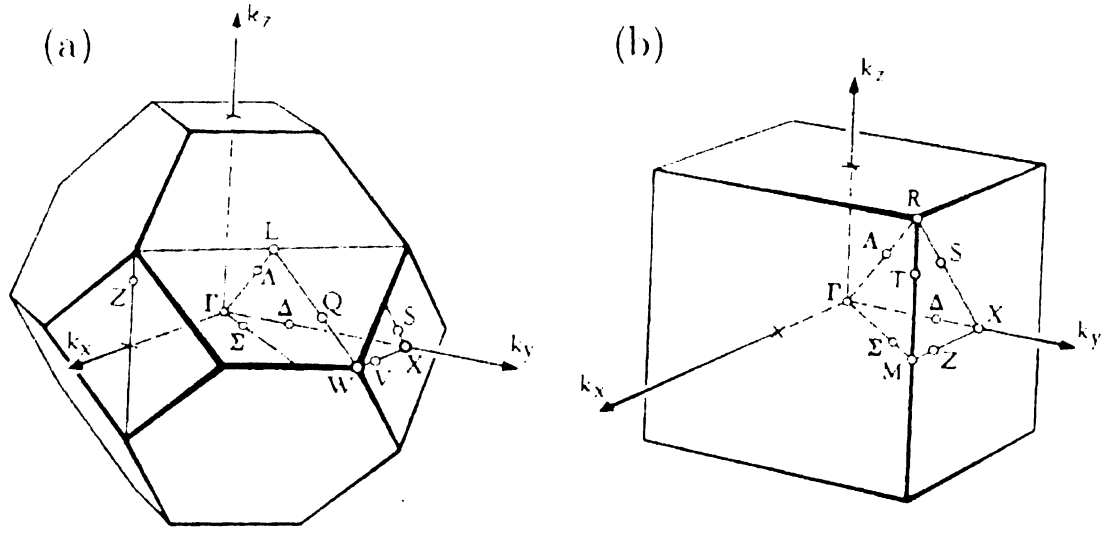

Figure 5.4: (a) Face-centered cubic (fcc) and (b) simple cubic (sc) Brillouin zones; adapted from Ref. [83]

PbTe looks in fcc and cubic Brillouin zone (BZ) schemes [Fig. 5.4(a) and 5.4(b)]. In most of the IV-VI compounds, the valence p states play the dominant role in the formation of the valence and conduction bands. These bands are, respectively, bonding and antibonding states of Pb p and Te p. The edges of the conduction and valence bands are almost symmetric through the Fermi level and both the maximum and the minimum occur at the same point in the $\mathbf{k}$ space. In the fcc BZ corresponding to the primitive cell (2 toms/cell; 1 Pb and 1 Te), the direct band gap is at the L point [see Fig. 5.5(a)]. In the absence of SOI, there is a group of 6 bands (without considering spins) near the band gap at the L point in which three bands (one singlet and one doublet) are above and another three below the Fermi level. We will focus on the two singlets because they form the valence-band maximum (VBM) and the conduction-band minimum (CBM). The splittings between the singlets and the doublets are greater than 0.5 eV.

Brillouin zone mapping.—Since we are going to work mostly with simple cubic (sc) BZ [Fig. 5.4(b)], it is important to see how the band structure of PbTe is mapped onto sc BZs with different lattice parameters. Fig. 5.5(b) shows the band structure of PbTe (8 atoms/cell) along the high symmetry directions of the sc BZ with a=6.55

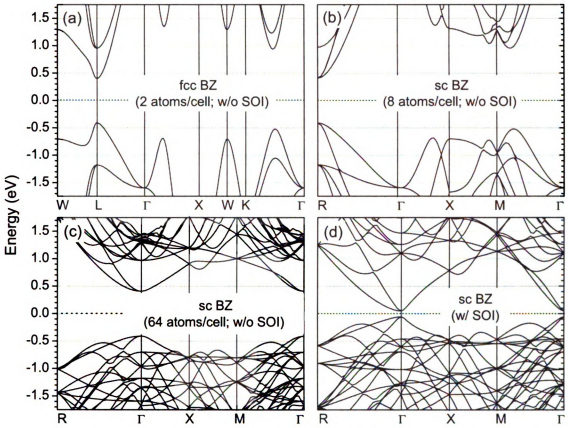

Figure 5.5: Band structure of undoped PbTe in different Brillouin zones: (a) face-centered cubic (fcc) primitive cell (2 atoms/cell; a=6.55 Å), (b) simple cubic unit cell (8 atoms/cell; a=6.55 Å), (c) sc supercell (64 atoms/cell; a=13.1 Å), and (d) simple cubic supercell (64 atoms/cell; a=13.1 Å) with spin-orbit interaction (SOI) included. The Fermi level (at 0 eV) is set to the middle of the band gap.

Å, the same lattice constant used for the fcc case. It is noted that the sc BZ is (25% in volume) smaller than the fcc BZ. The L point in the fcc BZ now becomes the R point in the sc BZ and the band extrema occur at R. In a cubic supercell of PbTe with a=13.1 Å (64 atoms/cell), which is eight times larger than the smaller cubic cell, the corresponding BZ is eight times smaller than that for the sc BZ with a=6.55 Å). The band extrema at the R point (of the large sc BZ) now map onto the Γ point of the small sc BZ. We will make use of this small sc BZ (a=13.1 Å) throughout the chapter when discussing the effects of defects on the band structure of PbTe.

Band degeneracy at CBM and VBM.—There are four inequivalent L points in a fcc BZ. A band which is nondegenerate (disregarding spins) at the L point in the fcc BZ, when mapped into the R (or Γ) point in a sc BZ, becomes fourfold degenerate. This is the case for the CBM and VBM at the R point in the large sc BZ [Fig. 5.5(b)] or at the Γ point in the smaller sc BZ [Fig. 5.5(c)]. In the presence of SOI, the band gap gets reduced significantly (from 0.816 eV to 0.105 eV) [Fig. 5.5(d)] due to large (0.685 eV) lowering in energy of the Pb p bands (dominant near the conduction-band bottom) and smaller (0.026 eV) change in the Te p bands (dominant near the valence-band top). With spin, the CBM (VBM) at the Γ point [Fig. 5.5(d)] has eightfold degeneracy. How the degeneracy at the CBM (VBM), which is eightfold (with spin) or fourfold (without spin), is lifted in the presence of an impurity will be discussed in detail in the following sections.

5.4.2 Understanding the Peculiar Properties of Ga, In, and Tl Impurities

We start with the band structure of In-doped PbTe along the high symmetry directions of the sc BZ obtained with and without atomic relaxation, see Fig. 5.6(a). For simplicity, the results obtained without SOI are shown in this figure. The impurity bands associated with the hyperdeep (HDS) and deep (DDS) defect states are the nearly flat bands, one at ~ -5 eV and the other in the band gap region [Fig. 5.6(a)]. These two bands are denoted as "HDS band" and "DDS band", respectively. The maxima of the bands are at the Γ point, whereas the minima are at the R point. The HDS and DDS bands resemble each other very well except that the bandwidth of the HDS band is smaller due the weaker interaction between the neighboring defect states (the associated defect states are more localized than those with DDS; see Fig. 4.5).

Atomic relaxation affects the position of the HDS and DDS bands.—As can be seen from Fig. 5.6(a), atomic relaxation rigidly shifts the HDS band away from the

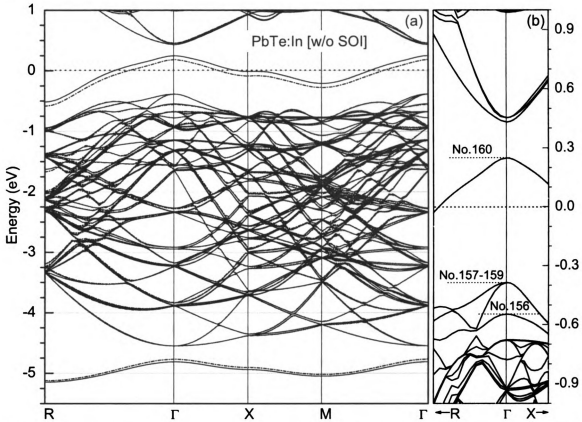

Figure 5.6: (a) Band structures of In-doped PbTe in calculations using relaxed (solid curves) and unrelaxed (dash-dotted curves) structures, and (b) a blowup of the band structure near the Γ point and in the neighborhood of the Fermi level. The Fermi level for the relaxed structure (at 0 eV) is set to the highest occupied states, whereas that for the unrelaxed one it was shifted by −0.180 eV so that the valence bands matched; spin-orbit interaction (SOI) was not included.

valence-band bottom (to lower energy, by ∼24 meV) and the DDS band away from the valence-band top (to higher energy, by ∼74 meV) and leaves the remaining bands almost unaffected. For comparison, atomic relaxation in Ga doped PbTe shifts the HDS and DDS bands in a similar way (i.e. to increase the separation between the two bands) by ∼117 meV and 75 meV, respectively. Atomic relaxation in the case of Tl doped PbTe, on the other hand, reduces the HDS-DDS distance; the DDS band is shifted down towards to valence-band top by ∼27 meV, whereas the HDS toward the valence-band bottom by ∼18 meV. This reflects the fact that after the relaxation the neighboring Te atoms move toward Ga (In) impurity and the Ga-Te

(In-Te) bondlength is decreased by ~2.8% (1.4%), whereas they move away from Tl and the Tl-Te bondlengh is increased by ~1.4%; see Table 4.2.

The removal of band degeneracy in the presence of an impurity and the parentage of the DDS band.—Let us now focus on the region near the Γ point and in the neighborhood of the Fermi level [Fig. 5.6(b)]. The DDS band is denoted as "No. 160", which is the 160th (half-filled) band of all the valence electrons (In $5s^2 5p^1$; Pb $6s^2 6p^2$; Te $5s^2 5p^4$) taken into account in the calculations (other electrons are treated as cores). For the discussions below the twofold spin degeneracy will not be considered. In the undoped case, the VBM and CBM (at the Γ point) are fourfold degenerate [see Fig. 5.5(c)]. The bands from 1-160 are filled with 320 electrons and the conduction band is empty. These 160 bands come primarily from 32 Pb s, 32 Te s, and 96 Te p orbitals (with some hybridization with Pb p which will be ignored). The total number of 320 valence electrons come from 128 Pb $6s^2 6p^2$ and 192 Te $5s^2 5p^4$ electrons. In the presence of the impurity, both the fourfold degenerate bands are split into a nondegenerate band and a threefold degenerate band. The fourfold-degenerate valence band at the Γ point splits into a nondegenerate band (No. 156) and a threefold degenerate band [bands No. 157-159]. The splitting between these two is ~161 meV. A similar splitting is also seen for the CBM, but it is small (~22 meV). Partial charge density analysis shows that band No. 156 at the Γ point is predominantly Te atoms which are the third nearest neighbors (n.n.) of the impurity atom (In), whereas bands No. 157-159 are predominantly second n.n. Te atoms. Also, at the Γ point, the nondegenerate band above the Fermi level (band No. 161) comes from the second n.n. Te atoms with some contribution from Pb, whereas the threefold degenerate band (bands No. 162-163) is predominantly Pb. It is noted that these splittings are present in the absence of local atomic relaxation. They, as it will be shown later, occur with any type of impurity and vacancy, and therefore the results of symmetry breaking (and defect potential) when one replaces a host atom by an impurity or removes the host

atom to make a vacancy.

The band No. 160 is the "impurity band" associated with the DDS discussed in Chapter 4. It is important to point out that this impurity band is split off neither from the top of the valence band nor from the bottom of the conduction band. It is a combination of the impurity s-state and the entire valence band [143]. When In (or Ga, Tl) replaces Pb, one has 319 (=320−4+3) valence electrons in the supercell. The bands 1-159 (which include the HDS) accommodate 318 electrons and the 319th electron occupies the 160th ("impurity") band which is half-filled.

Spin-orbit-induced splittings and hybridization.—It is known from the previous section that SOI has significant effects on the band structure of PbTe, especially on the conduction-band bottom (predominantly Pb p) with large spin-orbit-induced downward dispersion which dramatically reduces the band gap. Since the impurity band comes primarily from (Ga, In, Tl) s and Te p, one does not expect large spin-orbit-induced shift in this band. As a result, one expects hybridization between the conduction band and the impurity band when the conduction bands come down due to SOI. In Figs. 5.7(a)-(f), we show band structures of group III doped PbTe obtained with and without SOI. In the absence of SOI, the impurity band for In lies primarily in the band gap, except near the R point where its minimum lies below the VBM. This is also true for Ga and Tl, except that in these two cases the impurity band lies much closer to the VBM. In the presence of SOI, the conduction band comes down and crosses with the DDS band; there is hybridization between the DDS band and the Pb p bands at and near the Γ point (see the right panel of Fig. 5.7). This hybridization strongly distorts both the DDS band and the conduction band at and near the Γ point. The CBM at the Γ point is now threefold degenerate (sixfold including spins). Partial charge density analysis, however, shows that the CBM is predominantly Pb; there is no indication of the group III impurity atom. The band (which is twofold degenerate) right above the CBM is also predominantly Pb, with very little contribution from the

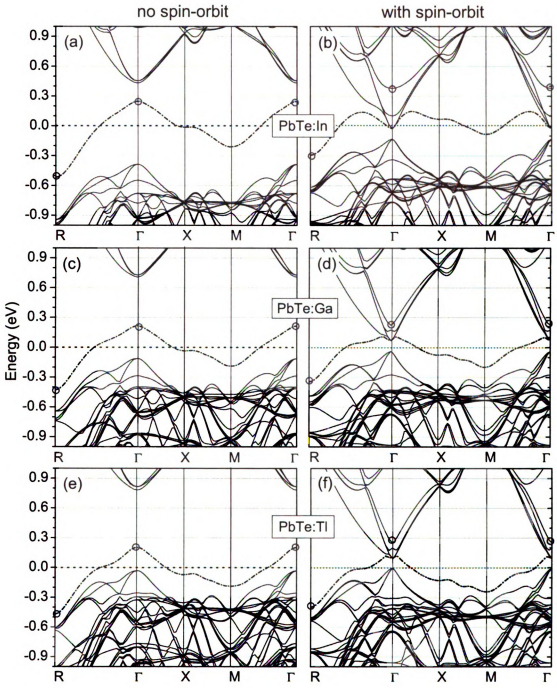

Figure 5.7: Band structures in the simple cubic BZ of PbTe doped with Ga, In, and Tl substitutional impurities in calculations with (the right panel) and without (the left panel) spin-orbit interaction (SOI). The dash-dotted curves are the impurity bands. The Fermi level (at 0 eV) is set to the highest occupied states.

Table 5.2: Character of the HDS and DDS bands in group III doped PbTe obtained in calculations with and without spin-orbit interaction (SOI). Δ is to measure the bandwidth of the HDS and DDS bands limiting by the minima at the R point and the maxima at the Γ point [marked by circles in Fig. 5.7(a)-(f)]. In the case of DDS with SOI, Δ is measured from the minimum at the R point to the minimum of the band which has In character at the Γ point (also marked by circles in the figures); see the text. All these quantities are measured in electronvolt (eV).

	Ga		In		Tl	
Band	Position	Δ	Position	Δ	Position	Δ
HDS	-5.2099 (R)	0.2658	-5.1472 (R)	0.3352	-5.4957 (R)	0.3363
(w/o SOI)	-4.9441 (Γ)		-4.8120 (Γ)		-5.1594 (Γ)	
HDS	-5.2460 (R)	0.2784	-5.0345 (R)	0.3445	-5.5145 (R)	0.3475
(w/ SOI)	-4.9676 (Γ)		-4.6900 (Γ)		-5.1670 (Γ)	
DDS	-0.4284 (R)	0.6441	-0.5171 (R)	0.7656	-0.4692 (R)	0.6728
(w/o SOI)	$+0.2157$ (Γ)		$+0.2485$ (Γ)		$+0.2036$ (Γ)	
DDS	-0.3443 (R)	0.5693	-0.2433 (R)	0.6728	-0.3987 (R)	0.6482
(w/ SOI)	$+0.2250$ (Γ)		$+0.3795$ (Γ)		$+0.2495$ (Γ)	

group III impurity. Above this band is another doubly degenerate band (marked by a circle in the figures) which is, however, predominantly group III impurity with some mixing with Te p. This indicates that, although there are spin-orbit-induced band splittings and hybridization, some characters of the impurity band are still preserved at an energy level which is close to the original (i.e., without SOI) level at Γ. It also suggests that the CBM at the Γ point is primarily Pb in nature, as in pure PbTe.

To characterize the HDS and DDS bands and see how they are modified by SOI, we summarize in Table 5.2 the characteristics of the HDS and DDS bands obtained in calculations with and without SOI. Although these bands have s-symmetry, SOI has an indirect effect because they have some Te p character which is affected by SOI. The bandwidth of the HDS band is slightly increased by SOI; by $\sim$4.7% (for Ga), 2.8% (In), and 3.3% (Tl). Both the bandwidth and the change in the bandwidth are monotonic in going from Ga, to In, and Tl. The distance between the DDS band minima (at the R point) to the band minima which preserves the group III impurity

character (at Γ; marked by circles) is also measured and compared with the DDS bandwidth obtained without SOI. The change in the DDS bands are larger because they have more Te p character; by ~11.7% (for Ga), 12.1% (In), and 3.7% (Tl).

Impurity levels.—The zero of the energy (the Fermi level) in the band structures indicates the average position of the impurity bands associated with the DDS. Since DDS is half-filled and the Fermi level is pinned at the middle of the DDS band, the average band position will be identified as the "impurity level". The impurity level associated with In is ~24 meV above the CBM [Fig. 5.7(b)], whereas it is in the band gap region and ~69 meV below the CBM for Ga [Fig. 5.7(d)], and ~5 meV below the VBM for Tl [Fig. 5.7(f)]. Scalar relativistic effects (through the Darwin and mass-velocity terms) have strongest effect on the position of the DDS band in the case of Tl (Z=81). They push the Tl level below the valence-band top. The impurity levels are, however, anomalous in going from Ga (Z=31) to In (Z=49) to Tl. This is probably due to the repulsion between Ga s and Pb s since the Ga s level is closest to the Pb s in energy among the three impurities.[3]

In order to pin down the impurity levels further, the band structures for group III doped PbTe were calculated using a (3×3×3) supercell. This supercell size corresponds to the composition RPb$_{107}$Te$_{108}$ (R=Ga, In, Tl), i.e., 1 at% of the impurity. The DOS for these systems have been discussed in Chapter 4. The cubic BZ is now 27 times smaller than the cubic BZ for the (1×1×1) cubic cell containing 8 atoms. The CBM and VBM are now at the R point [see Figs. 5.8(a')-(c')]. Note that the Γ-R separation for the (3×3×3) supercell BZ is one third the Γ-R separation for the (1×1×1) cell. The impurity bands associated with Ga, In, and Tl in the (3×3×3) supercell BZ are very flat, except near the R point [see Figs. 5.8(a')-(c')]. This is also consistent with the DOS picture obtained in calculations using the same supercell size given earlier [see Figs. 4.6(a)-(c)] where the defect states associated with Ga, In,

[3]These energy levels are: -12.49 (Pb s); -11.55 (Ga s), -10.14 (In s), and -9.83 (Tl s); from the Harrison's *Solid-State Table* [84].

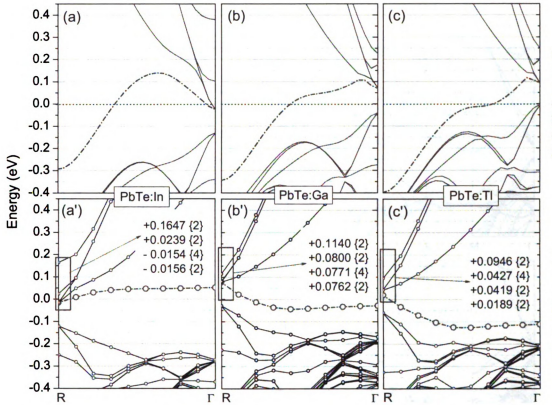

Figure 5.8: Band structure (long the R-Γ direction of the sc BZ) of PbTe doped with R=Ga, In, and Tl. The results were obtained in calculations using two different supercell models: (2×2×2) [figures (a), (b), and (c)] with the composition RPb$_{31}$Te$_{32}$ (a=13.1 Å), and (3×3×3) [figures (a'), (b'), and (c')] with the composition RPb$_{107}$Te$_{108}$ (a=19.65 Å). The energy levels near the CBM are also given with their corresponding degeneracy (including spins) in the curly brackets. SOI was included in all the calculations. The zero of the energy is set to the highest occupied states. Note that this zero level is ill-defined in the results presented in figures (a'), (b'), and (c') because the calculations scanned only a very small part of the BZ.

and Tl were presented by very sharp peaks.

Based on the calculated band structures, I have estimated the impurity level of In to be ∼50 meV above the CBM; for Ga, it is ∼70 meV below the CBM; and for Tl, it is ∼50 meV below the VBM. These results are in qualitative agreement with experiments where it has been reported that the impurity level is 70 meV above the conduction-band bottom (in the case of In), 65-60 meV below the conduction-band bottom (for Ga), and 150-250 meV eV below the top of the light-hole valence band (for Tl) [134]. Although the precise position of the DDS with respect to the band

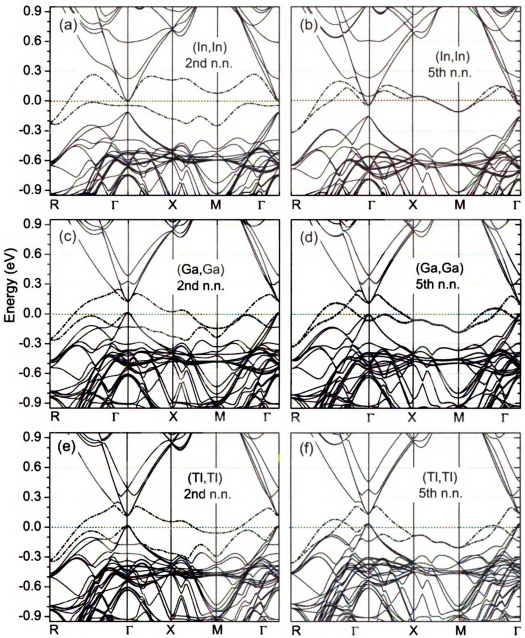

Figure 5.9: Band splittings due to impurity-impurity interaction in group III-doped PbTe. The results were obtained in calculations using the (2×2×2) supercell with a impurity pair: (In,In) [in (a) and (b)], (Ga,Ga) [in (c) and (d)], and (Tl,Tl) [in (e) and (f)]. The two impurity atoms in a pair are either the second (2nd n.n.) or the fifth (5th n.n.) nearest neighbors of one another. The dash-dotted curves are the impurity bands. SOI was included and the Fermi level (at 0 eV) is set to the highest occupied states.

edges might not be given accurately by the standard DFT due to the "band gap problem" [23], its general structure resulting from hybridization with the conduction band, particularly near the PbTe band gap, is expected to persist in the real system.

Impurity band splittings due to impurity-impurity interaction.—In order to see how the impurity-impurity interaction (or impurity concentration) affects the impurity bands and their average positions, calculations were carried out using the (2×2×2) supercell with (In,In), (Ga,Ga), and (Tl,Tl) substitutional impurity pairs. Band structures for the pairs with the two atoms which are the 2nd n.n. and the 5th n.n. are shown in Figs. 5.9(a)-(f). In the former case, the impurity-impurity distance is 6.55 Å (before relaxation) with one impurity at the center of the cell;[4] whereas in the latter it is 11.35 Å (before relaxation) with one impurity atom at the center and another one at the corner of the cell. As can be seen from the figures, there are splittings of the impurity bands due to the impurity-impurity interaction. Each impurity band now splits into two which can be considered as the bonding and antibonding states formed out of the DDSs which are themselves the antibonding states of the group III s and Te p states. The splittings is large when the pair distance is small and vice versus. One should see only one impurity band when the impurities are far apart (low impurity concentration), in which case there is one impurity atom (on the average) inside a (2×2×2) supercell. When the impurities are closer (high impurity concentration), there are at least two impurity bands [Figs. 5.9(a)-(f)], when there are two impurities (on the average) inside the (2×2×2) supercell, with one impurity band has a minimum at the CBM (at the Γ point). The other impurity band, which is split-off due to impurity-impurity interaction, can be either above the CBM, in the band gap, at or below the VBM (also at the Γ point).

[4]This is also the pair configuration [among the five possible configurations of (Ga,Ga), (In,In), and (Tl, Tl)] which has the lowest energy.

5.4.3 Searching for Good Thermoelectric Materials

As was discussed in the Introduction, $AgPb_mSbTe_{m+2}$ (LAST-m) compounds have shown extremely promising thermoelectric performance (for m=18). It is, therefore, important to understand the band structure of LAST-m for large m values. Although the real system appears to be very complicated [15, 17], as a first-order approximation LAST-m can be modeled using the supercell model $RR'M_mTe_{m+2}$ (m=30) which has been described in Sec. 5.2, where LAST-m was considered as PbTe simultaneously doped with R=Ag and R'=Sb. The calculations clearly show that the host band structure is modified by Ag and Sb. I have also investigated what happens if one chooses (Ag,Bi) instead of (Ag,Sb) or replaces Ag by Na or K.

Band structures of PbTe doped with Ag, Sb, and Bi.—Before discussing the band structures of $RR'M_mTe_{m+2}$ (m=30) systems, one would like to consider the effects of each impurity on the band structure of PbTe separately. In Figs. 5.10(b)-(d), the band structures of $RPb_{31}Te_{32}$ are given for R=Ag, Sb, or Bi. The impurity band associated with Ag [the dash-dotted curve in Fig. 5.10(b)] is the nearly flat band (along Γ-X-M-Γ) split off from the rest of the valence band. This band, however, overlaps with the states near the valence-band top. An examination of the partial charge density associated with this band shows that it is predominantly Te p hybridizing with Ag d. The band, therefore, can be identified with the resonant state in the DOS which has been discussed previously [see the inset of Fig. 4.12(a)]. The Fermi level lies below the VBM (by ~40 meV) indicating that the system is hole-doped. The Ag impurity at this concentration (~3%) reduces the PbTe band gap from 105 meV to 73 meV. This reduction in band gap should persist in improved (beyond DFT-GGA) calculations. Note that the conduction band degeneracy (fourfold, without spin) is lifted near the CBM (at the Γ point) in the presence of the impurity.

The "impurity bands" associated with Sb and Bi [the dash-dotted curves in Figs. 5.10(c) and 5.10(d)] arise from strong hybridization between the impurity p

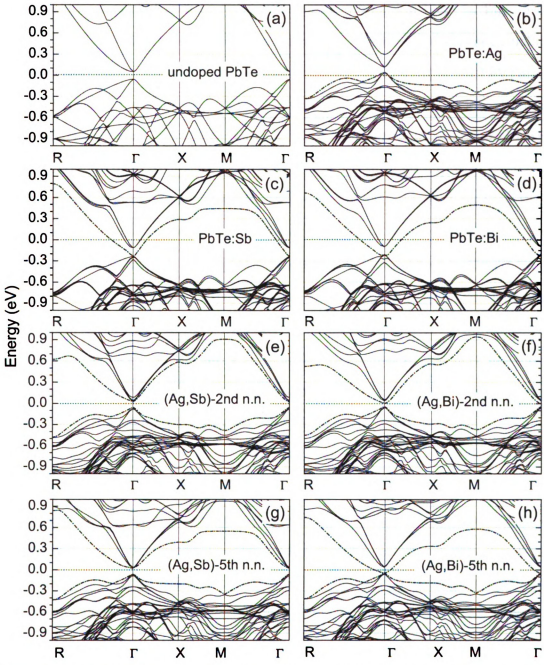

Figure 5.10: Band structure of undoped PbTe and PbTe doped with Ag, Sb, Bi, (Ag,Sb), and (Ag,Bi). The results were obtained in calculations using the (2×2×2) supercell with SOI included. The two impurity atoms in a pair are either the second (2nd n.n.) or the fifth (5th n.n.) nearest neighbors of one another. The Fermi level (0 eV) is set to the highest occupied states or in the middle of the band gap.

level which lies ~0.6 eV, about 0.7 eV above the conduction band minimum and the lowest conduction band states. This results in the splitting off of one of the fourfold degenerate conduction bands of PbTe [the lowest conduction band in Figs. 5.10(c) and 5.10(d)]. The CBM of PbTe, which originally has eightfold degeneracy (including spins) at the Γ point, now splits into a sixfold degenerate level (at ~ -0.1 eV) and the twofold degenerate level (at ~ -0.3 eV) which belongs to the "hybridized impurity band". Partial charge analysis shows that this "impurity band" associated with Sb (Bi) is predominantly Sb (Bi) p hybridizing with Pb p. The impurity bands come down and close the band gap. Since Sb and Bi have one more electron than Pb, the Fermi level cuts the conduction band and the system is metallic, actually a highly degenerate semiconductor. The splitting between the "impurity band" and the rest of the bands above is spin-orbit-induced and is, therefore, larger for Bi. This makes the impurity band of Bi overlap with the VBM (of PbTe) at the Γ point. Both Sb and Bi leave the valence-band top almost unaffected except at and near the Γ point. The Fermi level in the conduction band is above the CBM by ~114 meV (Sb) and by ~94 meV (Bi), which indicates that the systems are electron-doped.

Simultaneous doping with monovalent and trivalent atoms.—When PbTe is simultaneously doped with (Ag,Sb) or (Ag,Bi), the impurity band associated with the monovalent atom (Ag) in the valence band pushes the impurity band associated with the trivalent atom (Sb or Bi) upwards and the band gap opens up at the Γ point for certain pair configurations. This phenomenon is a result of charge compensation between the two impurity atoms and is independent of the relative separation between Ag and Sb, but depends on the distance between Ag and Bi. The gaps at the Γ point in the case of (Ag,Sb) are 94.1, 78.2, 81.5, 83.3 meV when the two atoms in the pair are at the first, the second, the third, and the fifth n.n., respectively. For comparison, the band gap for PbTe is 105 meV. For (Ag,Bi), the gaps at Γ are 43.4 and 0 meV for (Ag,Bi) for the second and the fifth n.n. distances, respectively, and

negative for other distances. Since the splitting of the conduction band is caused by spin-orbit part of the impurity potential, this splitting is larger and hence the band gap is smaller (or even negative) in the (Ag,Bi) case because SOI is much stronger in Bi. Since DFT-GGA underestimates the band gap of PbTe, the actual band gaps should be larger than those given above. Experimentally, diffuse reflectance measurements in $Ag_{1-x}Pb_{18}MTe_{20}$ (M=Bi,Sb) give an apparent gap of 0.25 eV for M=Bi and 0.28 eV for M=Sb [112]; both for x=0. The difference of ~30 meV in the band gap is consistent with the above calculated values when the two atoms in a pair are at the second n.n. distance [43.4 meV for (Ag,Bi) and 94.1 meV for (Ag,Sb)]. If the conduction band states are shifted rigidly up in energy by ~0.2 eV (to correct for DFT-GGA), the agreement between theory and experiment is pretty good.

In the current model ($RR'Pb_{30}Te_{32}$), the impurity concentration is ~3%, whereas in experiments, typically, it is ~5% [15, 112]. One, therefore, should expect that a monovalent atom (Ag) can easily find itself close enough to a trivalent atom (Sb or Bi) to have an impact on the latter. However, there is still a finite chance for an impurity atom to be isolated or closer to another atom of the same kind, depending on the actual distribution of the impurity atoms in the samples and the ratio between the monovalent and the trivalent atoms. This suggests that one can tune the band gap of the doped PbTe systems by tuning the Ag/Sb(Bi) ratio.

Tuning the transport properties by tuning the Ag/Sb(Bi) ratio.—Transport properties measurements carried out on n-type $Ag_{1-x}Pb_{18}MTe_{20}$ (M=Sb; x=0, 0.14, and 0.30) show that the electrical conductivity increases and the absolute value of the thermopower decreases with decreasing Ag concentration (i.e., with increasing x) at a given temperature [112]; see also Figs. 5.11(a) and 5.11(b). Let us assume that intrinsic point defects (Te vacancies) are responsible for the observed n-type conductivity, and for the sake of argument, assume that these defects do not perturb the

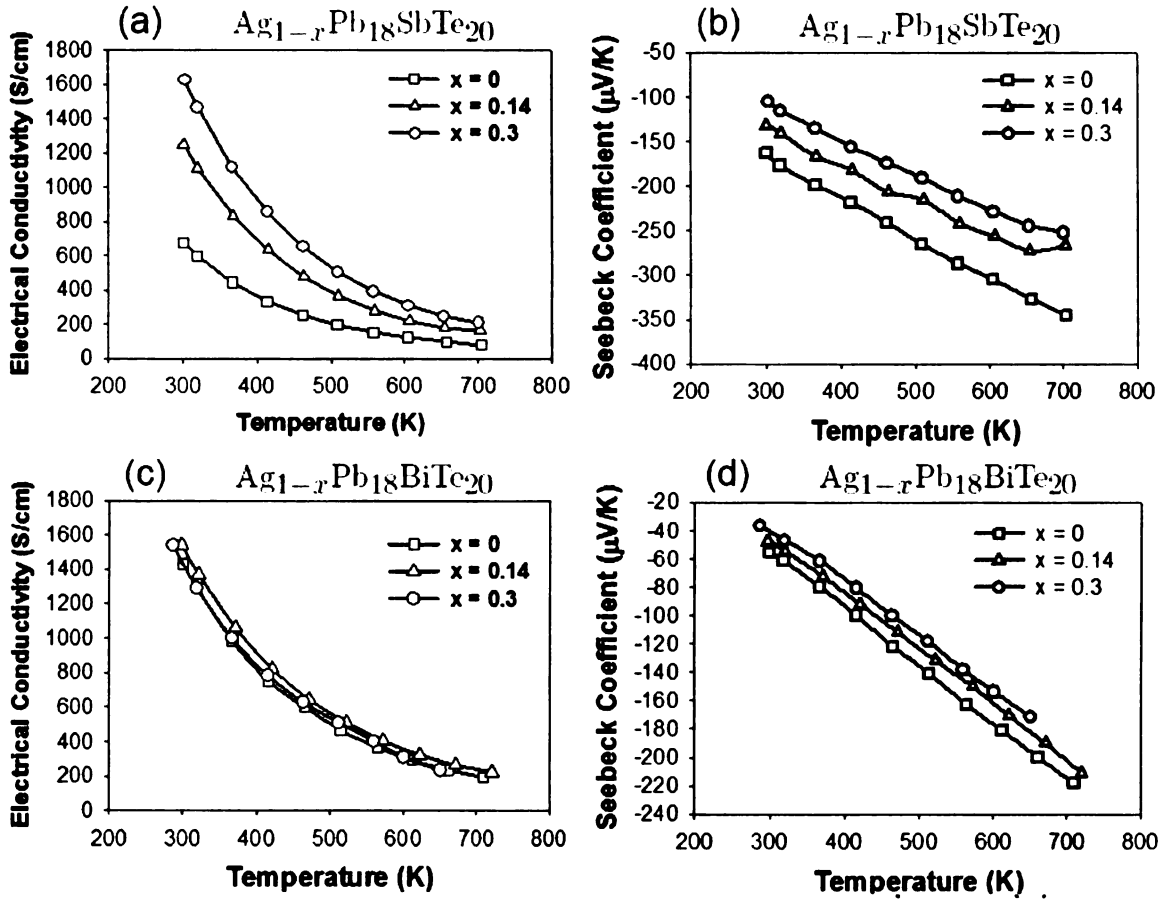

Figure 5.11: Electrical conductivity and thermopower (Seebeck coefficient) of $Ag_{1-x}Pb_{18}MTe_{20}$ (M=Bi,Sb); see also Ref. [112]. Courtesy of M. G. Kanatzidis.

band structures of PbTe doped with Ag, Sb, and (Ag,Sb) presented above.[5] With these assumptions, one can explain the observed behavior of the electrical conductivity and thermopower as the following. Increasing the Ag content increases the number of (Ag,Sb) pairs and reduces the number of isolated Sb impurities. This results in the widening of the band gap and reduction in the active carrier concentrations, which leads to a decrease in the electrical conductivity and increase in the magnitude of thermopower. The substitution of Sb by Bi also produces similar behavior [112]; see Figs. 5.11(c) and 5.11(d). The dependence of the electrical conductivity and the thermopower on x is, on the other hand, much weaker in the case of Bi [112]. There is

[5]As will be presented in Sec. 5.6, a Te vacancy in PbTe acts like Sb (and Bi) in the sense that it introduces a similar "hybridized impurity band" into the band gap region and turns PbTe into a n-type system.

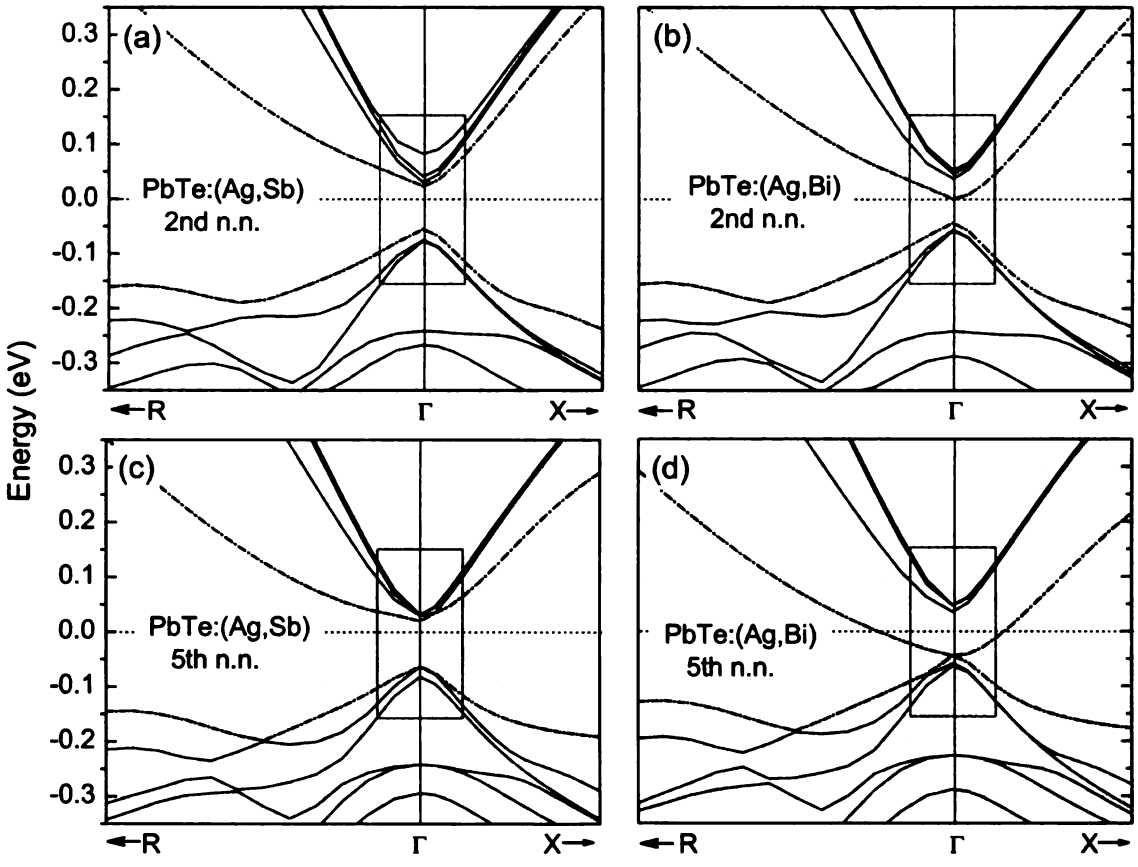

Figure 5.12: Band structure near the Γ point of PbTe doped with (Ag,Sb) and (Ag,Bi) impurity pairs. The Fermi level (0 eV) is set to the highest occupied states or in the middle of the band gap.

also an anomaly in the electrical conductivity for x=0.14 [see Fig. 5.11(c)]. These differences are possibly due to the band crossing associated with the Bi impurity band. Recent studies of Zhu *et al.* [191] on quenched $AgPb_{18}Sb_{1-y}Te_{20}$ (y=0.0, 0.1, 0.3, and 0.5) system also showed that increasing the Sb content (i.e., with decreasing y) results in reduced electrical conductivity and increase in thermopower. In this case, the increase of the Sb/Ag ratio (up to 1) increases the probability of having Ag-Sb pairs and reduces the number of isolated Sb impurities.

Why Sb is better than Bi?—In order to see the difference between the two systems, PbTe codoped with (Ag,Sb) and with (Ag,Bi), we show in Figs. 5.12(a)-(d) the blowups of the band structures near the band gap at the Γ point. Since these two systems are doped n-type [15, 112] by suitable adjustments of Ag concentration

(and the presence of unknown intrinsic defects), we focus near the conduction-band bottom. Besides the difference in the band gap between these two systems, there are important differences in the arrangement of the energy bands. For (Ag,Sb) at the second n.n. distance [Fig. 5.12(a)], there is a group of three bands (each band is a doublet where spin is included) which are close in energy at the Γ point; about 42 meV above the highest band in this group is another band (which is also a doublet). The arrangement of the bands is in the reverse order in the (Ag,Bi) case, the doublet is below the sextet by $\sim$37 meV. This means that, for the same carrier (electron) concentration, the chemical potential in the (Ag,Sb) case is lower (close to the CBM) than in the (Ag,Bi) case. This and the larger band gap for (Ag,Sb) which helps reduce the contribution from the minority carriers (holes), result in a larger thermopower for (Ag,Sb) doped PbTe, as seen experimentally.

Transport properties measurements of $Ag_{1-x}Pb_{18}MTe_{20}$ (M=Bi, Sb) show that for both the systems, the thermopower decreases dramatically when Sb is replaced by Bi; from -100 μV/K at 300 K to -250 μV/K at 700 K for Sb and -40 μV/K at 300 K to -160 μV/K at 600 K for Bi [112]; see Figs. 5.11(b) and 5.11(d). The lattice thermal conductivity of the Bi analog is, however, higher than of Sb because of the smaller mass fluctuation in the system (Sb is much lighter than Pb, whereas Bi and Pb are comparable). This, coupled with the lower values of the thermopower, results in much lower ZT in $Ag_{1-x}Pb_{18}BiTe_{20}$, ZT=0.53 (for x=1) and 0.44 (x=0.7) at 665 K [112], compared to ZT $\sim$1.6 at 665 K in $AgPb_{18}SbTe_{20}$ [15]. From the calculated band structures [Figs. 5.10(e)-(h)], one expects to also see large thermopowers in p-type LAST-m and LBST-m, if they can be made successfully, because the bands near the VBM are flatter (than those near the CBM).

Why Na and K are good substitutes for Ag?.—The substitution of Ag in LAST-m by Na or K have shown that these Ag-free thermoelectrics are also very promising [19, 20]. The p-type $Na_{1-x}Pb_mSb_yTe_{m+2}$ gives ZT $\sim$1.7 at 650 K for m=20, x=0.05,

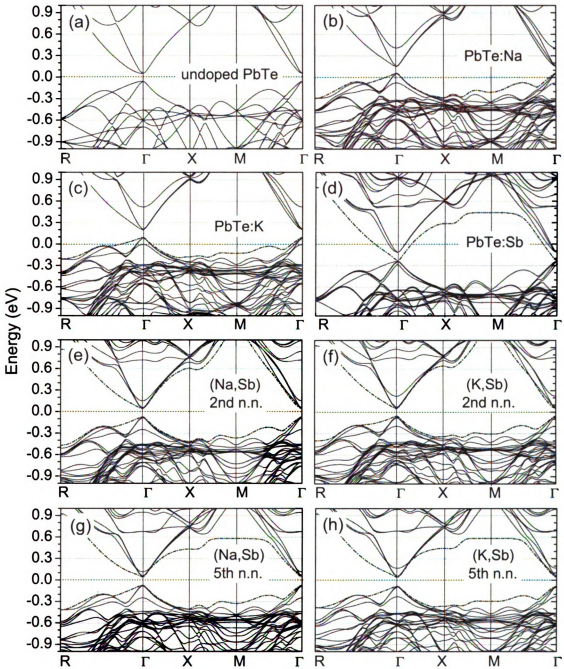

Figure 5.13: Band structure of undoped PbTe and PbTe doped with Na, K, Sb, (Na,Sb), and (K,Sb). The results were obtained in calculations using the (2×2×2) supercell with SOI included. The two impurity atoms in a pair are either the second (2nd n.n.) or the fifth (5th n.n.) nearest neighbors of one another. The Fermi level (0 eV) is set to the highest occupied states or in the middle of the band gap.

and y=1 [19], whereas the n-type $K_{1-x}Pb_mSb_yTe_{m+2}$ gives ZT=1.60 at 600 K for m=20, x=0.05, and y=1.2 [20]. These systems are good thermoelectrics because of their large thermopower and low thermal conductivity. The latter is believed to be due to the nanostructuring observed in the systems [19, 20], which is also consistent with the defect clustering studies presented in Sec. 5.3. To see how large the thermopower values can be, the band structures of PbTe doped with Na, K, (Na,Sb), or (K,Sb) have been calculated and the results are presented in Figs. 5.13(a)-(h).

Although thought to be ideal acceptors [144], Na and K also produce significant changes in the PbTe band structure with band splittings near the valence-band top and conduction-band bottom [Figs. 5.13(b) and 5.13(c)]. The VBM (CBM) of PbTe, which originally has eightfold degeneracy, now splits into a group of three nearly degenerate bands and a standalone band (a doublet) at the Γ point. The band nominally associated with Na (or K) [the dash-dotted bands in Figs. 5.13(b) and 5.13(c)], in fact, does not have any Na (K) character since the Na (K) s level is high up in the conduction band. It is, however, formed primarily out of p-orbitals associated with Te atoms which are the n.n. of the Na (K) atom (ion). This band will be called the "impurity band" since it is impurity-induced band splitting off of the topmost valence band from the rest of the the PbTe valence bands. The band structure for Sb doped PbTe has been discussed previously but is again given here for comparison. Simultaneous doping of Sb with Na (or K) helps in lifting of the Sb impurity bands upwards in energy, resulting in a band gap at Γ. Na (K) acts like Ag in this sense. However, the Sb impurity band is pushed to higher energy for Na (K) compared to Ag, and the new band gap can be even larger than that of the undoped PbTe; 114 and 112 meV for the (Na,Sb) and 100 and 122 meV for the (K,Sb) pair at the second and the fifth distances, respectively, as compared to 105 meV for the undoped PbTe. This suggests that Na and K, which are more ionic than Ag, almost perfectly compensate the charge perturbation created by the Sb atom.

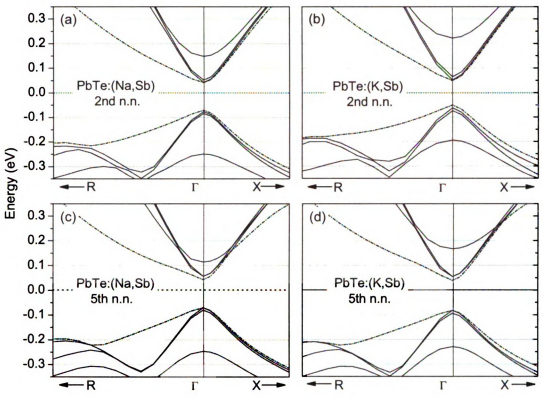

Figure 5.14: Band structure near the Γ point of PbTe doped with (Na,Sb) and (K,Bi) impurity pairs. The Fermi level (0 eV) is set to the highest occupied states or in the middle of the band gap.

There are other differences in the band structures of PbTe doped with Na, K, and Ag. The splitting between the threefold nearly degenerate band and the nondegenerate band (without spin; near the conduction-band bottom) at the Γ point increases in going from Ag [Figs. 5.12(a) and 5.12(c)] to Na [Figs. 5.14(a) and 5.14(c)] to K [Figs. 5.14(b) and 5.14(d)]; see Table 5.3. The trend in the splittings near the conduction-band bottom reflects the s level of Ag, Na, and K, which are at -5.99 eV (Ag), -4.96 eV (Na), and -4.01 eV (K) [84]. The trend in the splitting near the valence-band top is probably due the difference in the dopants (Ag, Na, K) and the host (Pb) potentials. Since the difference in the splitting between Ag, Na, and K is small near the valence-band top and large near the conduction-band bottom, one expects that the difference in the thermopower (at a given carrier concentration) is small for p-type systems but larger for the n-type systems.

Table 5.3: The splitting (in meV) between the group of three nearly degenerate bands and the single band at the conduction-band (CB) bottom and valence-band (VB) top (at the Γ point) of PbTe codoped with Sb and either Ag, Na, or K. The two atoms in a pair are either the second (2nd) or the fifth (5th) n.n. of one another.

Pair	(Ag,Sb)		(Na,Sb)		(K,Sb)	
	2nd n.n.	5th n.n.	2nd n.n.	5th n.n.	2nd n.n.	5th n.n.
CB Bottom	42	0	96	58	157	112
VB Top	167	160	165	166	132	136

Experimentally, it has been found that $Na_{1-x}Pb_mSb_yTe_{m+2}$ [19] is p-type whereas $K_{1-x}Pb_mSb_yTe_{m+2}$ is n-type. This has been a puzzle for a long time. We believe that the difference is due to native point defects; defect complexes formed out of native defects with the dopants possibly playing a role in determining the carrier type and carrier concentration int these systems. In $Na_{0.8}Pb_{20}Sb_yTe_{22}$ compositions with y=0.4, 0.6, and 0.8, Poudeu *et al.* [19] have found that the p-type electrical conductivity decreases and the thermopower increases as one increases the Sb content (y). One can assume that Pb vacancies are responsible for the observed p-type conductivity in the Na analog.[6] Then the behavior of the electrical conductivity and thermopower can be understood in terms of the calculated band structures where the increase of the Sb/Na ratio (up to 1) increases the probability of having (Na,Sb) pairs and reduces the isolated Sb impurities. This is similar to what has been discussed for Ag.

5.5 Impurity Bands in GeTe and SnTe

5.5.1 GeTe

One of the best materials today for power generation is $(AgSbTe_2)_x(GeTe)_{1-x}$, known as TAGS (stands for Te-Ag-Ge-Sb), which has ZT ~1.2 at 700 K (p-type) [5].

[6] As will be presented in Sec. 5.6, a Pb vacancy in PbTe acts like the monovalent impurities. It introduces a similar "impurity band" into the band gap region and turns PbTe into a p-type system.

This system is thought to be a solid-solution composition of $AgSbTe_2$ and GeTe. A similar system, $(AgBiTe_2)_x(GeTe)_{1-x}$, has also been found to be a good thermoelectric material with ZT=1.32 at 700 K (for x=0.03) [113]. To understand the role Ag and Sb (or Bi) play in these GeTe-based systems, band structure calculations were carried out where Ag and Sb (or Bi) were treated as impurities in the GeTe host.

Band structure of undoped GeTe.—GeTe has a NaCl-type structure like PbTe and SnTe, but with a slight distortion due to a phase transition at low temperature [100]. Since the distortion is small, the NaCl-type structure was assumed in the current studies. In Fig. 5.15(a) the band structure of undoped GeTe along different high symmetry directions of the sc BZ (a=12.04 Å) is shown. This band structure, which was obtained using the (2×2×2) supercell with 64 atoms/cell, looks very much like that of PbTe. The band gap (at Γ) is found to be 0.243 eV, 20% larger than the experimental value (of 0.20 eV at 0 K) [60]. Without SOI, our calculations give GeTe a band gap of 0.388 eV. This reduction of the band gap (by 37.4%) is caused by a small upward shift (by ∼0.050 eV at Γ) in the energy of the topmost valence band and the spin-orbit-induced splitting of the bottommost conduction band where one of the split bands is pushed down (by ∼0.096 eV at Γ) in energy.

Band structures of GeTe doped with Ag, Sb, and Bi.—Introduction of Ag into GeTe (Ag substitutes for Ge) results in a p-type system with the Fermi level below the VBM. An "impurity band" [the dash-dotted curve in Fig. 5.15(b)] splits off from the valence-band top (of GeTe). Sb and Bi, on the other hand, make GeTe n-type. Impurity bands associated with Sb and Bi which are split off from the GeTe conduction-band bottom significantly reduce the band gap (in the case of Sb) or even close the gap (Bi) [see Figs. 5.15(c) and 5.15(d)]. These observations are similar to what was seen for Ag, Sb, and Bi in PbTe, except that band crossing is less severe for GeTe because it has a larger band gap. Introduction of Ag simultaneously with Sb (or Bi) also helps lift the impurity band associated with Sb (or Bi) up and increases (or even open up)

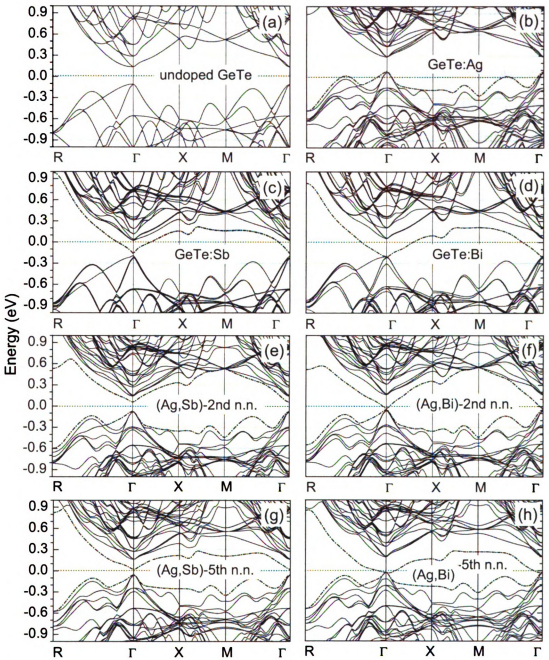

Figure 5.15: Band structure of undoped GeTe and GeTe doped with Ag, Sb, Bi, (Ag,Sb), and (Ag,Bi). The results were obtained in calculations using the (2×2×2) supercell with SOI included. The two impurity atoms in a pair are either the second (2nd n.n.) or the fifth (5th n.n.) nearest neighbors of one another. The Fermi level (0 eV) is set to the highest occupied states or in the middle of the band gap.

the gap [see Figs. 5.15(e)-(h)], again similar to what was seen in PbTe [Figs. 5.10(e)-(h)]. However, the arrangement of the energy bands near the CBM of (Ag,Sb) doped GeTe is in the reverse order of that in PbTe. The nondegenerate band is now at lower energy than the nearly threefold degenerate band.

Simultaneous doping with monovalent and trivalent atoms.—Although (Ag,Sb) and (Ag,Bi) doped GeTe have the same band arrangements near the CBM, the splitting between the threefold degenerate band and the nondegenerate "impurity band" is smaller in (Ag,Sb); 82.8 and 143.8 meV at the second and the fifth n.n. compared to 194.9 and 219.4 meV for (Ag,Bi) also at the second and the fifth n.n. For n-type thermoelectrics, only the lowest conduction band should contribute. (Ag,Sb) doped system should give higher thermopower compared to (Ag,Bi) because the former has a larger band gap. Although the arrangement of the energy bands in the conduction-band bottom does not matter for p-type thermoelectrics, the larger band gap should also result in larger thermopower in the (Ag,Sb) case, compared to the (Ag,Bi); again, due to reduced intrinsic contributions in the (Ag,Sb) system. The system with Bi, on the other hand, should have lower lattice thermal conductivity because of the larger mass difference between Bi and Ge. Taking into account all these different factors, one can qualitatively understand why p-type $(AgBiTe_2)_x(GeTe)_{1-x}$ [113] and the p-type TAGS system [5] have comparable ZT values.

5.5.2 SnTe

Besides the doped PbTe and GeTe systems, materials based on SnTe have also shown to be promising for thermoelectric applications. Androulakis *et al.* [25] have reported an unusual coexistence of large thermopower and degenerate doping in the nanostructured material $Ag_{1-x}SnSb_{1+x}Te_3$ (x=0.15). This system shows a positive thermopower of $\sim$160 μV/K at 600 K and an almost metallic carrier concentration of $\sim 5\times10^{21}$ cm^{-3}. Studies of low temperature properties of $Ag_{1-x}SnSb_{1+x}Te_3$ (x=0,

0.15) and $Ag_{1-x}Sn_2Sb_{1+x}Te_4$ (x=0.1) show that these heavily doped systems have anomalously large linear heat capacity and temperature independent paramagnetic susceptibility [54]. *Ab initio* electronic structure calculations were carried out for these systems using superlattice models[7] and the experimental data have been explained in terms of a rapidly changing electronic DOS and pseudogap structure near the Fermi energy [54]. In order to fully understand the role Ag and Sb play in these and other SnTe-based systems, especially those at low impurity concentration (lightly doped) limit (~3%), band structure calculations were carried out where Ag and Sb were treated as impurities in SnTe.

Electronic anomalies in SnTe.—Fig. 5.16(a) shows the band structure of undoped SnTe in calculations using the (2×2×2) supercell. As in PbTe and GeTe, the band gap in SnTe occurs at the Γ point of the sc BZ (the L point in the fcc BZ of the primitive cell). However, unlike in PbTe and GeTe, SOI in SnTe increases the band gap by ~50%; from 0.054 eV (without SOI) to 0.105 eV (with SOI).[8] The band structure of SnTe doped with Ag is shown in Fig. 5.16(b). The "impurity band" associated with Ag [the dashed-dotted curve in Fig. 5.16(b)] is the hybridized Ag d and Te p band split off from the valence-band top. The impurity band associated with Sb [the dash-dotted surve in Fig. 5.16(c)], on the other hand, splits off from the conduction-band bottom and is predominantly Sb p with some hybridization with Sn p. This hybridized impurity band comes down and closes the gap. These observations are similar to PbTe and GeTe doped with Ag and Sb. There are, however, noticeable differences near the conduction-band bottom at the Γ point; the CBM is not at the Γ point but near Γ and along the Γ-R and Γ-X directions. The Γ point now becomes a saddle point. However, the separation between the maximum at Γ and the VBM (close to Γ) is small; e.g., ~3 meV for SnTe doped with Ag. This breaking of the

[7]These superlattice models were constructed based on the results obtained in MC simulations of an ionic model (presented in Chapter 1).

[8]The experimental band gap of SnTe is 0.3 eV at 0 K (see Ref. [192]).

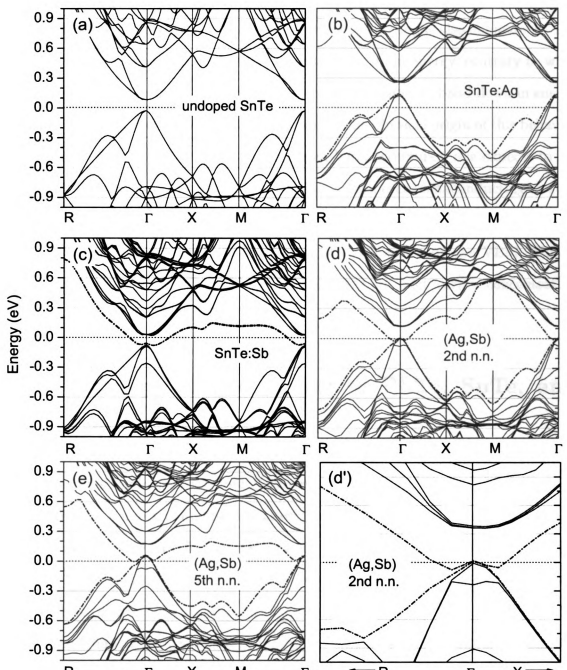

Figure 5.16: Band structures of undoped SnTe and SnTe doped with Ag, Sb, and (Ag,Sb). A blowup of the band structure of SnTe doped with (Ag,Sb) at the 2nd n.n. near the Γ is presented in (d'). The results were obtained in calculations using the (2×2×2) supercell with SOI included. The Fermi level (at 0 eV) is set to the highest occupied states.

symmetry near the CBM is also observed in SnTe simultaneously doped with Ag and Sb [Fig. 5.16(d) and 5.16(e)].

The electronic structure in the case of simultaneous doping is also anomalous. The introduction of Ag does not lift the Sb impurity band up in energy, contrary to what was observed in PbTe and GeTe. It, actually, pulls the impurity band down in energy resulting in a large overlap with the valence band. The physical origin of this behavior is still an open issue.[9] Based on the calculated band structures, one expects to see the (Ag,Sb) doped SnTe systems to exhibit highly degenerate semiconducting or even metallic conduction. However, high thermopower for p-type SnTe-based systems is also possible because of the high degeneracy of the bands near the VBM. This is consistent with the observation of large thermopower and high carrier concentration in experiments [25].

5.6 Vacancy-Induced Bands in PbTe, SnTe, and GeTe

One of the remarkable properties of the narrow band-gap IV-VI binary semiconductors is that they have a range of nonstoichiometry accompanied by either cation or anion vacancy. Vacancies in PbTe have been extensively studied by various authors[136, 138, 144, 140] which show that Pb vacancies produce p-type and Te vacancies produce n-type PbTe, respectively. I have also discussed my results for Pb and Te vacancies in PbTe in Chapter 4 with a careful look at the nature of the defect states created by the vacancies in bulk PbTe and in thin films. Complete band structures which are expected to be useful in interpretation the transport properties of these systems are, however, still lacking. In this section, I will present the calculated band structures using the (2×2×2) supercell model (one vacancy per 64 lattice sites) showing the

[9]It is likely that this behavior is associated with the "band inversion" observed in SnTe[193].

impurity bands associated with Pb and Te vacancies in PbTe. I have also extended these studies to vacancies in GeTe and SnTe.

Nature of the vacancy-induced bands.—Figs. 5.17(a)-(f) show the band structures of PbTe, SnTe, and GeTe with cation and anion vacancies. The impurity bands associated with the cation vacancies are the ones that split off from the valence-band top [the dash-dotted curves in Figs. 5.17(a), 5.17(c), and 5.17(e)]; the impurity bands associated with the anion (Te) vacancies, on the other hand, split off from the conduction-band bottom [the dash-dotted curves in Fig. 5.17(b), 5.17(d), and 5.17(f)]. Partial charge density analysis shows that the formers are predominantly p states associated with the n.n. Te atoms of the cation vacancy, whereas the latters are predominantly cation p states (with some hybridization with Te) associated with the n.n. cation atoms of the Te vacancy. The partial charge densities for Pb and Te vacancies in PbTe are similar to those presented earlier [see Figs. 4.16(a) and 4.16(b)].

Defect levels.—Since the widths of the impurity bands are large, the concept of "defect level" may not be very meaningful here. However, one can take the average position of the impurity band as the defect level. Since all the impurity bands associated with the cation (Pb, Sn, Ge) vacancies are in the valence band, their impurity levels are also in the valence band. The Fermi levels are $\sim$0.1 eV, 0.25 eV, and 0.2 eV below the VBM for the Pb, Sn, and Ge vacancies, respectively, indicating that the systems are p-type. The impurity bands associated with the Te vacancy in PbTe, SnTe, and GeTe all have large dispersions and their average positions can be in the conduction band (for Te vacancy in PbTe), in the band gap (in GeTe), and in the valence band (in SnTe).

The results reported by other authors for Te vacancies in SnTe are somewhat controversial. Calculations carried out by Hemstreet [138] (using the XSW-cluster method) and Polatoglou [194] (using the Green's function scattering-theoretic method) showed that one Te vacancy in SnTe introduced two electrons in the conduction band,

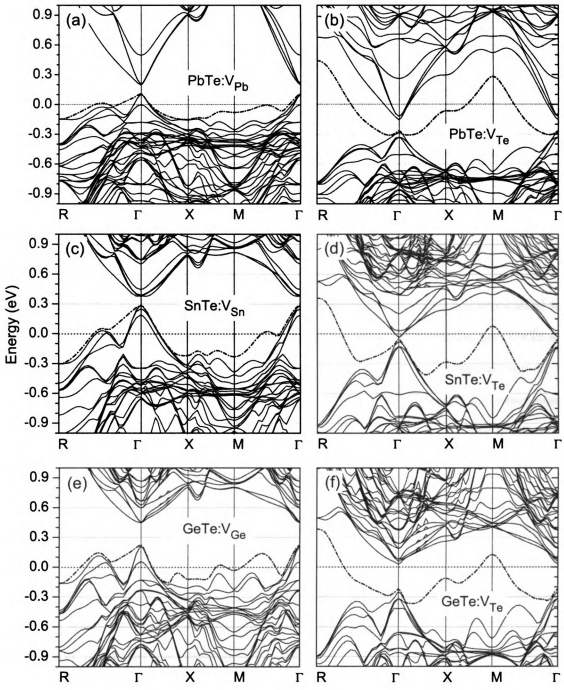

Figure 5.17: Band structures in the simple cubic BZ showing the impurity bands (dash-dotted curves) associated with cation and anion vacancies in PbTe, SnTe, and GeTe. The results were obtained in calculations using the (2×2×2) supercell with SOI included. The Fermi level (at 0 eV) is set to the highest occupied states.

thereby making the system n-type. Within the framework of the so-called "p-model", Volkov and Pankratov [140], on the other hand, reported that the defect level associated with Te vacancies in SnTe was in the valence band and acted like an acceptor, just like a Sn vacancy. My calculated band structure seems to support the latter scenario. My calculations also suggest that a Te vacancy in GeTe may also act as an acceptor because the average position of the corresponding impurity band is very close to the VBM. This, in addition to Ge vacancies, may also be responsible for the observed persistent p-type and metallic conduction in GeTe [195].

5.7 Summary

In summary, the energetics of defect clustering and the impurity bands associated with various impurities and native point defects (vacancies) in PbTe, SnTe, and GeTe were studied. My *ab initio* calculations show that the impurity pairs formed out of one monovalent and one trivalent atoms in PbTe, SnTe, and GeTe have the lowest energy when the two impurity atoms are the second nearest neighbors of one another. Te atoms near an impurity pair tend to go off-center. One, therefore, should carry out experimental and more theoretical studies to see if there is off-centering in the real samples and how it impacts on the thermal conductivity of these systems. Electronic structure was strongly affected by the defects (depends on the relative pair distance). Band degeneracy at the VBM and CBM of the host material is removed and there are band splittings in the presence of an impurity or a vacancy. Once the spin-orbit interaction is turned on, these splittings become larger because of the symmetry breaking. They also depends on the type of the impurity or the vacancy.

The problem of deep defect states in PbTe is revisited by carefully studying the impurity (HDS and DDS) bands associated with the group III (Ga, In, Tl) impurities. The HDS and DDS bands were found to split off neither from the valence-band top nor the conduction-band bottom, but they are the results of the strong interac-

tion between the impurity s-state and the entire valence band. There is also strong spin-orbit-induced hybridization between the DDS band associated with In and the conduction band. Overlap between the DDS bands associated with Ga and Tl and the conduction band is possible when the impurity bandwidths are large enough (high impurity concentration). The impurity levels of In, Ga, and Tl are found to be above the CBM, in the band gap, and below the VBM, respectively. Impurity-impurity interaction (present for large impurity concentrations) is found to cause large impurity band splittings in group III doped PbTe.

For other impurities in PbTe, SnTe, and GeTe, I find that the impurity bands associated with the monovalent impurities (Na, K, Ag) split off from the topmost valence band but are degenerate with other valence bands at the VBM. All these bands are, however, still in the valence band and the systems are hole-doped. The impurity bands associated with the trivalent impurities (Sb, Bi), on the other hand, split off from the conduction-band bottom with large dispersions towards the valence band. These bands reduce or even close the band gap. This phenomenon is due to the interaction between the cation (Sb, Bi) p states and the anion (Te) p states which tends to drive the systems towards highly degenerate semiconducting or (semi)metallicity. This is also consistent with what was observed in the LAST-m compounds (see Chapter 2) and the I-V-VII_2 and Tl-based III-V-VII_2 ternary chalcogenides (see Chapter 3). The simultaneous doping of one monovalent and one trivalent impurity, however, helps lift up (to higher energies) the impurity band associated with the trivalent impurity and the band gap increases/opens; except for the SnTe-based systems. One, therefore, can tune the monovalent-trivalent ratio to tune the band gap and the band structure in the neighborhood of the gap in PbTe and GeTe-based systems. SnTe behaves anomalously in the sense that the introduction of the monovalent impurity does not lift the trivalent impurity band up but pulls it further down towards the valence band. This anomalous behavior needs further study. The cation vacancies in PbTe,

SnTe, and GeTe act like the monovalent impurities, whereas the anion vacancies are more like the trivalent impurities. However, the dispersions of the anion-vacancy-induced bands towards the valence band are very strong in the case of SnTe and GeTe which put the corresponding defect levels in the valence band, instead of the conduction band. Based on the calculated band structures, I have been able to explain qualitatively some of the observed transport properties of the whole class of PbTe, SnTe, and GeTe-based thermoelectric materials.

Chapter 6

Open Issues and Outlook

This thesis concerns with the studies of charge ordering and self-assembled nanostructures in a class of quaternary systems and their phase diagram, defect clustering and nanostructure formation in bulk thermoelectrics, atomic and electronic structures of ternary chalcogenides, and nature of defect states in narrow band-gap semiconductors. The complete summaries of these studies have been given at the end of Chapters 2, 3, 4, and 5. In this chapter, instead of repeating them, I would only like to address some remaining open issues and provide outlook for future research.

• *Nanoscale structure formation in bulk thermoelectric materials.*—This thesis has presented attempts to tackle this problem using Monte Carlo and *ab initio* methods. The results are interesting and provide many insights on the role of the long-range electrostatic interaction and covalency, and the energetics of different impurity pairs. They are, however, still far from giving realistic pictures of the nanostructuring observed in real material samples because of the small number of atoms the calculations can handle and the finite size effects. A good understanding of this phenomenon should come from further experimental and theoretical studies. On the experiment side, one should use advanced techniques to provide detailed information about the embedded nanostructures, such as their composition and atomic orderings. On the theory side, study of nanoscale structure formation in bulk materials will require

multiscale modeling which makes use of a combination of simulation techniques at various levels of coarse-graining, i.e., different time and length scales [196, 197]. The results presented in this thesis can be used as a basis for these simulations. The ionic model presented in this thesis can also be expanded to include short-range interaction in order to better describe the real systems.

• *Direct calculations of transport properties from the calculated electronic structure.* —This thesis has also presented comprehensive studies of impurities and native point defects in narrow band-gap semiconductors. Based on the calculated electronic DOS and band structures, I have been able to explain some of the observed transport properties of the whole class of PbTe, SnTe, and GeTe-based thermoelectric materials. These studies are, however, still limited to a qualitative understanding of the transport properties of the materials. It is very desirable to calculate transport properties directly from the obtained band structures to have a quantitative understanding.

• *Theory of defect states in narrow band-gap semiconductors beyond the standard DFT and supercell models.*—Although the studies presented in this thesis have provided a broad general picture and a good understanding of the nature of defect-induced electronic states in narrow band-gap semiconductors, a general theory is still lacking. One should explore different methods, probably other than the standard DFT and supercell models, or develop new methods which are able to give a deeper and more systematic understanding of the defect states. One, for example, can construct *ab initio* effective Hamiltonians to study the arrangement of the energy bands near the band gap region in the band structure of group III doped PbTe and to understand the electronic anomalies in SnTe-based systems.

• *Origin of the n- or p-type conductivity in a certain material.*—Why $Ag_{1-x}Pb_{18}$ MTe$_{20}$ (M=Sb, Bi; x=0, 0.14, 0.3) systems [112] are n-type while there is Ag deficiency and they are supposed to behave like p-type systems? Why $Ag_{1-x}SnSb_{1+x}Te_3$ [25] is p-type while there is cation (Sb) redundancy and it is supposed to behave like a

n-type system? Why $Na_{1-x}Pb_mSb_yTe_{m+2}$ [19] is p-type whereas it K counterpart, $K_{1-x}Pb_mSb_yTe_{m+2}$ [20], is n-type? In order to answer these questions, one should carefully re-examine the stoichiometry in the samples and figure out how the impurity atoms go into the host material, i.e, as substitutional impurities on the cation (or anion) sites, interstitials, or precipitates. One should also examine to see if there is (re-)vaporization which can result in a depletion of the volatile element(s) thereby creating vacancies in the samples. Since impurities and vacancies have been considered separately in this thesis, it is natural to carry out studies on defect complexes formed out of both impurities and vacancies. These studies are expected to give a good understanding of the coupling between impurities and vacancies and possible explanation(s) of the conductivity type observed in a given system.

Bibliography

[1] Committee on CMMP 2010, National Research Council, *Condensed-Matter and Materials Physics: The Science of the World Around Us* (The National Academies Press, Washington DC, 2007).

[2] M. S. Dresselhaus, G. Chen, M. Y. Tang, R. Yang, H. Lee, D. Wang, Z. Ren, J.-R. Fleurial, and P. Gogna, Adv. Mater. **19**, 1 (2007).

[3] T. J. Seebeck, *Abh. Preuss. Akad. Wiss.*, p. 265 (1822-1823).

[4] A. F. Ioffe, *Semiconductor Thermoelectrics and Thermoelectric Cooling* (Infosearch Ltd, London, 1957).

[5] C. Wood, Rep. Prog. Phys. **51**, 459 (1988).

[6] G. D. Mahan, Solid State Physics **51**, 81 (1998).

[7] G. D. Mahan and J. O. Sofo, Proc. Natl. Acad. Sci. U.S.A. **93**, 7436 (1996).

[8] F. J. DiSalvo, Science **285**, 703 (1999).

[9] Y. Gelbstein, Z. Dashevsky, and M. P. Dariel, Physica B **363**, 196 (2005).

[10] K. Takahata and I. Terasaki, Jpn. J. Appl. Phys. **41**, 763 (2002).

[11] R. Venkatasubramanian, E. Siivola, T. Colpitts, and B. O'Quinn, Nature (London) **413**, 597 (2001).

[12] G. S. Nolas, D. T. Morelli, and T. M. Tritt, Ann. Rev. Mater. Sci. **29**, 89 (1999).

[13] T. C. Harman, P. J. Taylor, M. P. Walsh, and B. E. LaForage, Science **297**, 2229 (2002).

[14] T. C. Harman, M. P. Walsh, B. E. LaForge, and G. W. Turner, Jour. Elec. Mat. **34**, L19 (2005).

[15] K.-F. Hsu, S. Loo, F. Guo, W. Chen, J. S. Dyck, C. Uher, T. Hogan, E. K. Polychroniadis, and M. G. Kanatzidis, Science **303**, 818 (2004).

[16] M.G. Kanatzidis, S.D. Mahanti, and T.P. Hogan (Eds.), *Chemistry, Physics, and Materials Science of Thermoelectric Materials: Beyond Bismuth Telluride* (Kluwer Academic, New York, 2003).

[17] E. Quarez, K.-F. Hsu, R. Pcionek, N. Frangis, E. K. Polychroniadis, and M. G. Kanatzidis, J. Am. Chem. Soc. **127**, 9177 (2005).

[18] J. Androulakis, K. F. Hsu, R. Pcionek, H. Kong, C. Uher, J. J. D'Angelo, A. Downey, T. Hogan, and M. G. Kanatzidis, Adv. Mater. **18**, 1170 (2006).

[19] P. F. P. Poudeu, J. D'Angelo, A. D. Downey, J. L. Short, T. P. Hogan, and M. G. Kanatzidis, Angew. Chem. Int. Ed. **45**, 3835 (2006).

[20] P. F. P. Poudeu and M. G. Kanatzidis (to be published).

[21] J. Hafner, C. Wolverton, and G. Ceder, MRS Bull. **31**, 659 (2006).

[22] R. M. Martin, *Electronic Structure: Basic Theory and Practical Methods* (Cambridge University Press, Cambridge, 2004).

[23] W. G. Aulber, L. Jonsson, and J. W. Wilkins, Solid State Physics **54**, 1 (2000).

[24] U. von Barth, Phys. Script. T**109**, 9 (2004).

[25] J. Androulakis, R. Pcionek, E. Quarez, J.-H. Do, H. Kong, O. Palchik, C. Uher, J. J. D'Angelo, J. Short, T. Hogan, and M. G. Kanatzidis, Chem. Mater. **18**, 4719 (2006).

[26] T. C. King, Y. K. Kuo, M. J. Skove, and S.-J. Hwu, Phys. Rev. B **63**, 045405 (2001).

[27] T. C. King, Y. K. Kuo, and M. J. Skove, Physica A **313**, 427 (2002).

[28] T. C. King and Y. K. Kuo, Phys. Rev. E **68**, 036116 (2003).

[29] V. Levashov, M. F. Thorpe and B. W. Southern, Phys. Rev. B **67**, 224109 (2003).

[30] J.-R. Lee and S. Teitel, Phys. Rev. B **46**, 3247 (1992).

[31] P. Gupta and S. Teitel, Phys. Rev. B **55**, 2756 (1997).

[32] R. Dickman and G. Stell, in *Simulation and Theory of Electrostatic Interactions in Solutions*, edited by G. Hummer and L.R. Pratt (AIP, Woodbury, New York, 1999). p. 225.

[33] A. B. Walker and M. J. Gillan, J. Phys. C: Solid State Phys. **16**, 3025 (1983).

[34] L. Bellaiche and D. Vanderbilt, Phys. Rev. Lett. **81**, 1318 (1998).

[35] F. Bresme, C. Vega, and J. L. F. Abascal, Phys. Rev. Lett. **85**, 3217 (2000).

[36] G. H. Wannier, Phys. Rev. **79**, 357 (1950); Phys. Rev. B **7**, 5017(E) (1973).

[37] S. Alexander and P. Pincus, J. Phys. A: Math. Gen. **13**, 263 (1980).

[38] O. J. Heilmann, J. Phys. A: Math Gen. **13**, 1803 (1980).

[39] M. K. Phani, J. L. Lebowitz, and M. H. Kalos, Phys. Rev. B **21**, 4027 (1980).

[40] S. Kämmerer, B. Dünweg, K. Binder, and M. d'Onorio de Meo, Phys. Rev. B **53**, 2345 (1996).

[41] D. Bilc, S. D. Mahanti, K.-F. Hsu, E. Quarez, R. Pcionek, and M. G. Kanatzidis, Phys. Rev. Lett. **93**, 146403 (2004).

[42] K. Hoang, K. Desai and S. D. Mahanti, Phys. Rev. B **72**, 064102 (2005).

[43] M. Grousson, G. Tarjus, and P. Viot, Phys. Rev. E **62**, 7781 (2000); **64**, 036109 (2001).

[44] A. Z. Panagiotopoulos and S. K. Kumar, Phys. Rev. Lett. **83**, 2981 (1999).

[45] N. Metropolis, A. Rosembluth, M. Rosembluth, and A. Teller, J. Chem. Phys. **21**, 1087 (1953).

[46] M. P. Allen and D. J. Tildesley, *Computer Simulation of Liquids* (Clarendon, Oxford, 1987).

[47] J. Hoshen and R. Kopelman, Phys. Rev. B **14**, 3438 (1976).

[48] H. E. Stanley, *Introduction to Phase Transitions and Critical Phenomena* (Oxford University Press, New York, 1971).

[49] D. P. Landau and K. Binder, *A Guide to Monte Carlo Simulations in Statistical Physics* (Cambridge University Press, Cambridge, 2000).

[50] M. O'Keeffe, M. Eddaoudi, H. Li, T. Reineke, and O. M. Yaghi, J. Solid Stat. Chem. **152**, 3 (2000).

[51] See, e.g., K. T. Thomson and R. M. Wentzcovitch, J. Chem. Phys. **108**, 8584 (1998).

[52] A. Ciach and G. Stell, Phys. Rev. E **70**, 016114 (2004).

[53] K. Hoang, S. D. Mahanti, J. Androulakis, and M. G. Kanatzidis, in *Materials and Technologies for Direct Thermal-to-Electric Energy Conversion*, edited by J. Yang, T.P. Hogan, R. Runahashi, and G.S. Nolas (Mater. Res. Soc. Symp. Proc. **886**, Warrendale, PA, 2006), 0886-F05-06.

[54] K. Hoang, J. Androulakis, S. D. Mahanti, M. G. Kanatzidis, X. Tang, and Terry M. Trit (preprint).

[55] J. P. Perdew, K. Burke, and M. Ernzerhof, Phys. Rev. Lett. **77**, 3865 (1996).

[56] P. E. Blöchl, Phys. Rev. B **50**, 17953 (1994); G. Kresse and D. Joubert, *ibid.* **59**, 1758 (1999).

[57] G. Kresse and J. Hafner, Phys. Rev. B **47**, 558 (1993); **49**, 14251 (1994); G. Kresse and J. Furthmüller, *ibid.* **54**, 11169 (1996); Comput. Mat. Sci. **6**, 15 (1996).

[58] L. E. Ramos, L. K. Teles, L. M. R. Scolfaro, J. L. P. Castineira, A. L. Rosa, and J. R. Leite, Phys. Rev. B **63**, 165210 (2001).

[59] D. J. Singh, Mater. Res. Soc. Symp. Proc. **691**, G1.2 (2002).

[60] O. Madelung, H. Weiss, and M. Schultz (Eds.), *Landolt-Brnstein: Numerical Data and Functional Relationships in Science and Technology*, New Series, Vol. 17, Pt. a (Springer-Verlag, Berlin, 1982).

[61] K. Hoang, J. R. Salvador, S. D. Mahanti, and M. G. Kanatzidis, Phys. Rev. Lett. **99**, 156403 (2007).

[62] R. Detemple, D. Wamwangi, M. Wuttig, and G. Bihlmayer, Appl. Phys. Lett. **83**, 2572 (2003).

[63] J. H. Wernick and K. E. Benson, J. Phys. Chem. Solids **3**, 157 (1957); J. H. Wernick, S. Geller, and K. E. Benson, *ibid.* **4**, 154 (1958).

[64] S. Geller and J. H. Wernick, Acta Cryst. **12**, 46 (1959).

[65] R. M. Ayral-Marin, G. Brun, M. Maurin, and J. C. Tedenac, Eur. J. Solid State Inorg. Chem. **27**, 747 (1990).

[66] B. Eisenmann and H. Schäfer, Z. Anorg. Allg. Chem. **456**, 87 (1979).

[67] A. P. Deshpande, V. B. Sapre, and C. Mande, J. Phys. C: Solid State Phys. **17**, 955 (1984).

[68] J. L. Shay and J. H. Wernick, *Ternary Chalcopyrite Semiconductors: Growth, Electronic Properties, and Applications* (Pergamon Press, Oxford, 1975).

[69] J. E. Jaffe and A. Zunger, Phys. Rev. B **29**, 1882 (1984).

[70] S. N. Rashkeev and W. R. L. Lambrecht, Phys. Rev. B **63**, 165212 (2001).

[71] D. I. Bilc, *Electronic Structure and Thermoeletric Properties of Narrow Band Gap Chalcogenides* (PhD Thesis, Michigan State University, 2005).

[72] R. S. Kumar, A. L. Cornelius, E. Kim, Y. Shen, S. Yoneda, C. Chen, and M. F. Nicol, Phys. Rev. B **72**, 060101(R) (2005).

[73] L. G. Voinova, V. A. Bazakutsa, S. A. Dembovskii, L. G. Lisovskii, E. P. Sokol, and C. T. Kantser, Izv. Vys. Uchebn. Zav., Fizika **5**, 154 (1971) (in Russian).

[74] A. S. Tsytko, S. A. Dembovskii, I. I. Ezhik, and V. A. Bazakutsa, Izv. Vys. Uchebn. Zav., Fizika **12**, 154 (1969) (in Russian).

[75] R. A. Hein and E. M. Swiggard, Phys. Rev. Lett. **24**, 53 (1970).

[76] B. Wölfing, C. Kloc, J. Teubner, and E. Bucher, Phys. Rev. Lett. **86**, 4350 (2001).

[77] K. Kurosaki, A. Kosuga, and S. Yamanaka, J. Alloys Compounds **351**, 279 (2003).

[78] K. Kurosaki, H. Uneda, H. Muta, and S. Yamanaka, J. Alloys Compounds **376**, 43 (2004).

[79] S. M. Allen and J. W. Cahn, Acta Metall. **20**, 423 (1972).

[80] C. Wolverton and A. Zunger, Phys. Rev. B **57**, 2242 (1998); J. Electrochem. Soc. **145**, 2424 (1998).

[81] D. J. Singh, *Planewaves, Pseudopotentials, and the LAPW Method* (Kluwer Academic, Boston, 1994).

[82] P. Blaha *et al.*, *WIEN2k, An Augmented Plane Wave + Local Orbitals Program for Calculating Crystal Properties*, edited by Karlheinz Schwarz (Technische Universität Wien, Austria, 2001).

[83] M. Lax, *Symmetry Principles in Solid State and Molecular Physics* (Wiley, New York, 1974).

[84] W. A. Harrison, *Elementary Electronic Stucture* (World Scientific, Singapore, 2004).

[85] V. P. Zhuse, V. M. Sergeeva, and E. L. Shtrum, Sov. Phys. Tech. Phys. **3**, 1925 (1958).

[86] D. Bagayoko, L. Franklin, H. Jin, and G. L. Zhao, Phys. Rev. B **76**, 037101 (2007); and references therein.

[87] T. Tritt *et al.* (private communication).

[88] D. M. Bylander and L. Kleinman, Phys. Rev. B **41**, 7868 (1990).

[89] L. Ye, K. Hoang, A. Freeman, S. D. Mahanti, and M. G. Kanatzidis (to be submitted).

[90] J. Heremans *et al.* (private communication).

[91] J. X. Zheng, G. Ceder, T. Maxisch, W. K. Chim, and W. K. Choi, Phys. Rev. B **73**, 104101 (2006).

[92] X. Gao and M. Daw, APS March Meeting (March 5-9, 2007), Abstract No. D40.013.

[93] A. Zunger, S.-H. Wei, L. G. Ferreira, and J. E. Bernard , Phys. Rev. Lett. **65**, 353 (1989).

[94] A. van de Walle, M. Asta, and G. Ceder, *The Alloy Theoretic Automated Toolkit: A User Guide*, CALPHAD Journal **6**, 539 (2002).

[95] M. Kapon, G. M. Reisner, and R. E. Marsh, Acta Cryst. C**45**, 2029 (1989).

[96] L. D. Calvert, Acta Cryst. B **48**, 113 (1992).

[97] S. A. Semiletov and L. I. Man, Kristallografia **4**, 414 (1959).

[98] E. F. Hockings and J. G. White, Acta Cryst. **14**, 328 (1961).

[99] K. Chrissafis, E. S. Vinga, K. M. Paraskevopoulos, and E. K. Polychroniadis, phys. stat. sol. (a) **196**, 515 (2003).

[100] O. Madelung, *Semiconductors: Data Handbook*, 3rd ed. (Spinger, Berlin, 2004) and references therein.

[101] N. B. Brandt, D. V. Gitsu, N. S. Popovich, V. I. Sidorov, S. M. Chudinov, Sov. Phys. Semicond. **8**, 390 (1974).

[102] K. Wacker, M. Salk, G. Decker-Schultheiss, and E. Keller, Z. anorg. allg. Chem. **606**, 51 (1991).

[103] P. N. Rey, J. C. Jumas, J. Olivier-Fourcade, and E. Philippot, Acta Cryst. C **39**, 971 (1983).

[104] O. Valassiades, E. K. Polychroniadis, J. Stoemenos, and N. A. Economou, Phys. Stat. Sol. (a) **65**, 215 (1981).

[105] J. D. Jensen, J. R. Burke, D. W. Ernst, and R. S. Allgaier, Phys. Rev. B **6**, 319 (1972).

[106] G. P. Agrawal and N. K. Dutta, Semiconductor Lasers (van Nostrand Reinhold, New York, 1993), p. 547.

[107] S. Chatterjee and U. Pal, Opt. Eng. (Bellingham) **32**, 2923 (1993).

[108] T. K. Chaudhuri, Int. J. Energy Res. **16**, 481 (1992).

[109] J. H. Dughaish, Physica B **322**, 205 (2002).

[110] P. F. Poudeu, J. D'Angelo, H. Kong, A. Downey, J. L. Short, R. Pcionek, T. P. Hogan, C. Uher, and M. G. Kanatzidis, Am. Chem. Soc. **128**, 14347 (2006).

[111] J. R. Sootsman, R. J. Pcionek, H. Kong, C. Uher, and M. G. Kanatzidis, Chem. Mater. **18**, 4993 (2006).

[112] M.-K. Han, K. Hoang, H. Kong, R. Pcionek, C. Uher, K. M. Paraskevopoulos5, S. D. Mahanti, M. G. Kanatzidis (to be submitted to *Chemistry of Materials*).

[113] S. K. Plachkova and I. A. Avramova, phys. stat. sol. (a) **184**, 195 (2001).

[114] A. J. Mountvala and G. Abowitz, J. Am. Ceram. Soc. **48**, 651 (1965).

[115] E. I. Rogacheva, I. M. Krivulkin, O. N. Nashchekina, A. Yu. Sipatov, V. A. Volobuev, and M. S. Dresselhaus, Appl. Phys. Lett. **78**, 3238 (2001).

[116] H. S. Lee, B. Cheong, T. S. Lee, K. S. Lee, W. M. Kim, J. W. Lee, S. H. Cho, and J. Y. Huh, Appl. Phys. Lett. **85**, 2782 (2004).

[117] K. Kishimoto, M. Tsukamoto, and T. Koyanagi, J. Appl. Phys. **92**, 5331 (2002).

[118] E. I. Rogacheva, O. N. Nashchekina, S. N. Grigorov, M. A. Us, M. S. Dresselhaus, and S. B. Cronin, Nanotechnology **14**, 53 (2003).

[119] E. I. Rogacheva, O. N. Nashchekina, A. V. Meriuts, S. G. Lyubchenko, M. S. Dresselhaus, and G. Dresselhaus, Appl. Phys. Lett. **86**, 063103 (2005).

[120] E. I. Rogacheva, S. N. Grigorov, O. N. Nashchekina, T. V. Tavrina, S. G. Lyubchenko, A. Yu. Sipatov, V. V. Volobuev, A. G. Fedorov, and M. S. Dresselhaus, Thin Solid Films **493**, 41 (2005).

[121] X. Qiu, Y. Lou, A. C. S. Samia, A. Devadoss, J. D. Burgess, S. Dayal, and C. Burda, Angew. Chem. Intl. Ed. **44**, 5855 (2005).

[122] C. Wang, G. Zhang, S. Fan, and Y. Li, J. Phys. Chem. Solids **62**, 1957 (2001).

[123] B. Poudel, W. Z. Wang, D. Z. Wang, J. Y. Huang, and Z. F. Ren, J. Nanosci. Nanotech. **6**, 1050 (2006).

[124] B. Zhang, J. He, and T. M. Tritt, Appl. Phys. Lett. **88**, 043119 (2006).

[125] W. Heiss, H. Groiss, E. Kaufmann, G. Hesser, M. Böberl, G. Springholz, F. Schäffler, K. Koike, H. Harada, and M. Yano, Appl. Phys. Lett. **88**, 192109 (2006).

[126] B. A. Akimov, V. A. Bogoyavlenskiy, L. I. Ryabova, and V. N. Vasil'kov, Phys. Rev. B **61**, 16045 (2000).

[127] Ya. A. Ugai, A. M. Samoilov, M. K. Sharov, O. B. Yatsenko, and B. A. Akimov, Inorg. Mat. **38**, 12 (2002).

[128] Ya. A. Ugai, A. M. Samoilov, S. A. Buchnev, Yu. V. Synorov, and M. K. Sharov, Inorg. Mat. **38**, 450 (2002).

[129] A. M. Samoilov, S. A. Buchnev, Yu. V. Synorov, B. L. Agapov, and A. M. Khoviv, Inorg. Mat. **39**, 1132 (2003).

[130] A. M. Samoilov, S. A. Buchnev, E. A. Dolgopolova, Yu. V. Synorov, and A. M. Khoviv, Inorg. Mat. **40**, 349 (2004).

[131] H. Murakami, W. Hattori, and R. Aoki, Physica C **269**, 83 (1996).

[132] H. Murakami, W. Hattori, Y. Mizomata, and R. Aoki, Physica C **273**, 41 (1996).

[133] H. Murakami, R. Aoki, and K. Sakai, Thin Solid Films **343-344**, 27 (1999).

[134] B. A. Volkov, L. I. Ryabova, and D. R. Khokhlov, Phys.-Usp. **45**, 819 (2002), and references therein.

[135] C. S. Lent, M. A. Bowen, R. S. Allgaier, J. D. Dow, O. F. Sankey, and E. S. Ho, Solid State Commun. **61**, 83 (1987).

[136] N. J. Parada and G. W. Pratt, Phys. Rev. Lett. **22**, 180 (1969).

[137] N. J. Parada, Phys. Rev. B **3**, 2042 (1971).

[138] L. A. Hemstreet, Phys. Rev. B **12**, 1212 (1975).

[139] K. Weiser, Phys. Rev. B **23**, 2741 (1981).

[140] B. A. Volkov and O. A. Pankratov, Zh. Eksp. Teor. Fiz. **88**, 280 (1985) [Sov. Phys. JETP **61**, 164 (1985)].

[141] S. D. Mahanti and D. Bilc, J. Phys.: Condens. Matter. **16**, S5277 (2004).

[142] H. Hazama, U. Mizutani, and R. Asahi, Phys. Rev. B **73**, 115108 (2006)

[143] S. Ahmad, K. Hoang, and S. D. Mahanti, Phys. Rev. Lett. **96**, 056403 (2006).

[144] S. Ahmad, S. D. Mahanti, K. Hoang, and M. G. Kanatzidis, Phys. Rev. B **74**, 155205 (2006).

[145] I. Hase and T. Yanagisawa, Physica C **445-448**, 61 (2006).

[146] S. C. Erwin, L. Zu, M. I. Haftel, A. L. Efros, T. A. Kennedy, and D. J. Norris, Nature **436**, 91 (2005).

[147] G. M. Dalpian and J. R. Chelikowsky, Phys. Rev. Lett. **96**, 226802 (2006).

[148] K. Kishimoto and T. Koyanagi, J. Appl. Phys. **92**, 2544 (2002).

[149] A. Satta and S. de Gironcoli, Phys. Rev. B **63**, 033302 (2000).

[150] J. Ma, Y. Jia, Y. Song, E. Liang, L. Wu, F. Wang, X. Wang, and X. Hu, Surface Science **551**, 91 (2004).

[151] K. Hoang, S. D. Mahanti, and P. Jena, Phys. Rev. B **76**, 115432 (2007).

[152] S. D. Mahanti, K. Hoang, and S. Ahmad, Physica B **401-402**C, 291 (2007.

[153] F. Bechstedt, *Principles of Surface Physics* (Springer-Verlag, Berlin, 2003).

[154] J. Neugebauer and M. Scheffler, Phys. Rev. B **46**, 16067 (1992); M. Bockstedte, A. Kley, J. Neugebauer, and M. Scheffler, Comput. Phys. Commun. **107**, 187 (1997).

[155] W. H. Press, B. P. Flannery, S. A. Teukolsky, and W. T. Vetterling, *Numerical Recipes* (Cambridge University Press, New York, 1992).

[156] H. J. Monkhorst and J. D. Pack, Phys. Rev. B **13**, 5188 (1976).

[157] P. E. Blöchl, O. Jepsen, and O. K. Andersen, Phys. Rev. B **49**, 16223 (1994).

[158] R. M. Nieminen, in *Theory of Defects in Semiconductors*, edited by D. A. Drabold and S. Estreicher (Springer, Berlin, 2007).

[159] P. A. Schultz, Phys. Rev. Lett. **96**, 246401 (2006).

[160] A. A. Lazarides, C. B. Duke, A. Paton, and A. Kahn, J. Vac. Sci. Technol. A **13**, 1378 (1995).

[161] J. P. Perdew, J. A. Chevary, S. H. Vosko, K. A. Jackson, M. R. Pederson, D. J. Singh, and C. Fiolhais, Phys. Rev. B **46**, 6671 (1992).

[162] J. P. Perdew and A. Zunger, Phys. Rev. B **23**, 5048 (1981).

[163] For an extensive discussion of the structural and electronic properties of (bulk) lead chalgogenides from *ab initio* calculations using different methods, see, K. Hummer, A. Grüneis, and G. Kresse, Phys. Rev. B **75**, 195211 (2007) and references therein.

[164] M. Green, M. J. Lee, and R. E. Miles, Surface Science **12**, 403 (1968).

[165] For a comprehensive discussion of the DFT-related problems in defect calculations and possible improvements, see the book chapter by R. M. Nieminen (Ref. [158]).

[166] Khokhlov (Ed.), *Lead Chalcogenides: Physics and applications* (Taylor & Francis, New York, 2003).

[167] D. R. Khokhlov, Phys.-Usp. **49**, 955 (2006).

[168] Z. Dashevsky, S. Shusterman, M. P. Dariel, and I. Drabkin, J. Appl. Phys. **92**, 1425 (2002).

[169] H. P. Hjalmarson *et al.*, Phys. Rev. Lett. **44**, 810 (1980).

[170] D. M. Duffy, J. P. Hoare, and P. W. Tasker, J. Phys. C: Solid State Phys. **17**, L195 (1984).

[171] L. Esaki, P. J. Stiles, and L. L. Chang, Phys. Rev. Lett. **20**, 1108 (1968).

[172] T. V. Bocharova, A. N. Veis, Z. M. Dashevsky, V. A. Kotelnikov, and R. Yu. Krupitskaya, Sov. Phys. Semicond. **15**, 103 (1981).

[173] D. Bilc, S. D. Mahanti, and M. G. Kanatzidis, Phys. Rev. B **74**, 125202 (2006).

[174] S. Wu, H. Zeng, and Z. A. Schelly, Langmuir **21**, 686 (2005).

[175] W. Lu, P. Gao, W. B. Jian, Z. L. Wang, and J. Fang, J. Am. Chem. Soc. **126**, 14816 (2004).

[176] E. V. Shevchenko, D. V. Talapin, N. A. Kotov, S. O'Brien, and C. B. Murray, Nature **439**, 55 (2006).

[177] T. Mokari, M. Zhang, and P. Yang, J. Am. Chem. Soc. **129**, 9864 (2007).

[178] R. S. Kane, R. E. Cohen, and R. Silbey, J. Phys. Chem. **100**, 7928 (1996).

[179] H. Zeng, Z. A. Schelly, K. Ueno-Noto, and D. S. Marynick, J. Phys. Chem. A **109**, 1616 (2005).

[180] G. Allan and C. Delerue, Phys. Rev. B **70**, 245321 (2004).

[181] M. Shim, C. Wang, D. J. Norris, and P. Guyot-Sionnest, MRS Bull. **26**, 1005 (2001).

[182] R. O. Jones, B. W. Clare, and P. J. Jennings, Phys. Rev. B **64**, 125203 (2001).

[183] Z. Zhou, M. L. Steigerwald, R. A. Friesner, and L. Brus, Phys. Rev. B **71**, 245308 (2005).

[184] S. Ossicini, E. Degoli, F. Iori, E. Luppi, R. Magri, G. Cantele, F. Trani, and D. Ninno, Appl. Phys. Lett. **87**, 173120 (2005).

[185] G. Cantele, E. Degoli, E. Luppi, R. Magri, D. Ninno, G. Iadonisi, and S. Ossicini, Phys. Rev. B **72**, 113303 (2005).

[186] F. Iori, E. Degoli, R. Magri, I. Marri, G. Cantele, D. Ninno, F. Trani, O. Pulci, and S. Ossicini, Phys. Rev. B **76**, 085302 (2007).

[187] M. Lannoo, C. Delerue, G. Allan, Y.-M. Niquet, Phil. Trans. R. Soc. Lond. A **361**, 259 (2003).

[188] B. A. Cook, X. Wei, J. L. Harringa, and M. J. Kramer, J. Mater. Sci. **42**, 7643 (2007).

[189] J. J. Rehr and R. C. Albers, Rev. Mod. Phys. **72**, 621 (2000).

[190] H. Lin, E. S. Božin, S. J. L. Billinge, E. Quarez, and M. G. Kanatzidis, Phys. Rev. B **72**, 174113 (2005).

[191] T. J. Zhu, F. Fan, S. N. Zhang, and X. B. Zhao, J. Phys. D: Appl. Phys. **40**, 3537 (2007).

[192] L. Esaki and P. J. Stilles, Phys. Rev. Lett. **16**, 1108 (1966).

[193] Y. W. Tung and M. L. Cohen, Phys. Rev. Lett. **180**, 823 (1969).

[194] H. M. Polatoglou, Physica Scripta **39**, 251 (1989).

[195] A. H. Edwards, A. C. Pineda, P. A. Schultz, M. G. Martin, A. P. Thompson, and H. P. Hjalmarson, J. Phys.: Condens. Matter **17**, L329 (2005).

[196] See, e.g., D. W. Brenner, *Computer Modeling of Nanostructred Materials*, in *Nanostructured Materials: Processing, Properties and Applications*, edited by C. C. Koch (William Andrew Inc., 2006).

[197] J. J. de Pablo and W. A. Curtin (Eds.), *Multiscale Modeling in Advanced Materials Research*, MRS Bull. **32** (November 2007).